Predictability of Medicanes in the ECMWF ensemble forecast system

Zur Erlangung des akademischen Grades eines
DOKTORS DER NATURWISSENSCHAFTEN
von der KIT-Fakultät für Physik des
Karlsruher Instituts für Technologie (KIT)

genehmigte

DISSERTATION

von

M.Sc. Enrico Di Muzio
aus Guardiagrele, Italien

Tag der mündlichen Prüfung:	5. Juli 2019
Referent:	Prof. Dr. Peter Knippertz
Korreferent:	Prof. Dr. Andreas H. Fink
Außerhäusiger Referent:	Dr. Michael Riemer

Abstract

Medicanes (short for *Medi*terranean hurri*canes*) are small but intense tropical-like cyclones that occasionally strike the Mediterranean region, constituting a major threat due to strong winds, abundant precipitation and flooding. These cyclones are preceded by multiple meteorological phenomena at various spatial and temporal scales, from planetary-scale Rossby waves breaking over western Europe to a synoptic-scale upper-level trough intruding the Mediterranean region and developing into a cut-off. These precursor structures help destabilize the atmosphere and promote cyclogenesis and deep convection, which in turn enables the development of a warm core during the mature stage of these cyclones. Medicanes typically exhibit several tropical-like traits, such as nearly perfect axial symmetry, spiralling clouds and a clear-sky region in the vicinity of their center resembling the eye of a hurricane. These storms occur infrequently and often in regions with scarce observations, and their development is influenced by the interplay of numerous processes ranging from the planetary to the convective scale. For this reason, predicting Medicanes is a challenge for operational weather forecasts.

The overarching goal of this thesis is to assess the predictability of Medicanes through the evaluation of European Centre for Medium-Range Weather Forecasts (ECMWF) operational ensemble forecasts. For this purpose, a systematic investigation of seven recent (2011–2017) Medicanes and a 2016 tropical-like storm which occurred over the Bay of Biscay is carried out by using an object-based approach, whereby both the cyclone and antecedent large-scale precursors are treated as objects and characterized via suitable parameters. This approach helps simplify the analysis and meaningfully condense vast amounts of data, extracting the most relevant quantities.

The eight cases and the corresponding antecedent large-scale processes are first characterized using ECMWF observational analysis data. A large case-to-case variability is found, although all events exhibit a common development pathway, with a Rossby wave packet forming far upstream over the Atlantic Ocean, travelling eastward and

breaking over western Europe few days prior to cyclone formation; the Rossby wave packet is associated with an upper-level trough penetrating into the Mediterranean region and often, but not always, developing into a cut-off. The eight cases also exhibit common features, such as an upper-level warm core and a strong symmetrization and contraction of the cyclone during its early stage. Medicanes are found to fit the tropical transition paradigm, whereby a midlatitude baroclinic cyclone transforms into a largely barotropic (sub)tropical cyclone.

ECMWF ensemble forecasts are found to successfully reproduce the eight cases, with no systematic errors, although predictability and forecast consistency strongly depend on the case. For some events, short-term forecasts exhibit a high probability of extreme winds and wind gusts occurring, though not all Medicanes are predicted to be as extreme. The occurrence of the cyclone is generally well forecast, with higher probability than 50% at 7 days lead time. Cyclone position uncertainty also evolves remarkably steadily with lead time. Conversely, the largest uncertainty is seen for upper-level thermal wind, representing the cyclone's warm or cold core. This indicates that the development of an upper-level warm core is one of the least predictable aspects of Medicane forecasts, with a forecast horizon of only 1–3 days. The presence of forecast jumps found in most cases for cyclone occurrence and structure confirm previous findings of a high sensitivity of Medicane forecasts to the initial conditions and hints at the existence of predictability barriers.

A Rossby wave packet breaking over western Europe is observed for all cases and found to be predictable up to 10 days prior to cyclone formation. Interestingly, ensemble forecasts do not indicate a significant linkage between the occurrence and features of the cyclone and those of the Rossby wave packet, with the exception of weak hints that a cyclone is less likely to develop if Rossby wave breaking fails to occur. These findings suggest that the primary role of planetary-scale processes is to bring about a large-scale environment that is later conducive for cyclogenesis and air-sea instability.

On the other hand, the presence and intensity of the upper-level cut-off trough are found to be instrumental in determining cyclone occurrence, while their linkage to cyclone thermal structure is highly variable. A stronger trough and/or a better vertical alignment with the surface cyclone is associated with a higher cyclone occurrence probability and a deeper warm core in most cases. Nevertheless, warm core magnitude is negatively linked with trough depth for two events, suggesting that the influence of

large-scale upper-level dynamics strongly depends on the case and works in synergy with small-scale factors, consistently with previous findings.

Preface

The PhD candidate confirms that the research presented in this thesis contains significant scientific contributions by himself. This thesis reuses material from the following publication (Di Muzio et al. 2019):

Di Muzio, E., Riemer, M., Fink, A. H. and Maier-Gerber, M., 2019: Assessing the predictability of Medicanes in ECMWF ensemble forecasts using an object-based approach. *Q. J. R. Meteorol. Soc.*, **145(720)**, 1202–1217. DOI:10.1002/qj.3489

Chapters 1, 2, 4, 5, 6 and 7 reuse material from Di Muzio et al. (2019). The research leading to these results has been accomplished within project C “Multi-scale Dynamics and Predictability of Atlantic Subtropical Cyclones and Medicanes” of the Transregional Collaborative Research Center SFB / TRR 165 “Waves to Weather” funded by the German Science Foundation (DFG). The research proposal of this project was written by Andreas H. Fink and Michael Riemer. The analysis in Di Muzio et al. (2019) was solely carried out by the candidate, who also wrote the text with advice from Michael Riemer, Andreas H. Fink and Michael Maier-Gerber and comments from all co-authors during the manuscript preparation.

The candidate confirms that appropriate credit has been given within the thesis where reference has been made to the work of others. This copy has been supplied on the understanding that this is copyright material and that no quotation from the thesis may be published without proper acknowledgment.

Contents

Chapter 1

Introduction

The Mediterranean region has long been known as a hotspot for cyclogenesis (Peterssen 1956; Ulbrich et al. 2009; Neu et al. 2013) also due to its geography (Buzzi and Tibaldi 1978). The most intense Mediterranean cyclones can cause high-impact weather such as torrential rainfall, windstorms, landslides and floods (Jansá et al. 2000; De Zolt et al. 2006; Nissen et al. 2010; Lionello et al. 2012; Pfahl and Wernli 2012). A fraction of these cyclones display some similarity to tropical cyclones, both in their appearance in satellite images and in their kinematic and thermal structure, and are consequently known as Mediterranean tropical-like cyclones or *Medicanes* (portmanteau word from *Medi*terranean hurri*canes*). Medicanes have been documented since the beginning of the satellite era (Ernst and Matson 1983; Mayengon 1984; Rasmussen and Zick 1987) and constitute a major threat in the Mediterranean region. These storms are usually shorter-lived than North Atlantic hurricanes but may exhibit several tropical-like traits in the mature phase of their life cycle, such as high axial symmetry, a warm core, a strong tendency to weaken after making landfall and a cloud-free, weak-wind region at their centre resembling the eye of a hurricane (Emanuel 2005; Cavicchia et al. 2014a).

Medicanes are distinguished among Mediterranean cyclones by the complex pathway leading to their formation and maintenance. While a large fraction of hurricanes develop in regions of near-zero baroclinicity and draw their energy from the warm tropical ocean, Medicanes arise from pressure lows that are born under moderate to strong baroclinicity (Cavicchia et al. 2014a; Mazza et al. 2017). The interaction between the warm sea and cold air associated with a deep upper-level trough provides the necessary thermodynamic disequilibrium for these storms to develop a warm core (Emanuel 2005; Cavicchia et al. 2014a) undergoing a process known as tropical transition (Davis and Bosart 2003, 2004). It can thus be stated that Medicanes are the result of a synergy

between synoptic-scale processes, which provide the necessary environment for their development, and mesoscale processes such as deep convection and latent heat fluxes from the sea, which are crucial for their maintenance (Homar et al. 2003; Emanuel 2005; Tous et al. 2013). For this reason and because of their small size (Miglietta et al. 2013; Picornell et al. 2014) and low frequency (Cavicchia et al. 2014a), these storms can be considered extreme events and are therefore found at the end of the spectrum of Mediterranean cyclones. Due to the complex Mediterranean orography and the fact that observations are sparse over the sea, Medicanes remain elusive and thus pose a considerable challenge for numerical weather forecasts.

Research efforts so far focused chiefly on modeling aspects (Homar et al. 2003; Fita et al. 2007; Moscatello et al. 2008a; Davolio et al. 2009; Miglietta et al. 2011; Chaboureau et al. 2012a; Miglietta et al. 2013; Cioni et al. 2016; Mazza et al. 2017; Pytharoulis et al. 2017; Cioni et al. 2018) and, to a lesser extent, observational aspects (Pytharoulis et al. 2000; Reale and Atlas 2001; Moscatello et al. 2008b; Chaboureau et al. 2012b; Miglietta et al. 2013). Deterministic simulations with high-resolution, convection-permitting models (Fita et al. 2007; Davolio et al. 2009; Cioni et al. 2016; Mazza et al. 2017; Pytharoulis et al. 2017; Cioni et al. 2018) have been deemed to best reproduce small-scale processes playing a crucial role in the maintenance of Medicanes during their tropical-like phase. On the other hand, few studies analyzed Medicanes using ensemble forecasts (Cavicchia and von Storch 2012; Chaboureau et al. 2012a; Pantillon et al. 2013; Mazza et al. 2017), of which only Pantillon et al. (2013) used operational forecasts. While Chaboureau et al. (2012b) and Pantillon et al. (2013) examined the predictability of a single case, no study has so far attempted at systematically investigating the predictability of multiple cases.

This gap is bridged in the present thesis, in which European Centre for Medium-Range Weather Forecasts (ECMWF) operational ensemble forecasts are used to analyze the predictability of eight recent (2011-2017) tropical-like cyclones: seven Medicanes and the first case ever documented in the Bay of Biscay. The scope of this work is threefold. The eight events are first characterized using ECMWF operational analysis data, describing their commonalities as well as their variability. Focus then shifts to ensemble forecasts, assessing whether and how long in advance they can adequately reproduce the eight cyclones, investigating forecast uncertainty and variability and analyzing the evolution of cyclone predictability with lead time. Finally, the fundamental large-scale factors influencing the formation of Medicanes are examined, assessing

their predictability and their impact on cyclone predictability as well as identifying different pathways of Medicane development.

In this thesis, ensemble forecasts are evaluated against operational analysis data using an object-based approach. Object-based methods gained popularity in recent decades for the verification of precipitation forecasts (Ebert and McBride 2000; Wernli et al. 2008) and have since been applied to the analysis of other atmospheric features, such as the jet stream (Limbach et al. 2012) and Rossby waves (Glatt and Wirth 2014). Here, each cyclone is treated as an object and the storm's predictability is evaluated using suitable parameters that describe cyclone intensity, position and structure and comparing the analysis object's parameter values with the forecast object's ones. The benefits of using an object-based approach will be discussed in further detail in Chapters 2 and 4, together with a suite of methods including a dynamic time warping method (Berndt and Clifford 1994), which is used to better match cyclones in forecasts with the one in the analysis, a Rossby wave packet identification method (Wolf and Wirth 2015, 2017), and a Rossby wave breaking identification method based on the one developed by Rivière (2009).

The thesis is structured as follows. In Chapter 2, the state of the art in predictability, ensemble forecasting, tropical transition and Medicanes is discussed. The objectives of the thesis are provided in Chapter 3. In Chapter 4, a brief overview of the data and methods used is given. Chapter 5 contains a detailed characterization of the eight cases, with a description of their large-scale environment, their features as well as their commonalities and variability. Ensemble forecasts are discussed in detail in Chapter 6: specifically, findings on the overall predictability of the eight cases are presented in Section 6.1, while the large-scale dynamical processes influencing their predictability are discussed in detail in Section 6.2. Finally, results are summarized and contextualized, and an outlook is discussed in Chapter 7.

Chapter 2

State of the art

This chapter will provide an overview of the state of the art in predictability, ensemble forecasting, object-based methods, tropical transition and Medicanes.

2.1 Predictability

Numerical weather prediction has made giant steps since its inception in the 1950s (Lynch 2008). Weather forecasts have tremendously improved over the past decades and trends are still positive (Figure 2.1; after Figure 1 of Bauer et al. 2015). Nevertheless, forecasts are still far from perfect, due to insufficient observations, model deficiencies as well as the intrinsic complexity of the atmospheric system.

The atmosphere is a nonlinear dynamic system which shows chaotic behavior (Palmer 2000), being highly sensitive to initial conditions. This is often expressed with the well-known *butterfly effect* metaphor, which states that a butterfly flapping its wings in Brazil can (theoretically) influence the occurrence of a tornado in Texas. The metaphor signifies the strong influence of the initial state of the atmosphere on its time evolution: tiny variations of the former can result in large differences in the latter. As observations can never represent the true state of the atmosphere, forecasts will never have 100% accurate initial conditions. Even small errors will tend to grow with simulation time until the forecast has no longer any skill. A simple paradigm for the evolution of small errors was proposed by Lorenz (1982) for a perfect model – in this case the only source of error is the initial condition error – as follows:

$$\frac{d\varepsilon}{dt} = a\varepsilon(1-\varepsilon) \tag{2.1}$$

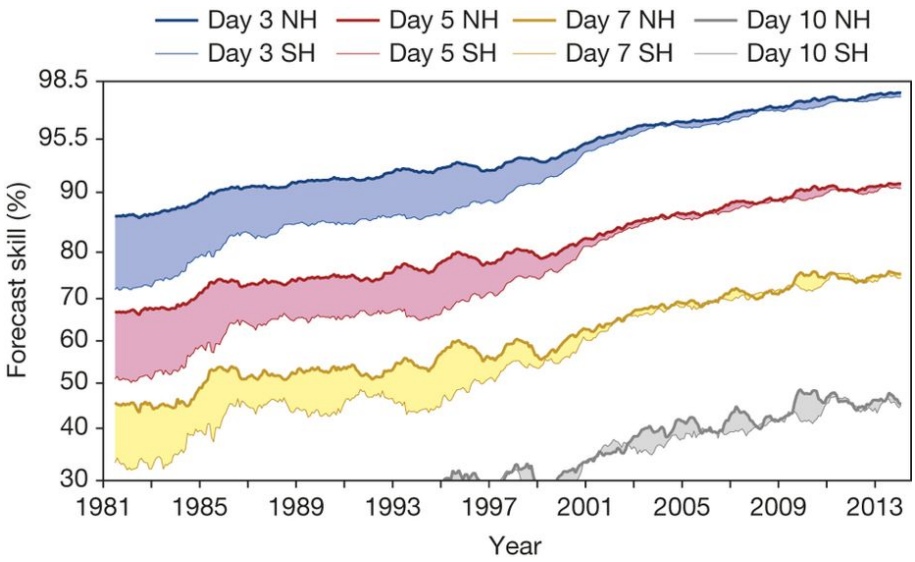

Figure 2.1: *A measure of forecast skill at three-, five-, seven- and ten-day ranges, computed over the extra-tropical northern and southern hemispheres. Forecast skill is the correlation between the forecasts and the verifying analysis of the height of the 500-hPa level, expressed as the anomaly with respect to the climatological height. Values greater than 60% indicate useful forecasts, while those greater than 80% represent a high degree of accuracy. The convergence of the curves for Northern Hemisphere and Southern Hemisphere after 1999 indicates the breakthrough in exploiting satellite data through the use of variational data. Figure and caption reprinted by permission from Springer Nature: Nature,* The quiet revolution of numerical weather prediction*, Bauer P, Thorpe A. and Brunet G., Copyright 2015.*

where ε is the average root mean square error of the forecast, scaled so that $\varepsilon \to 1$ at long forecast times, and a is the growth rate. The solution of the logistic equation (2.1) is

$$\varepsilon(t) = \frac{\varepsilon_0 e^{at}}{1 + \varepsilon_0(e^{at} - 1)} \tag{2.2}$$

where ε_0 is the initial error. Small errors grow exponentially with a growth rate a until they reach finite amplitude, then growth slows down; saturation is reached at $\varepsilon \to 1$. The upscale error growth implies that even if the initial conditions were nearly perfect, very small errors would still grow up to larger scales (Lorenz 1969b; Palmer 2000), eventually causing forecast quality to deteriorate (Kalnay 2003).

In addition to initial condition errors, further error sources arise from model deficiencies, including numerical approximation, imprecise boundary conditions and parameterizations of unresolved processes such as cloud processes, radiative transfer and convection (Warner 2010). Errors can also be categorized into systematic and stochastic errors (Hamill et al. 2000): while the former are reproducible if the model is run several times over nearly identical cases, the latter cannot be reproduced. Errors

in the initial conditions fall into the second category, although they are partly caused by model deficiencies (Leutbecher and Palmer 2008), such that improving the model potentially reduces both systematic and stochastic errors.

As a consequence of the above-discussed errors and the complexity of the atmospheric system, weather phenomena have a limited predictability, which is most generally defined as "the extent to which future states of a system may be predicted based on knowledge of current and past states of the system" (Glossary of the American Meteorological Society[1]). Atmospheric predictability has been investigated from a variety of viewpoints, from dynamical systems theory (Bohr et al. 2005) to numerical weather prediction (Simmons and Hollingsworth 2002) to information theory (DelSole 2004).

A fundamental distinction is to be drawn between intrinsic and practical predictability (Lorenz 1996; Melhauser and Zhang 2012). Intrinsic predictability is the ability to predict in the idealized case of using a near-perfect model with practically error-free initial and boundary conditions. Lorenz (1963a,b) first postulated that the atmosphere has, as an unstable system, a finite limit of intrinsic predictability, as opposed to stable systems, which are infinitely predictable. The existence of such inherent limits, caused by the chaotic nature of the atmosphere (Lorenz 1969a), has been confirmed by subsequent studies (Zhang et al. 2007; Rotunno and Snyder 2008; Sun and Zhang 2016). In particular, Zhang et al. (2007) observe the strong role of moist convection in enhancing upscale error growth to the point that forecast error becomes less sensitive to small initial errors, while Palmer et al. (2014) highlight the existence of an "absolute, finite-time predictability barrier" in the atmosphere, which breaks the dependence of certain multiscale systems on the initial conditions at sufficiently large forecast lead times: these authors name such phenomenon "real butterfly effect" and remark on the flow-dependent nature of predictability, with a large variability in the sensitivity of large-scale forecasts to small-scale initial errors. Lorenz (1963a) first estimated the intrinsic predictability limit to be around two weeks, although it can be much lower depending on the situation and the upscale error growth rate, as shown for winter cyclones (e.g. Zhang et al. 2007; Sun and Zhang 2016) and tropical cyclones (Zhang and Sippel 2009; Tao and Zhang 2015).

Practical predictability, also referred to as prediction (or forecast) skill, comes into play when using an imperfect model with error-prone initial and boundary conditions (Lorenz 1982, 1996), as is usually the case. The limit of practical predictability can

[1] http://glossary.ametsoc.org/wiki/Predictability

be generally pushed farther away and closer to the one of intrinsic predictability by improving the accuracy of initial conditions and the quality of models (Zhang et al. 2007; Ying and Zhang 2017). Zhang et al. (2019) estimate this limit to be around 10 days for midlatitude weather, although in some cases forecast skill horizons are now exceeding two weeks (Buizza and Leutbecher 2015) thanks to considerable advances in numerical weather prediction as well as the shift to a probabilistic approach (see Section 2.2: Ensemble forecasting).

As a matter of fact, predictability depends on the variable (e.g. geopotential height is typically more predictable than precipitation), the model (higher resolution generally implies higher predictability) and the spatial and temporal scales at which a phenomenon occurs (Hamill et al. 2000; Selz 2019). As errors grow faster at the sub- and near-grid scale than at the synoptic scale (Lorenz 1969b; Murphy 1988; Leutbecher and Palmer 2008), the latter is generally more predictable (Zhang et al. 2019). Phenomena occurring at long time scales, like the El Niño—Southern Oscillation, can be successfully predicted a year in advance (Kalnay 2003). The atmospheric flow itself can play a significant role through its intrinsic stability or lack thereof, as first pointed out by Lorenz (1965): consequently, atmospheric predictability is highly variable (Palmer et al. 2014), with some periods being much more (or less) predictable than average (Kalnay 2003) and the related weather forecasts being markedly more (or less) skillful than usual (Lillo and Parsons 2017).

The degree of predictability depends on the extent to which the prior (i.e. climatological) and posterior (i.e. forecast) distributions differ: an event is said to be unpredictable if the two distributions are identical (DelSole 2004; Warner 2010). The approach to weather forecasting has changed tremendously in the last few decades, with the availability of ever increasing computational resources and the seminal shift from deterministic forecasts to probabilistic ensemble forecasts (Lynch 2008; Buizza and Leutbecher 2015), which allow a more precise estimation of the posterior distribution and therefore a more rigorous assessment of predictability. In the next section, ensemble forecasting will be introduced and described in its salient features.

2.2 Ensemble forecasting

After Lorenz (1963a,b, 1965) hypothesized on the atmosphere's finite limit of predictability and demonstrated its dependence on the evolution of the flow itself, it was clear that numerical weather prediction should somehow account for the high

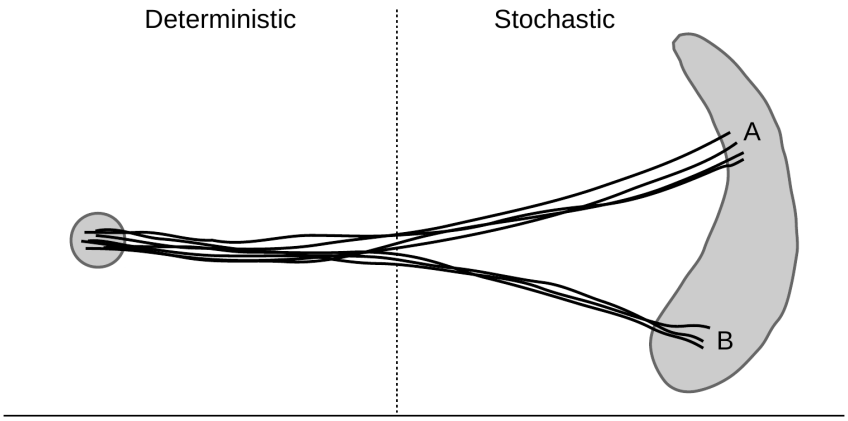

Figure 2.2: *Schematic of ensemble prediction. The circle on the left-hand side denotes the uncertainty of the initial conditions, each line corresponds to a forecast trajectory and the shape on the right-hand size represents the range of possible future states. The dashed line in the middle separates approximately the deterministic and stochastic regimes. The forecasts can be clustered into subsets A and B. Figure and caption were adapted from Figure 6.4.1 of* Atmospheric Modeling, Data Assimilation and Predictability*, Eugenia Kalnay, Copyright Eugenia Kalnay 2003; reproduced with permission of Cambridge University Press through PLSclear.*

sensitivity of the evolution of the atmosphere (Kalnay 2003). Lorenz (1965) himself investigated the behavior of a set ("ensemble") of "perturbed forecasts", i.e. forecasts that were initialized with slightly different initial conditions. While ensemble forecasting techniques have since undergone considerable development and are now used operationally by most major weather services, their underlying principles have not changed.

The fundamental idea of ensemble prediction is that by producing not just one, but multiple forecasts, each initialized with slightly perturbed initial conditions with respect to the control forecast, we take into account the uncertainty in our knowledge of the initial state of the atmosphere and therefore have insight into the full range of its possible future states, as shown schematically in Figure 2.2. Each individual forecast is considered equally probable and a distinction can be drawn between the deterministic regime, in which forecasts are close to each other and errors grow linearly, from the stochastic regime, in which error growth is nonlinear and forecasts may diverge sharply. The transition time between these regimes can be anywhere between a few hours and a few days, depending on the phenomenon predicted and its spatial scale: for large-scale phenomena it is around 2-3 days, while for mesoscale ones, such as storms and fronts, it is generally much shorter (Kalnay 2003). Highly nonlinear parameters such as precipitation diverge faster, and therefore have a shorter transition time, than more linear ones such as 500 hPa geopotential height.

Ensemble forecasting serves multiple purposes. Most prominently, it constitutes an effective means of tackling the issue of both initial condition errors and model errors: instead of aiming exclusively at reducing these errors as much as possible, their presence is capitalized on to explore forecast variability and estimate the probability distribution – the probability density function (PDF) – of possible future states of the atmosphere. Ensemble forecasting provides therefore a quantitative basis for probabilistic prediction, by which the probability of future events is determined: in the example in Figure 2.2, the probability of the future state being represented by cluster A (B) is 4/7 (3/7). Another essential goal of ensemble prediction is to improve forecast skill by ensemble averaging. The ensemble average indeed tends to retain only forecast components that are homogeneous (i.e. nearly identical) among the ensemble members, while filtering out the uncertain ones (Kalnay 2003). Consequently, the ensemble average tends to be closer to the truth than the control forecast (Toth and Kalnay 1997; Grimit and Mass 2002). However, this is only valid in the forecast's nonlinear, stochastic regime; during the regime of (nearly) linear error growth, the initial perturbations grow at a similar rate and essentially cancel each other out, such that the ensemble average is essentially equal to the control forecast. Ensemble averaging can also be a double-edged sword, as it may filter out significant features that are associated with low-probability, possibly extreme events.

Ensemble prediction is also advantageous when an indication of forecast reliability is needed. If the ensemble members are quite different from each other, it is certain that a fraction of them are wrong. If members are in good agreement, the forecast is likely (though not always) accurate. In some cases, forecast errors are dominated by systematic errors such as model deficiencies and most if not all members are far from the true evolution of the atmosphere. In such cases, schematized on the right-hand side of Figure 2.3, the ensemble forecast cannot be relied on, but it is still useful in diagnosing the error source, that is in recognizing that forecast errors are most likely due to systematic errors rather than to the growth of initial errors.

Ensemble prediction is computationally and financially costly. To keep costs at a minimum, ensemble forecasts are usually run at a lower resolution than deterministic forecasts: for instance, ECMWF currently (as of spring 2019[2]) runs the former (which are analyzed in this thesis) with an 0.2° (about 18 km) horizontal grid spacing and

[2]All characteristics of the ECMWF models are illustrated here: https://www.ecmwf.int/en/forecasts/documentation-and-support/evolution-ifs/cycles/summary-cycle-45r1

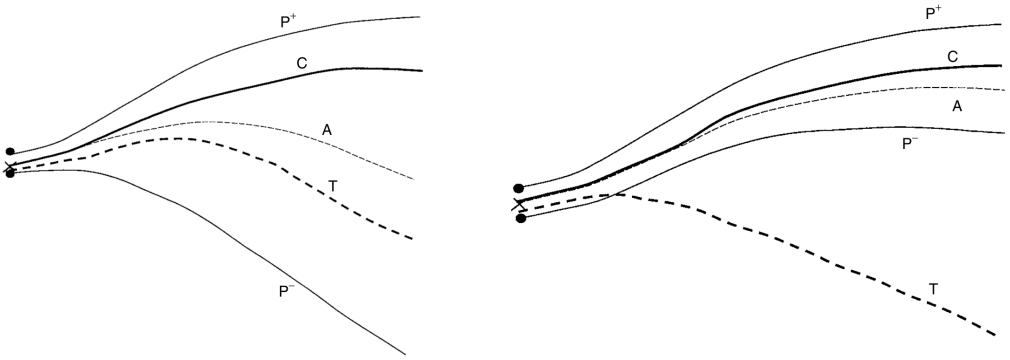

Figure 2.3: *Schematic of the components of a typical ensemble: the control forecast (C), starting from the analysis (denoted by a cross), which is the best estimate of the true initial state of the atmosphere; two perturbed ensemble forecasts (members P^+ and P^-) with initial perturbations respectively added and subtracted from the control forecast; the ensemble average (A); and the "true" evolution of the atmosphere (T).* (Left) *This is a "good" ensemble forecast, since T appears as a plausible member.* (Right) *This is a "bad" ensemble forecast, in which forecast errors are dominated by systematic errors. Figure and caption were adapted from Figure 6.5.1 of* Atmospheric Modeling, Data Assimilation and Predictability*, Eugenia Kalnay, Copyright Eugenia Kalnay 2003; reproduced with permission of Cambridge University Press through PLSclear.*

the latter with an 0.1° (about 9 km) grid spacing[3]. Weather agencies are also constantly faced with the critical choice of an optimal ensemble size and the consequent unavoidable compromise between having many members and/or a high resolution, which ensures a more precise estimation of the PDF of future atmospheric states and more reliable forecasts of extreme events (Palmer 2000; Buizza and Hollingsworth 2002; Palmer 2002; Lalaurette 2003; Buizza 2008), and sustaining high computational and financial costs.

Ensemble prediction techniques differ from one another chiefly in the way the perturbed initial conditions are produced. A key distinction can be drawn between techniques having random perturbations, which are denoted as Monte Carlo forecasting (Kalnay 2003), and those having perturbations that depend on the dynamics of the atmospheric flow at the moment of initialization. Two notable examples belonging to the latter category are the *breeding* technique (Toth and Kalnay 1993, 1997; Kalnay 2003), which is used by the National Centers for Environmental Prediction (NCEP) in the USA, and the *singular vectors* technique (Buizza and Palmer 1995; Palmer et al. 1998; Diaconescu and Laprise 2012), which is used at various weather agencies such as the ECMWF, the Japan Meteorological Agency, Météo-France and Bureau of Meteorology (BoM) in Australia.

[3]Even so, hundreds of terabytes' worth of data are generated daily: https://www.ecmwf.int/en/about/media-centre/key-facts-and-figures

The breeding technique is based on a random perturbation which is added to the initial conditions in the first place; the model is then integrated both from the control and the perturbed initial conditions; the control forecast is then subtracted from the perturbed forecast at fixed time intervals and the difference is scaled down to the same amplitude of the initial perturbation; the difference is finally used as new perturbation. Breeding thus uses perturbations that start out random, but slowly (over the course of a few days) "learn" the underlying flow dynamics, acquiring a faster growth rate than purely random perturbations and therefore being more suitable than those for ensemble prediction (Kalnay 2003).

The singular vector technique (first introduced by Lorenz (1965)) is based on determining the fastest-growing perturbations from a time-evolving basic state which is generated by the model itself: these perturbations, referred to as singular vectors, are orthogonal and, according to linear theory, exhibit the maximum growth over a finite time interval with respect to a specific metric (Diaconescu and Laprise 2012). The singular vector technique is effective in finding the most unstable perturbations along the directions of initial uncertainty that are associated with the largest forecast uncertainty (Leutbecher and Palmer 2008), thereby allowing an optimal estimation of the probability distribution of future atmospheric states.

For the sake of completeness, it is worth mentioning further ensemble prediction techniques that are not based on perturbing the initial conditions. Multi-model ensemble forecasting is widely used in climate science and consists of combining multiple deterministic forecasts from different models (Warner 2010): it has been used, for instance, by the Intergovernmental Panel for Climate Change for its reports on climate change (Pachauri et al. 2014). A model can also be integrated multiple times with either varying or fixed but stochastically perturbed parameterization schemes, to account for uncertainty in the representation of physical processes: as Berner et al. (2017) point out, this is a promising approach for both weather and climate ensemble prediction. Lastly, Ensemble Data Assimilation (EDA) uses measurement data in combination with an ensemble of short-range forecasts as a starting point to determine the state of the atmosphere. EDA has established at both the ECMWF (Buizza et al. 2008) and the NCEP (Whitaker et al. 2008) as a valid alternative to four-dimensional variational data assimilation (e.g. Rabier et al. 2000) for operational data assimilation systems.

Interpretation of ensemble forecasts is not straightforward. Since their output at each forecast time consists of a set of values, one for each member, their complexity is undoubtedly higher than that of deterministic forecasts, which conversely output

a single value per forecast time. The simplest properties used to evaluate ensemble forecasts are generally the two lowest-order moments of the forecast distribution, i.e. the ensemble mean and standard deviation, which is usually referred to as *spread*. A good ensemble forecast should have a sufficiently large spread to capture the true state of the atmosphere (which, in other words, should appear as one of the ensemble members), while reflecting the predictability of the specific situation: in principle, a small ensemble spread should be associated with high predictability and vice versa (Kalnay 2003). However, ensemble forecasts are often uncalibrated and underdispersive, which means that the true state lies outside the ensemble distribution as a consequence of forecast bias and dispersion errors (Gneiting et al. 2005), as already shown schematically on the right-hand side of Figure 2.3. Consequently, some form of calibration, also known as statistical postprocessing, is necessary (Gneiting and Raftery 2005; Gneiting and Katzfuss 2014) as well as beneficial (Warner 2010; Hopson 2014) in most cases.

Ensemble spread is generally positively correlated with ensemble error and negatively correlated with skill[4]. While it is reasonable to expect that large spread be associated with large error (or low skill) and vice versa, or at least that the probability of large errors be higher in cases of large spread (Buizza 1997; Grimit and Mass 2007), a high correlation between spread and error is not a necessary condition for ensemble forecasts (Whitaker and Loughe 1998). In fact, the spread-error distribution is not straightforward to determine quantitatively (Van Schaeybroeck and Vannitsem 2016), since it exhibits an increasing scatter at larger spread, depends from case to case and is significantly influenced by the spread's temporal variability (Grimit and Mass 2007). Even in the absence of a precise spread-skill relationship, however, the possibility of quantitatively estimating forecast uncertainty through ensemble forecasts makes them preferable to deterministic forecasts, especially in concert with statistical postprocessing (Hopson 2014).

Ensemble prediction has been shown to be a valuable approach to study and even improve atmospheric predictability (Palmer 2000, 2002; Palmer and Räisänen 2002; Buizza 2008) for multiple reasons. First, ensemble averaging shows a clearly higher skill compared with deterministic forecasts (Murphy 1988). Second, ensemble forecasts effectively provide an estimate of future uncertainty (Zhu 2005). Third, as predictability is highly variable in space, time and from a parameter to another,

[4]Numerous studies have examined the relationship between ensemble spread and either ensemble error or skill. While various definitions of both have been used from case to case, error is most simply defined as the deviation of the control forecast from the truth.

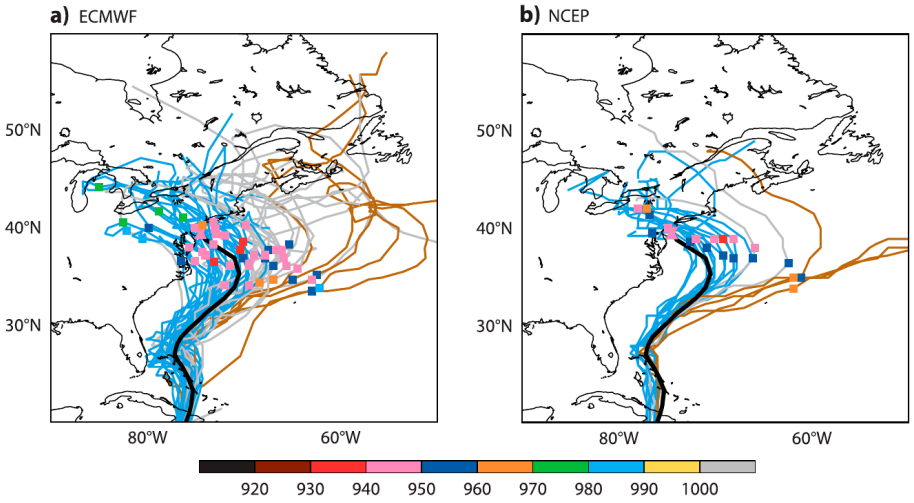

Figure 2.4: *ECMWF* (a) *and NCEP* (b) *ensemble forecasts initialized at 1200 UTC on October 24. The position at 0000 UTC on October 30 is indicated with a square, whose color represents the depth of the cyclone. Tracks are categorized according to their distance at landfall time from the observed landfall position: "hit" (blue tracks), "eastward" (brown) and "others" (gray). The NHC analysis track is shown in black and the observed landfall position is a pink hourglass symbol. Figure and caption were adapted from Magnusson et al. (2014). Reproduced with permission. © American Meteorological Society.*

ensemble prediction is advantageous to investigate this variability (Kalnay 2003). Fourth, ensemble forecasting can help extend the limits of predictability, as well as identify possible predictability barriers (Palmer et al. 2014). Furthermore, ensemble prediction has been shown to be a valuable tool to forecast extreme weather events several days in advance (Palmer 2000; Buizza and Hollingsworth 2002; Palmer 2002; Lalaurette 2003; Buizza 2008; Pantillon et al. 2013; Magnusson et al. 2015).

In particular, ensemble forecasts have shown high predictive skills for tropical cyclones (Yamaguchi and Majumdar 2010; Hamill et al. 2011) and have been widely used to analyze them (e.g. Torn and Cook 2013; Rios-Berrios et al. 2016) as well as investigate their predictability (Munsell et al. 2013; Zhang and Tao 2013; Magnusson et al. 2014; Pantillon et al. 2016; González-Alemán et al. 2018; an example of such application is given in Figure 2.4, where ensemble forecast uncertainty is shown for hurricane Sandy's landfall position). A few studies successfully used ensemble forecasts to examine Medicane predictability (Chaboureau et al. 2012b; Pantillon et al. 2013): specifically, Pantillon et al. (2013) found that ECMWF operational ensemble forecasts were able to more consistently capture early signals of the 2006 Medicane occurrence with respect to ECMWF deterministic forecasts.

A further benefit of using ensemble forecasts instead of deterministic ones is indeed a better consistency between consecutive forecasts (Buizza 2008; Zsótér et al. 2009).

One can thus expect a more gradual increase of the probability of an extreme event with decreasing lead time. However, this is not always the case, as a distinctly rapid change in the forecast distribution is sometimes seen between forecasts that are initialized a short time after one another. Such changes are called "forecast jumps" and are usually indicative of a reduced predictability and/or a marked sensitivity of the predicted quantity to the initial conditions (Zsótér et al. 2009).

2.3 Object-based approach

Object-based methods (also referred to as feature-based methods, e.g. Ebert and Gallus Jr. 2009) gained popularity in the last two decades for the verification of quantitative precipitation forecasts (Ebert and McBride 2000; Davis et al. 2006a,b; Wernli et al. 2008; Davis et al. 2009) and have been recently used to analyze other atmospheric features, such as convection (Fowle and Roebber 2003), sea breezes (Case et al. 2004), terrain-induced flows (Nachamkin 2004; Rife and Davis 2005), reflectivity (Marzban and Sandgathe 2008), the jet stream (Limbach et al. 2012), tropical cyclones (Skok et al. 2013) and Rossby waves (Glatt and Wirth 2014; Souders et al. 2014a,b; Wiegand and Knippertz 2014). These methods consider the location, size, shape and magnitude of the chosen atmospheric feature, together with further, feature-specific attributes, and are therefore considerably intuitive to interpret (Ebert and Gallus Jr. 2009).

In contrast to a grid-point-based approach, an object-based one allows to circumvent the "double penalty problem" (Ebert and McBride 2000; Baldwin and Kain 2006; Wernli et al. 2008), which arises in case of a mere displacement of an otherwise well predicted atmospheric feature (see schematic in Figure 2.5). In such case, grid-point-based methods produce a dipole of positive and negative differences between a forecast and the corresponding analysis, thus indicating a low predictability of the given feature, associated with large ensemble spread. Conversely, object-based methods can recognize the role of feature displacement in increasing ensemble spread, isolating it from other factors that reduce predictability and therefore arguably allowing a smarter forecast interpretation.

Object-based methods are suitably applied in a fully automated framework, avoiding any (potentially costly) human intervention. This is especially useful when dealing with large amounts of data, such as those generated through ensemble forecasts. On the other hand, since the identification of objects is often ambiguous (Davis et al. 2006a;

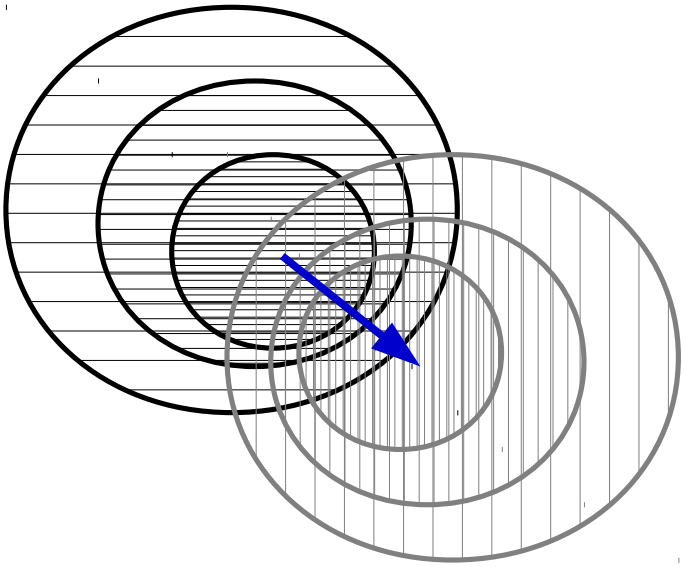

Figure 2.5: *Observed object (black, horizontal hatching) and forecast object (grey, vertical hatching); hatching spacing is inversely proportional to the magnitude of the quantity considered. The thick blue arrow shows the overall displacement of the forecast object with respect to the observed one. Figure was adapted from Figure 1 of Ebert and McBride (2000). Reproduced with permission. Copyright © 2000 Elsevier Science B.V.*

Ebert and Gallus Jr. 2009), a sufficiently robust approach should be used to reduce as much as possible the sensitivity of results to the chosen identification method.

2.4 Tropical transition

The majority of tropical cyclones (TCs) originate over the tropical oceans and are markedly different from extratropical cyclones. Firstly, the energy source of TCs is the imbalance between the warm ocean and the cold upper troposphere, as they often develop in regions of weak baroclinicity, i.e. devoid of strong horizontal temperature gradients, unlike extratropical cyclones which are primarily fueled by baroclinicity. What perhaps most notably distinguishes TCs from other cyclones is their thermal structure, with a warmer core than its surroundings at all altitudes, as opposed to extratropical cyclones which usually have a cold core (with the exception of occluded cyclones, e.g. Palmén and Newton 1969): for this reason, TCs are referred to as warm-core cyclones. The kinematic structure is also substantially different between TCs and extratropical cyclones, with the former having an axisymmetric wind field to first order, while the latter have a distinctly asymmetrical wind field. Lastly, as a result of their thermodynamic structure, TCs often exhibit a small cloud-free region of sinking air at their center referred to as eye, which is not observed in extratropical cyclones.

Despite the considerable differences between TCs and extratropical cyclones, it is not always straightforward to categorize cyclones based on their region of occurrence, appearance, structure and evolution, as they are part of a continuous spectrum. A particularly elusive class is constituted by subtropical cyclones, which exhibit charac-

teristics of both TCs and extratropical cyclones. Forming predominantly at subtropical latitudes, these storms, unlike "pure" TCs, develop in regions of moderate baroclinicity and are generally influenced by the interaction with an upper-level trough (Evans and Guishard 2009; Bentley et al. 2016; da Rocha et al. 2018); but they are also driven by convective redistribution of the heat of the ocean as they evolve (Davis 2010; da Rocha et al. 2018), similarly to "pure" TCs. Since they fall into an intermediate category and are affected by both extratropical and tropical processes, subtropical cyclones are challenging to understand, predict and categorize (Davis 2010).

Most TCs forming at latitudes lower than 20° N require specific environmental conditions for their development, namely sea surface temperature (SST) greater than 26 °C to a depth of at least 50 m, upper-tropospheric divergence, high moisture in the lower and mid-troposphere, weak vertical wind shear (VWS) and a preexisting cyclonic circulation near the surface (see e.g. DeMaria et al. 2001). However, a significant fraction of TCs are first born as extratropical or subtropical cyclones north of 20° N and under considerably different conditions, including moderately high shear, SST lower than 26 °C and low-level baroclinicity (Bracken and Bosart 2000; Davis and Bosart 2003; McTaggart-Cowan et al. 2008, 2013, 2015), to later develop a warm core and transform into TCs through a process known as tropical transition (TT; Davis and Bosart 2003, 2004), essentially evolving in the opposite direction with respect to extratropical transition (Jones et al. 2003; Evans et al. 2017), whereby a TC transforms into an extratropical cyclone.

Although subtropical or extratropical cyclones transitioning into TCs have been observed for at least three decades (e.g. Bosart and Bartlo 1991), Davis and Bosart (2003, 2004) were the first to describe a TT paradigm, analyzing 10 transitioning and 14 nontransitioning cyclones in the Atlantic Ocean (Davis and Bosart 2003), all of which formed under high-shear baroclinic conditions. Baroclinicity is instrumental in promoting the occurrence of organized convection, resulting in the appearance of coherent vortices in the lower troposphere which then extract energy from the warm sea through surface heat fluxes (the wind-induced surface heat exchange effect, Emanuel 1986; Rotunno and Emanuel 1987)]. Convection acts to erode the relatively high initial shear through vertical mixing of absolute momentum; diabatic effects are found to be crucial in redistributing (potential vorticity (PV)) both vertically and horizontally (Davis and Bosart 2003; Hulme and Martin 2009a).

In the early stage of a transitioning cyclone, convection promotes and accelerates the extratropical occlusion process (Hulme and Martin 2009a), whereby the cyclone

attains an equivalent barotropic structure (Palmén and Newton 1969), which in turn favors tropical cyclogenesis and the development of a warm core (Davis and Bosart 2003): Davis and Bosart (2004) remark that, as a rule of thumb, the occluded cyclone should remain over sufficiently warm water for at least one day for a successful TT (this view has been later corroborated by Hulme and Martin 2009a). The nontransitioning cyclones analyzed by Davis and Bosart (2003) failed to simultaneously attain these conditions, as they either moved to a region of cooler water or maintained a high shear as a consequence of the interaction with shortwave troughs which prevented occlusion to complete.

The initial baroclinicity is not important in TT cases for baroclinic energy conversion, but rather for its role in facilitating organized convection and consequently favoring tropical cyclogenesis (Davis and Bosart 2003, 2004). The magnitude of the initial baroclinicity varies considerably among TT events (Davis and Bosart 2003) and a further categorization into strong and weak TT cases – with strong and weak baroclinicity, respectively – carried out by McTaggart-Cowan et al. (2008, 2013) reveals that about 28% of all TCs in the Atlantic result from TT, a higher percentage than for any other basin. This may be explained by more favorable environmental conditions over the Atlantic, owing to a more frequent concurrency of high SST, low-level baroclinicity and upper-level troughs (Davis and Bosart 2003; Hulme and Martin 2009a; McTaggart-Cowan et al. 2013). In view of the extratropical influence on the TT pathway, TCs arising from TT tend to form at higher latitudes (Bentley et al. 2016) and be weaker (McTaggart-Cowan et al. 2008) compared with nonbaroclinic TCs.

The importance of upper-level (possibly cut-off) troughs reaching subtropical latitudes for the TT cyclogenesis pathway was first pointed out by Davis and Bosart (2003, 2004) and later confirmed by Hulme and Martin (2009a) and Bentley et al. (2017). These synoptic-scale features are generally linked with Rossby wave breaking (Thorncroft et al. 1993) and have been shown to be associated with a significant fraction of TC events in the Atlantic (McTaggart-Cowan et al. 2013; Galarneau Jr. et al. 2015), including TT events (Hulme and Martin 2009a). The interaction between the trough and a preexisting extratropical or subtropical cyclone with an associated low-level baroclinic region appears instrumental in promoting organized convection (Hulme and Martin 2009a,b) through both a steeper lapse rate underneath the trough and quasi-geostrophic forcing of vertical motion (Bentley et al. 2017), and distinguishes TT from other pathways of tropical cyclogenesis that are affected by baroclinicity (McTaggart-Cowan et al. 2008, 2013). It is worth noting that the intrusion of upper-level troughs

in the tropics (south of 20° N), with associated relatively cold upper-tropospheric air, appears instead to have an adverse effect on tropical cyclogenesis from African easterly waves (Zhang et al. 2016).

It is evident that TT is, by its very nature, a multiscale phenomenon, resulting from the interaction between both extratropical and tropical processes. This has consequences on predictability, as pointed out by Wang et al. (2018), who applied the categorization by McTaggart-Cowan et al. (2013) to Global Ensemble Forecast System reforecasts to examine the extratropical influence on Atlantic TC activity. These authors highlight the lower predictability of TT events with respect to other TCs, attributing it to the higher forecast errors for VWS and 700-hPa relative humidity as well as the fact that the extratropical atmosphere has generally a lower predictability – with a faster error growth – than the tropical atmosphere for mid-range forecasts, which deteriorates the predictability of TCs with a strong extratropical influence. Wang et al. (2018) also interpret the lower predictability of TT events in terms of a theoretical genesis potential index (e.g. Emanuel and Nolan 2004) for tropical cyclogenesis, which is generally obtained as a multiplication of factors corresponding to relevant TC genesis predictors: as the TT pathway depends on a complex interaction between large-scale and mesoscale, extratropical and tropical processes, it is likely sensitive to a larger number of factors, and has therefore lower predictability, than nonbaroclinic TC pathways.

While TCs arising from TT occur most frequently in the Atlantic (McTaggart-Cowan et al. 2013), the occurrence of tropical-like cyclones (TLCs) in the Mediterranean Sea has been linked to the TT pathway (Moscatello et al. 2008a; McTaggart-Cowan et al. 2010a,b; Chaboureau et al. 2012b; Mazza et al. 2017). Specifically, McTaggart-Cowan et al. (2010a,b) highlight the analogies between the Mediterranean, "Gulf of Genoa"-type cyclone which underwent TT in November 2007 and TT events in the Atlantic, most notably the reduction of VWS through convective transport of horizontal momentum and the prevalence of diabatic energy over baroclinic energy in driving cyclogenesis, in addition to the development of a warm core. Both Moscatello et al. (2008a) and McTaggart-Cowan et al. (2010a,b) point out the strong influence of the Mediterranean orography on the cyclone's development and intensification: the lack of a vast, uninterrupted body of water such as a major ocean is indeed, together with the lower Mediterranean SST with respect to the subtropical Atlantic, a significant factor in setting apart Mediterranean TT events from the Atlantic ones. In the next section, Mediterranean TLCs – generally referred to as Medicanes – will be introduced and an overview of our knowledge of these storms will be provided.

2.5 Medicanes

The existence of Mediterranean cyclones bearing a similarity to TCs was first observed in the 1980s (Billing et al. 1983; Ernst and Matson 1983; Mayengon 1984; Rasmussen and Zick 1987). In particular, Rasmussen and Zick (1987) analyzed a 1983 Medicane and remarked on the fact that, with deep convection influencing its formation and by virtue of its small size and warm core, this cyclone resembled polar lows, which had already gained attention in the meteorological community (e.g. Rasmussen 1979). In fact, an analogy to hurricanes has been drawn for both Medicanes and polar lows, in view of their common tropical-like traits and formation mechanisms, such as the large thermodynamic disequilibrium between (relatively) warm sea and cold air in which both these types of cyclones develop (Rasmussen et al. 1992; Emanuel 2005), the strong influence by surface fluxes (Emanuel and Rotunno 1989; Lagouvardos et al. 1999), the warm core, the eye-like feature (Businger and Reed 1989; Bresch et al. 1997) and the small size due to the high values of the Coriolis parameter f at extratropical latitudes (Emanuel and Rotunno 1989). The distinguishing factor of Medicanes and polar lows with respect to the majority of cyclones occurring at extratropical latitudes is essentially the fact that these cyclonic vortices can potentially be sustained by air-sea interaction mechanisms[5] (Emanuel and Rotunno 1989; Bresch et al. 1997; Homar et al. 2003; Emanuel 2005).

2.5.1 Development pathways

Medicanes generally form in the strongly unstable environment associated with a cold upper-level trough and a PV streamer (Lagouvardos et al. 1999; Emanuel 2005; Fita et al. 2007; Cavicchia et al. 2014a; Cioni et al. 2016; Miglietta et al. 2017), which is the result of Rossby wave breaking over western Europe (Tous and Romero 2013; Tous et al. 2013). The large thermodynamic imbalance between relatively warm sea and cold air aloft triggers air-sea instability and promotes cyclogenesis (Lagouvardos et al. 1999; Homar et al. 2003; Emanuel 2005; Carrió et al. 2017; Fita and Flaounas 2018). The upper-level trough appears to play a crucial role for the intensification during the early stage of Medicanes (Homar et al. 2003; Emanuel 2005; Miglietta et al. 2017) as well as for their maintenance at a later time (Carrió et al. 2017; Fita and Flaounas 2018).

[5] Warm-core TLCs can also rarely occur over much smaller water bodies, such as the September 1996 "Hurricane Huron" analyzed by Sousounis et al. (2001).

While a PV streamer originating from Rossby wave breaking and penetrating into the Mediterranean is linked to the majority of intense Mediterranean cyclones, including Medicanes (Flaounas et al. 2015; Raveh-Rubin and Wernli 2015), Fita and Flaounas (2018) observe that the PV streamer tends to behave differently for Medicanes, generally developing into a cut-off instead of wrapping around the cyclone. This produces a long-lasting unstable environment, reducing shear and enhancing the lapse rate, thus promoting organized convection – a common evolution pathway for most, if not all, subtropical cyclones (Bentley et al. 2017; da Rocha et al. 2018) including TT cases (Hulme and Martin 2009a).

Similarly to subtropical cyclones, Medicanes generally form in a low-level baroclinic environment (Miglietta et al. 2017; da Rocha et al. 2018). Baroclinic processes have been shown to play an important role for the early development of Medicanes (Lagouvardos et al. 1999; Mazza et al. 2017; Carrió et al. 2017; Pytharoulis 2018), as a result of the strong interaction with the upper-level through, which promotes cyclogenesis and air-sea instability (Lagouvardos et al. 1999; Cioni et al. 2016; Miglietta et al. 2017). On the other hand, the role of baroclinicity in maintaining Medicanes is not as clear-cut: while it is not a necessary ingredient (Emanuel 2005), as shown for numerous cases (Homar et al. 2003; Fita et al. 2007; Moscatello et al. 2008a), it can be important in some other cases, as shown by Miglietta and Rotunno (2019) for the 2005 Medicane. Some authors (Mazza et al. 2017; Fita and Flaounas 2018) have suggested that Medicanes can actually develop a warm core through warm seclusion, which is typical of mature baroclinic extratropical cyclones, thus exhibiting a marked baroclinic influence throughout their existence.

What sets Medicanes apart from other intense Mediterranean cyclones is the crucial role played by surface heat fluxes and convection in cyclone intensification and maintenance. Specifically, there is a consensus that surface heat fluxes and latent heat release are instrumental in causing the initial low to intensify during its early stage (Lagouvardos et al. 1999; Pytharoulis et al. 2000; Homar et al. 2003; Moscatello et al. 2008a; Davolio et al. 2009; Tous et al. 2013; Miglietta et al. 2017; Mazza et al. 2017; Miglietta and Rotunno 2019)[6]. The important role of surface fluxes is confirmed by sensitivity studies showing that higher SST causes the tropical-like stage of Medicanes to be longer and more marked, while the opposite is true for lower SST (Miglietta et al. 2011; Pytharoulis 2018); Miglietta et al. (2011) note that lower SST also delays the

[6] Lagouvardos et al. (1999) observe that latent and sensible heat contribute equally to surface fluxes, as seen also for polar lows (Rasmussen 1979).

development of deep convection, to the point that no tropical-like stage is observed for strongly reduced SST. Some authors go as far as to suggest that Medicanes may be maintained predominantly through surface fluxes and air-sea interaction during their mature stage (Homar et al. 2003; Emanuel 2005; Fita et al. 2007; Miglietta and Rotunno 2019), though Miglietta and Rotunno (2019) point out that the importance of air-sea interaction is case-dependent, while Carrió et al. (2017) observe that surface fluxes and latent heat release are not so important individually, but rather in synergy with the upper-level trough.

Moisture also plays an important role in Medicane development, as first remarked by Fita et al. (2007), who show that high moisture content throughout the troposphere prior to Medicane formation has a strong impact on the subsequent evolution of the cyclone, despite not being a necessary ingredient for its formation. Cavicchia et al. (2014a) also observe, from a climatological viewpoint, that a high mid-tropospheric moisture content is one of the environmental ingredients associated with the occurrence of Medicanes, similarly to TCs (DeMaria et al. 2001). Moisture content affects the timing and magnitude of deep convection, which generally peaks during the early intensification stage of Medicanes (Claud et al. 2010; Miglietta et al. 2013; Cioni et al. 2018; Dafis et al. 2018), while decreasing afterwards (Fita and Flaounas 2018). The latent heat released through convection contributes not only to the intensification, but also to the contraction of the cyclone (Moscatello et al. 2008a; Carrió et al. 2017).

Numerous factors can influence the development of Medicanes. First, as Fita et al. (2007) point out, the Mediterranean Sea is considerably different from the subtropical oceans, due to its small size, relatively high latitude and low SST as well as the abundant orography surrounding and within the region. As a result, local processes can significantly affect the evolution of Medicanes (Flaounas et al. 2015), as observed evidently for the events of October 1996 and September 2006. The 1996 event is analyzed by Miglietta and Rotunno (2019), who highlight the strong influence of cold, dry low-level winds intruding the Mediterranean from Spain and France on the cyclone's intensification. The 2006 Medicane is analyzed by Moscatello et al. (2008a) and Miglietta et al. (2015), who stress the impact of 1) the Atlas mountains on the development of the cyclone and 2) the orography of Calabria on the intensity and location of convection and therefore on the evolution of the cyclone. The 2006 Medicane was also influenced by its interaction with 1) a cold front, which promoted convection through frontal uplift (Miglietta et al. 2011), and 2) the jet stream, which enhanced upward forcing once the cyclone crossed it, accelerating the development of

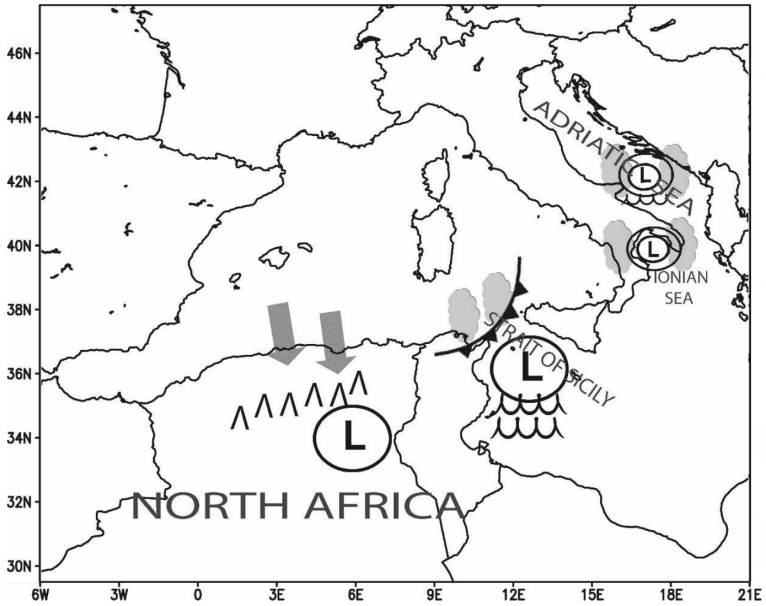

Figure 2.6: *Different stages of the evolution of the 2006 Medicane. The chain of events leading to the small-scale vortex over southern Italy began with northerly flow (gray arrows) impinging on the Atlas Mountains (∧ symbols) and producing an orographic cyclone on the lee side ("L" stands for pressure low). As the cyclone moved eastward and reached the Strait of Sicily, its interaction with a cold front promoted the development of convection (represented by the gray clouds) nourished by sea surface fluxes (represented by the wave symbols). Such interaction transformed the orographic vortex into an intense smaller-scale vortex (represented by the higher number of circles around the L), which deepened further due to convection over the Ionian Sea and was maintained by both convection and sea surface fluxes as it remained in the Adriatic Sea. Figure and caption were adapted from Moscatello et al. (2008a). Reproduced with permission. © American Meteorological Society.*

the storm's warm core (Chaboureau et al. 2012b). Moscatello et al. (2008a) point out the similarity between the evolution of this Medicane and that of cyclones undergoing TT; in both cases, an intermediate process acts to increase mesoscale vorticity, organize convection and ultimately produce a self-sustaining vortex (Davis and Bosart 2004): a role fulfilled by the interaction with orography and the cold front for the 2006 Medicane, as shown schematically in Figure 2.6.

2.5.2 Definition

The complex pathway leading to the occurrence of Medicanes, with the interaction and feedback between multiple processes at different scales, explains the high case-to-case variability and perhaps also the lack of an objective, unanimous definition of these cyclones (Tous et al. 2016; Miglietta et al. 2017; Fita and Flaounas 2018; Miglietta and Rotunno 2019). In particular, Fita and Flaounas (2018) and Miglietta

and Rotunno (2019) acknowledge that Medicanes cannot be fit into a single, uniform category of cyclones and propose two alternative ways of characterizing them. Fita and Flaounas (2018) propose to categorize Medicanes *a priori* as subtropical cyclones, given that they occur at a sufficiently low latitude, (may) exhibit both extratropical and tropical features and are dynamically linked to PV streamers. Miglietta and Rotunno (2019) propose an *a posteriori* categorization into three classes: one for events where air-sea interaction and surface fluxes effects prevail over baroclinic processes; one for events where both effects are important throughout the cyclone's evolution; and a last class containing all Medicanes that strongly interact with other features such as orography, fronts or the jet stream. As Miglietta (2019) points out, further investigation is necessary to test this categorization and better assess the contribution of all factors to Medicane development.

Medicanes remain elusive cyclones, owing to their occurrence over the sea, where observations are sparse, and their small scale (few hundred km in diameter, down to 60 km for the 2006 event; Chaboureau et al. 2012b), which poses a challenge also for their detection (Picornell et al. 2014). The conditions for a cyclone to be considered a Medicane are consistently defined in the literature: 1) a nearly perfect cyclone thermal symmetry, and 2) a positive lower-level and upper-level thermal wind, corresponding to a lower-level and upper-level warm core (Miglietta et al. 2011; Cavicchia et al. 2014a; Picornell et al. 2014). These conditions are computed by means of the cyclone phase space (CPS) originally developed by Hart (2003), which provides a quantitative estimate of the cyclone's thermal structure, to identify Medicanes in (re)analysis and model data (the CPS is widely used in this thesis and illustrated in detail in Section 4.4). CPS parameters are to be computed in a circle around the cyclone's center; while Hart (2003) uses a 500 km radius, a smaller radius of 150 km or less has been preferred for Medicanes given that they are generally smaller and weaker than TCs (Fita et al. 2007). Picornell et al. (2014) additionally enforce a constraint on pressure gradient, which is required to be larger than 3.2 hPa/100 km in at least 6 out of 8 radial directions; while Cavicchia et al. (2014a) impose further constraints on wind, which is required to exceed 18 ms^{-1} within 50 km from the cyclone center and be more intense at 850 hPa than at 300 hPa. As a result of 1) the use of different constraints and thresholds by different authors and 2) the sensitivity of CPS parameters to the chosen radius and the spatial extent of the cyclone's warm core, a specific cyclone may or may not be considered a Medicane.

2.5.3 Climatology and features

The high variability of Medicane intensity, seasonality and occurrence regions was first pointed out by Claud et al. (2010), while Miglietta et al. (2013) noted that these storms tend to occur in two sub-basins of the Mediterranean, i.e. around the Balearic Islands and in the Ionian Sea. This was confirmed by Cavicchia et al. (2014a), who produced the first climatology of Medicanes for the period 1948–2011, by downscaling NCEP –National Center for Atmospheric Research reanalysis data. These authors highlight the low frequency of Medicanes, about 1.6 events per year, with a maximum in winter, a minimum in summer and autumn having more events than spring. Cavicchia et al. (2014a) also observe that the frequency of the environmental conditions associated with Medicane development – namely, low shear, large mid-tropospheric moisture content and high low-level vorticity – is spatially and temporally similar to the frequency of Medicanes themselves. Nastos et al. (2018) also identify the western Mediterranean and the Ionian Sea as preferential regions and estimate a similar Medicane frequency to Cavicchia et al. (2014a) – 1.4 events per year – but find a maximum in September, with considerable interannual variability. Miglietta and Rotunno (2019) attribute the higher Medicane frequency in the western Mediterranean to the frequent intrusion of cold, dry continental airmasses into the sea in this region, which enhances air-sea interaction effects.

Medicanes may form as canonical extratropical cyclones in the first place, exhibiting a vertical tilt and frontal structures (Mazza et al. 2017). The duration of the early extratropical phase is highly variable and strongly depends on the development pathway (Miglietta et al. 2017). Although TLCs are a wide category, with a broad range of durations, intensities and sizes (Miglietta et al. 2013), mature Medicanes exhibit common distinctive traits, such as: 1) a warm core; 2) strong surface fluxes, associated with a low-level vorticity maximum with more intense surface winds than upper-level winds (Pytharoulis et al. 2000; Reale and Atlas 2001); 3) a high pressure gradient (Picornell et al. 2014); 4) a smaller size and weaker intensity compared with TCs (Fita et al. 2007; Chaboureau et al. 2012b); 5) a similar spatial distribution of deep convection and lightning activity to TCs (Dafis et al. 2018), in contrast with a peak of convection and rainfall during the early intensification stage rather than during the mature stage as for TCs (Claud et al. 2010; Fita and Flaounas 2018).

The following features have been reported for individual Medicanes, although there is no evidence that they can be observed for all Medicanes: 1) explosive intensification, with a rapid mean sea level pressure (MSLP) fall (Moscatello et al. 2008a; Cioni et al.

2018); 2) virtually perfect vertical alignment of the cyclone (Reale and Atlas 2001); 3) an eye-like feature at the center of the cyclone, with weak or absent winds, surrounded by spiralling clouds (Pytharoulis et al. 2000; Reale and Atlas 2001; Moscatello et al. 2008a; Cioni et al. 2018); 4) a surface wind maximum at the eyewall, observed for the 2006 Medicane by Moscatello et al. (2008b); 5) a tropospheric-deep PV tower, highlighted for the same event by Chaboureau et al. (2012b). Fita et al. (2007) report a record sustained wind speed of 40 ms^{-1} for Medicanes, noting that they can occasionally reach tropical storm intensity. A record minimum pressure of 979 hPa was reached by storm Qendresa (November 2014), one of the eight events analyzed in this thesis, which also exhibited a pressure drop of 20 hPa in 6 hours and wind gusts of nearly 43 ms^{-1} (all measurements taken in Malta, see Carrió et al. 2017; Cioni et al. 2018). Qendresa exhibited an eye for some time during its mature stage, with spiralling clouds (see the satellite image in Figure 2.7) and weaker, descending motion in the vicinity of its center, as diagnosed by Cioni et al. (2018) and shown in Figure 2.8.

A few studies have focused on Medicanes in future climate, a crucial issue considering that these storms can cause significant damage in the densely populated coastal regions of the Mediterranean (Tous and Romero 2013; Cavicchia et al. 2014a), which is itself highly vulnerable to future climate change (e.g. Giorgi and Lionello 2008). There is a consensus that the overall frequency of Medicanes will decrease, but the strongest Medicane intensity is predicted to moderately increase (Romero and Emanuel 2013; Cavicchia et al. 2014b; Walsh et al. 2014; Tous et al. 2016; Romero and Emanuel 2017). In particular, Walsh et al. (2014) highlight a predicted general decrease in the

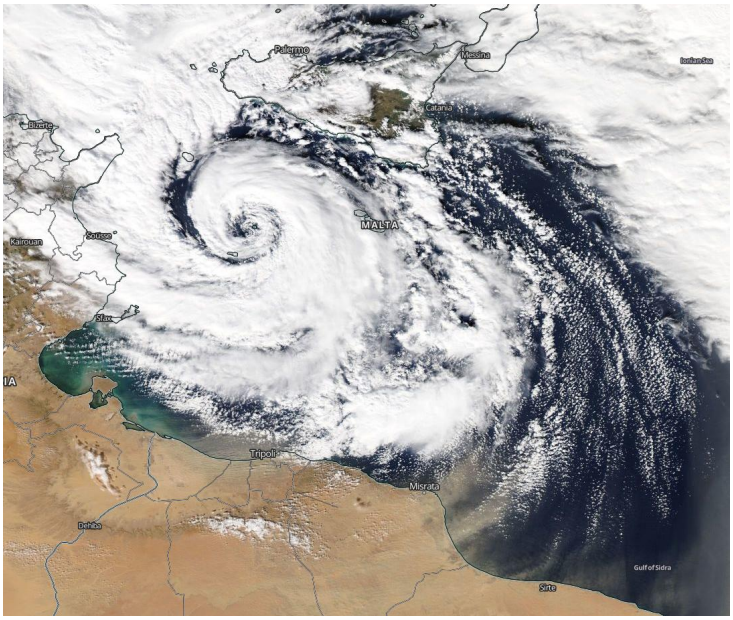

Figure 2.7: *False-color image of Medicane Qendresa captured by NASA's Moderate Resolution Imaging Spectroradiometer (MODIS) Aqua satellite at 1215 UTC on November 7, 2014. The picture was captured around the time Qendresa reached its highest intensity; some of its tropical-like traits are evident, such as spiralling clouds, a high axial symmetry and a small cloud-free region at the center of the cyclone, resembling the eye of a hurricane.*

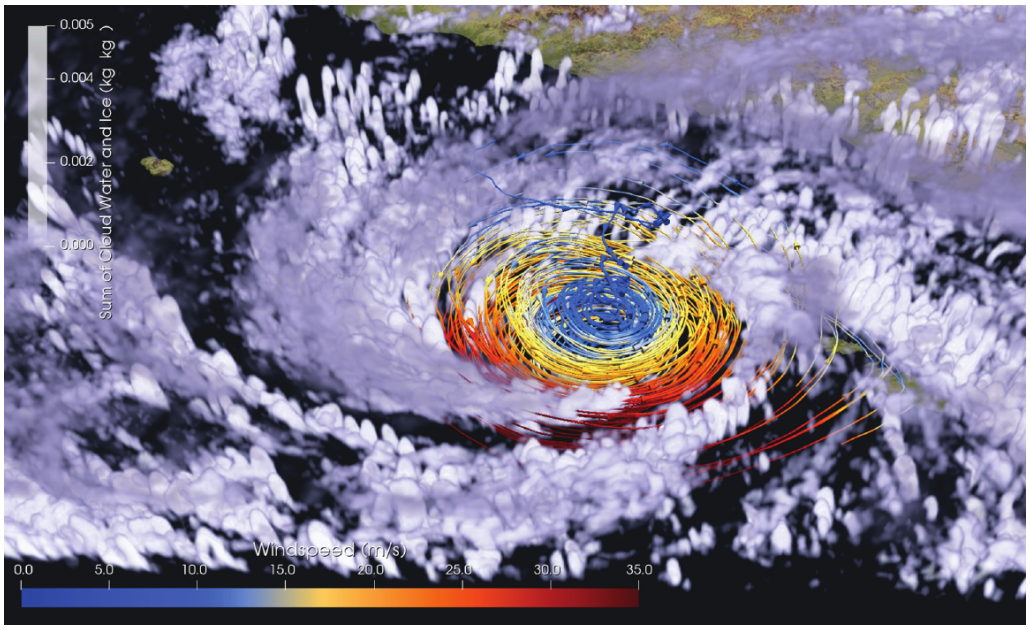

Figure 2.8: *High-resolution simulation of cyclone Qendresa; forecast time is 1400 UTC on November 7, 2014. The sum of cloud water and cloud ice mixing ratios (kg kg^{-1}) is shown as grey-white shading; forward-backward time-integrated trajectories of air parcels are colored according to wind speed (ms^{-1}). Figure was taken and caption adapted from Cioni et al. (2018). Reproduced with permission. © 2018 Royal Meteorological Society.*

frequency of all types of Mediterranean cyclones, while observing that Medicanes will likely become less frequent due to a lower frequency of the environmental factors that are conducive to Medicane development, such as low shear and maximum potential intensity (Bister and Emanuel 1998). Gaertner et al. (2007) remark on the large uncertainty of future climate simulations, but point out the risk of a fully tropical cyclone occurring in the Mediterranean in the future.

2.5.4 Predictability

Predicting Medicanes is challenging, owing to the complex multiscale pathway leading to their development and the large case-to-case variability. Numerous studies have focused on the simulation of individual events or small sets of events using either high-resolution, non-hydrostatic models (e.g. Fita et al. 2007; Davolio et al. 2009; Miglietta et al. 2011; Chaboureau et al. 2012a,b; Cioni et al. 2016; Carrió et al. 2017; Cioni et al. 2018; Fita and Flaounas 2018; Pytharoulis 2018; Miglietta and Rotunno 2019) or models with parameterized convection (e.g. Lagouvardos et al. 1999; Homar et al. 2003; Moscatello et al. 2008a; Miglietta et al. 2013; Tous et al. 2013; Akhtar et al. 2014; Miglietta et al. 2015, 2017; Pytharoulis et al. 2017). A horizontal grid

spacing of less than 10 km appears to be necessary to resolve the fine-scale features of Medicanes (Akhtar et al. 2014; Miglietta et al. 2015; Cioni et al. 2016, 2018).

Numerous studies highlight a strong sensitivity of Medicane simulations to the initial conditions (Fita et al. 2007; Moscatello et al. 2008a; Davolio et al. 2009; Chaboureau et al. 2012a,b; Cioni et al. 2016). Other studies have reported a marked sensitivity to horizontal resolution (Akhtar et al. 2014), microphysical and boundary layer schemes (Miglietta et al. 2015; Ricchi et al. 2019) and initialization time, with simulations initialized prior to cyclone formation being more accurate than those initialized afterwards (Cioni et al. 2016). The intensity and structure of the cyclone appear to be highly sensitive to its trajectory (Miglietta et al. 2015; Cioni et al. 2016). Pytharoulis et al. (2017) observe, in the context of a case study, that no model setup is optimal and capable of reproducing all traits of the cyclone.

Medicane simulations have occasionally exhibited systematic errors, such as a tendency for the simulated cyclones to be stronger and last longer than the observed cyclones (Fita et al. 2007), a temporal delay with respect to observations (Moscatello et al. 2008a) or an underprediction of cyclone intensity (Chaboureau et al. 2012b). Furthermore, even relatively short-range weather forecasts sometimes fail to predict the occurrence of Medicanes (Chaboureau et al. 2012b; Pantillon et al. 2013). While ensemble forecasts can be underdispersive, with only a fraction of members predicting a fully developed Medicane (Chaboureau et al. 2012a), ensemble prediction has been successfully used to analyze TT for a Medicane event (Mazza et al. 2017) and has shown to be a valuable resource to alert operational forecasters to Medicane occurrence (Pantillon et al. 2013), which can consistently appear in some ensemble members up to a few days in advance.

Chapter 3

Research questions

In the previous chapter, the development pathways and characteristics of Medicanes were illustrated, placing these cyclones into the broader context of TT. Despite occurring at the midlatitudes, Medicanes can exhibit the traits of both extratropical and TCs and are therefore difficult to categorize. In addition to this, the occurrence of these storms is affected by a multitude of meteorological processes at various spatial and temporal scales. For these reasons, the successful prediction of Medicanes constitutes a considerable challenge for both operational weather forecasters and numerical weather prediction systems. In the previous chapter, ensemble prediction was also introduced as a powerful means to obtain better weather forecasts and its benefits were discussed, including a more meaningful representation of uncertainty and an increased effectiveness in predicting extreme weather events. This thesis aims at bridging a gap, carrying out the first systematical assessment of Medicane predictability through the evaluation of ECMWF operational ensemble forecasts of eight recent TLCs: seven Medicanes and a cyclone that occurred over the Bay of Biscay.

The eight events are first characterized in terms of their antecedent dynamics, kinematics and thermal structure by using ECMWF operational analysis data. This part of the study (Chapter 5) addresses the following research questions (RQs):

RQ 1 How do Medicanes fit into the TT paradigm?

- **RQ 1a** What similarities and differences can be found between the TT development pathway and that of Medicanes?
- **RQ 1b** How can Medicanes be best categorized? Is a new, ad-hoc category necessary?

After this preliminary analysis, a first insight into Medicane prediction is provided in Chapter 6, Section 6.1, where the focus is the overall predictability. The extremeness of the eight Medicane cases is first assessed in Subsection 6.1.1 by using two forecast indices that compare ensemble forecasts to model climatology. The prediction of Medicane occurrence, position, intensity, kinematic and thermal structure is then examined in the following subsections. In this part of the thesis, the following questions are addressed:

RQ 2 How are Medicanes reproduced in ECMWF ensemble forecasts?

- **RQ 2a** Are Medicanes extreme events with respect to model climatology?
- **RQ 2b** How accurately are Medicanes represented in these forecasts? Are there systematic errors?
- **RQ 2c** Which Medicane aspects exhibit higher and lower predictability? What are the respective forecast horizons in terms of lead time?

In this section, particular attention is given to forecast uncertainty and its evolution with lead time, addressing the following research questions:

RQ 3 How can uncertainty be characterized in spatio-temporal ensemble data sets?

- **RQ 3a** How is uncertainty best represented for non-trivial, cyclone-relative quantities?
- **RQ 3b** How does uncertainty evolve with lead time?
- **RQ 3c** For which quantities is the largest uncertainty found in Medicane forecasts?

Finally, the attention is shifted to the large-scale dynamics, with a focus on the dynamical structures that typically precede Medicanes, producing a conducive environment to their development: Rossby waves (RWs) – namely, RW packets and RW breaking – and upper-level troughs. The aim of this part of the thesis (Section 6.2) is to study the predictability of precursor processes on the one hand, and identify a linkage

between these processes and cyclone predictability on the other hand, addressing the following research questions:

RQ 4 To what extent is the predictability of Medicanes linked to antecedent planetary-scale and synoptic-scale dynamics?

RQ 4a What is the influence of RWs on Medicane occurrence and thermal structure and how predictable are they?

RQ 4b How do the presence and position of an upper-level trough determine or affect Medicane occurrence and structure?

The results are discussed in detail in Chapters 5 and 6 and a final summary is given in Chapter 7, where research questions are answered and outlook is provided on further research directions.

Chapter 4

Data and methods

In this chapter, a description is provided of the methods and techniques that are used to analyze ECMWF operational analysis and ensemble forecast data and apply the object-based approach introduced in Chapter 1. The data used are first described. It is then illustrated how RW packets and RW breaking objects are defined, identified and characterized. A description of the detection and tracking of MSLP lows in both analysis and ensemble data follows. Forecast cyclones are matched non-linearly in time to the reference cyclone in the analysis, maximizing the similarity of the trajectories by virtue of a dynamic time warping (DTW) technique, which is thoroughly explained along with its advantages over a time-linear matching approach. Forecasts are evaluated over a time window as opposed to a fixed forecast time: the choice of the time window depends on the cyclone's intensity as well as dynamical and thermal structure measured by suitable parameters. A brief illustration of Principal Component Analysis is also provided. The chapter is concluded with a short description of the graphics used in evaluating the ensemble forecast statistics.

4.1 Data

ECMWF operational analysis data is used as reference data to verify ensemble forecasts, which are initialized twice daily (at 0000 and 1200 Universal Time Coordinate (UTC)) and consist of 50 perturbed forecasts or members and a control forecast. Data is available every 6 hours for both analysis and ensemble data.

Both the high-resolution (HRES), deterministic model, which is used to generate analysis data, and the ensemble prediction system (ENS) have undergone some changes during the time period considered in this study (2011–2017). Between 2011 and early

2016, horizontal grid spacing is 16 km for the HRES model and 32 km for the ENS; afterwards, grid spacing decreases to 9 km for the HRES model and 18 km for the ENS. Five and three events, respectively, occurred during these two time periods (see also Table 5.1 in Chapter 5). Vertical resolution also changed for both the HRES model and the ENS during the analyzed time period. The reader is referred to the ECMWF web page for a detailed documentation of model changes and updates: https://www.ecmwf.int/en/forecasts/documentation-and-support/changes-ecmwf-model.

Two severe forecast indices developed at the ECMWF are also used: the Extreme Forecast Index (EFI; Lalaurette 2003) and the Shift Of Tails (SOT) index (Zsótér 2006). While a brief description of these indices is provided here, the reader is referred to the articles cited above for a more detailed explanation. The main strength of the EFI and SOT is the fact that no preexisting observation climatology is required, such that they can be used even in regions where observations are unavailable (Prates and Buizza 2011).

The EFI measures the difference between the ensemble forecast distribution and the model climatology and is defined as follows:

$$\mathrm{EFI} = \frac{2}{\pi} \int_0^1 \frac{p - F_f(p)}{\sqrt{p(1-p)}}\, dp\,, \tag{4.1}$$

where p represents a quantile of the model climatology distribution and $F_f(p)$ is the fraction of ensemble members below such quantile. High values of EFI can arise from either a few members having extreme values or most members having moderately anomalous values. The EFI ranges from -1 to 1, corresponding to extreme forecasts in the negative and positive direction, respectively.

The SOT index measures the level of abnormality in the upper (SOT_+) or lower (SOT_) tail of the ensemble forecast distribution and is defined as follows:

$$\mathrm{SOT}_+(p) = -\frac{Q_f(p) - Q_c(1)}{Q_c(p) - Q_c(1)}\,, \tag{4.2}$$

$$\mathrm{SOT}_-(p) = -\frac{Q_f(p) - Q_c(0)}{Q_c(p) - Q_c(0)}\,, \tag{4.3}$$

where $Q_c(p)$ and $Q_f(p)$ are the p quantile of the model climatology and the forecast distribution, respectively, so that $Q_c(0)$ and $Q_c(1)$ correspond to the lowest and highest value of the climatology. The 0.9 quantile is used in this thesis. As the SOT_+ [SOT_] index is defined on distribution tails, it is only sensitive to extreme forecasts, equalling

0 when the chosen quantile of the forecast distribution equals the highest [lowest] value of the climatology and attaining positive [negative] values when the quantile exceeds it. The ECMWF calculates EFI and SOT with respect to several forecast time windows: the one-day window (e.g. 24–48 forecast hours) is used in this thesis.

4.2 Rossby waves

The amplitude of RWs exhibits a strong zonal asymmetry, with regions of high amplitude generally referred to as RW packets or trains (Wirth et al. 2018). Since RW breaking associated with an upper-level trough is usually a synoptic-scale dynamical precursor to Medicanes (Subsection 2.5.1), RW predictability – specifically, that of RW packets and RW breaking – is investigated in this thesis by means of an object-based approach. The definition, detection and characterization of RW packets is provided in subsection 4.2.1, while that of RW breaking objects is given in subsection 4.2.2. Hereafter, RW packets and RW breaking objects will be collectively referred to as RW objects in case no distinction is necessary.

4.2.1 Rossby wave packets

The method used to identify RW packets was developed by Wolf and Wirth (2015, 2017) and employs as input variable upper-level (300 hPa) wind on a $1° \times 1°$ global regular grid at 12-hour intervals. The background wind field is calculated by using a 30-day low-pass filter and wind anomaly is expressed at any output time as the difference between the full and background wind field.

The background field is interpreted as the waveguide along which RW packets propagate. The projection of wind anomalies perpendicular to the background field, referred to as $v_\perp$ and representing the wave signal, is used to compute the RW envelope following the method of Zimin et al. (2006). However, this method requires an almost plane wave as input variable and RWs often fail to meet this condition, as ridges are generally wider than troughs. To tackle this issue, a semigeostrophic coordinate transformation (Wolf and Wirth 2015) is therefore applied to $v_\perp$ before the wave envelope is computed.

For an almost-plane wave, the wind anomaly associated with a RW packet can be written as:

$$v_\perp(x) = A(x)C(x) \tag{4.4}$$

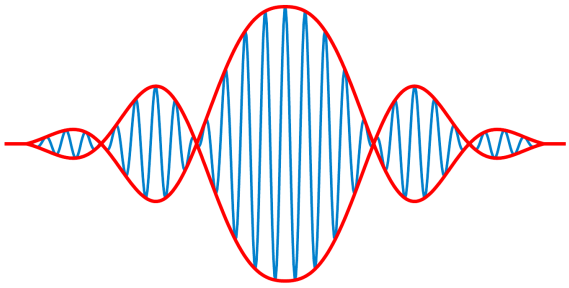

Figure 4.1: *Simple schematic of a wave packet: the carrier wave $C(x)$ is shown in blue, the wave envelope $A(x)$ in red.*

where x is the distance along a streamline of the background field, $C(x)$ is the so-called carrier wave and $A(x)$ is the amplitude of the RW packet, i.e. the wave envelope, which is always positive and varies on a much larger distance than $C(x)$. In the simplest idealized case, represented in Figure 4.1, the carrier wave can be expressed as a simple sine function: $C(x) = \sin(sx)$ where s is the wavenumber; in reality, a RW packet contains all wavenumbers in a specific range: $4 < s < 15$ is used here.

In order to extract RW packets as objects from the wave envelope, which is a continuous field, a double threshold is used, following Wolf and Wirth (2017): a coherent region of envelope values above the first (lower) threshold constitutes a search area, in which a RW packet is identified as the (not necessarily contiguous) region where the envelope value exceeds the second (higher) threshold, as shown in Figure 4.2. As the magnitude of RW packets strongly depends on the season (Glatt and Wirth 2014; Wolf et al. 2018), both thresholds are based on an arctangent function of the average magnitude of the envelope in the extratropical Northern Hemisphere, allowing a single threshold definition for all seasons. The use of a double threshold is motivated by the fact that the RW packet identification method was originally designed to also track RW packets, according to their spatial overlap between consecutive time outputs. In this thesis, RW packet tracking is only used to determine the duration and trajectory of the precursor RW packet for each Medicane event (see Chapter 5). For details about the threshold calculation and RW packet tracking, the reader is referred to Wolf and Wirth (2017). Finally, the position of a RW packet is computed at each time output as its “center of mass”, using the envelope field value for weighting.

RW packets are identified in both analysis and ensemble forecast data and characterized by the following properties, whose forecast statistics are discussed in Chapter 6: occurrence, position, area, magnitude, distance between the RW packet position and that of the Medicane, closest distance between the RW packet and the cyclone (defined as the shortest distance between any RW packet grid point and the cyclone), easternmost longitude, zonal extent (i.e. the difference between the longitude of the

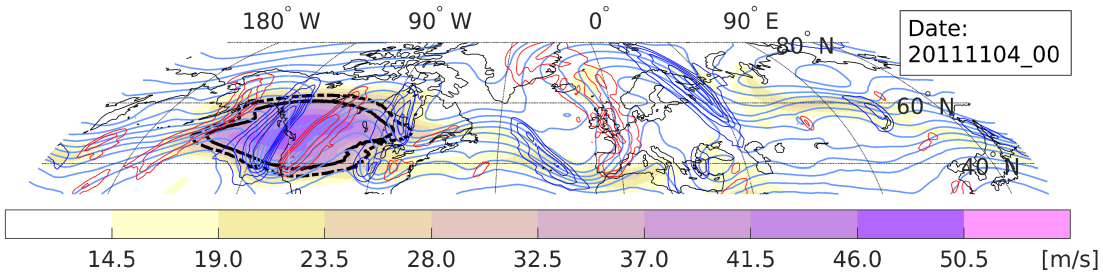

Figure 4.2: *Example plot of RW packets and the quantities used for their identification: meridional wind, shown as thin blue (red) contours for negative (positive) values between 20 ms^{-1} and 60 ms^{-1} absolute value, in 10 ms^{-1} intervals; streamlines of the background wind field, shown as light blue contours; the wave envelope field in shading; the search area, denoted by the dashed thick black line and comprising envelope values above the first (lower) threshold of (in this particular case) 24.0 ms^{-1}; and the RW packet, denoted by the continuous thick black line and comprising envelope values above the second (higher) threshold of 30.0 ms^{-1}. In this case, related to Medicane Rolf (see Chapter 5), a single RW packet is found over North America 60 hours prior to the Medicane development.*

easternmost point and that of the westernmost point), northernmost latitude, and meridional extent (i.e. the difference between the latitude of the northernmost point and that of the southernmost point). For each Medicane event, the associated RW packet is tracked back in time from its last position to determine its trajectory and its position at the time it forms: for this reason, there is no distance constraint with respect to the Medicane to define RW packet occurrence. An area constraint is imposed, discarding RW packets smaller than 250 000 km square kilometers.

4.2.2 Rossby wave breaking

The method used to identify RW breaking objects is adapted from Rivière (2009), which in turn follows Strong and Magnusdottir (2008), and employs as input variable isentropic PV at the 320 K level[1] on a $1° \times 1°$ global regular grid at 12-hour intervals. RW breaking is identified where a local reversal of the meridional PV gradient (manifesting as the overturning of PV contours; see e.g. McIntyre and Palmer 1985) is detected, as explained below.

For each output time, all PV contours are computed at 0.25 potential vorticity unit (PVU) intervals between 2 and 10 PVU (1 PVU = 10^{-6} $K\,m^2\,kg^{-1}\,s^{-1}$), ; a 21-point moving average is then applied to smooth all contours. Each contour is subsequently

[1]This level is the only one available for download from the ECMWF Meteorological Archival and Retrieval System archive for ensemble forecast data. Despite this limitation, PV at 320 K well represents upper-tropospheric dynamics and this level is sufficiently close to the 300 hPa isobaric level to be suitable for the scope of this thesis.

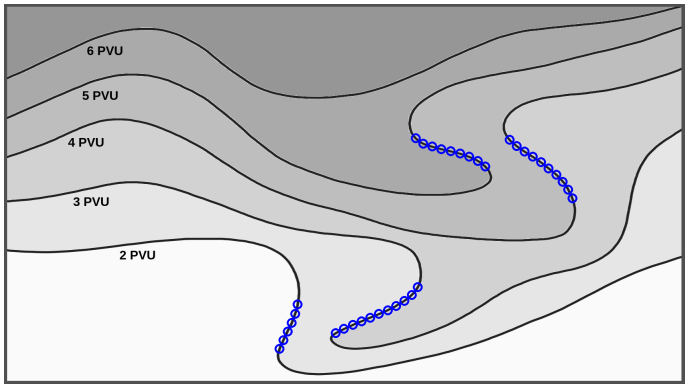

Figure 4.3: *Schematic of the identification of RW breaking regions using PV contours. RW breaking is detected where the meridional gradient of PV is reversed, as indicated by overturning contour segments, which are shown as sequences of blue dots.*

examined as follows: all points $\langle \lambda_i, \varphi_i \rangle$ (λ being longitude, φ latitude and $i = 1, \ldots N$, where N is the total number of contour points) are ordered from west to east; all contour segments $[\langle \lambda_i, \varphi_i \rangle, i_\mathrm{A} \leq i \leq i_\mathrm{B}]$ satisfying for each i the condition $\lambda_{i+1} < \lambda_i < \lambda_{i-1}$, thereby exhibiting a local reversal of meridional PV gradient, are considered to belong to a RW breaking region, as shown in Figure 4.3. Segments that are shorter than 500 km are discarded to reduce noise.

A matrix defined for all grid points and initially filled with zeros is used for the next step, when all RW breaking segments from all PV contours are examined: for each RW breaking segment point, the closest grid point is considered to be a RW breaking grid point and is thus assigned the value 1 in the matrix; once a grid point has been categorized as RW breaking, it maintains its status. RW breaking objects are eventually identified as contiguous regions of RW breaking grid points, as shown in Figure 4.4, and their position is computed at each time output as their "center of mass", similarly to RW packets (but without weighting). RW breaking objects smaller than 50 000 km^2 are discarded.

Before restricting the selection of PV contours to the 2–10 PVU range at 0.25 PVU intervals, the RW breaking object identification method was tested by 1) choosing a smaller or larger range, and 2) running the algorithm iteratively, starting with an initial interval of 2 PVU and reducing it by 50% at each iteration. It was found that 1) results show little sensitivity to the range when an upper bound of at least 10 PVU is used, and 2) with an increasingly smaller interval, each RW breaking object expands significantly at first, then only marginally; the 0.25 PVU interval was deemed optimal in the majority of cases, as most RW breaking objects expand by less than 1% when the interval is reduced by a further 50%. The RW breaking identification method was eventually used with a fixed interval to reduce computational costs.

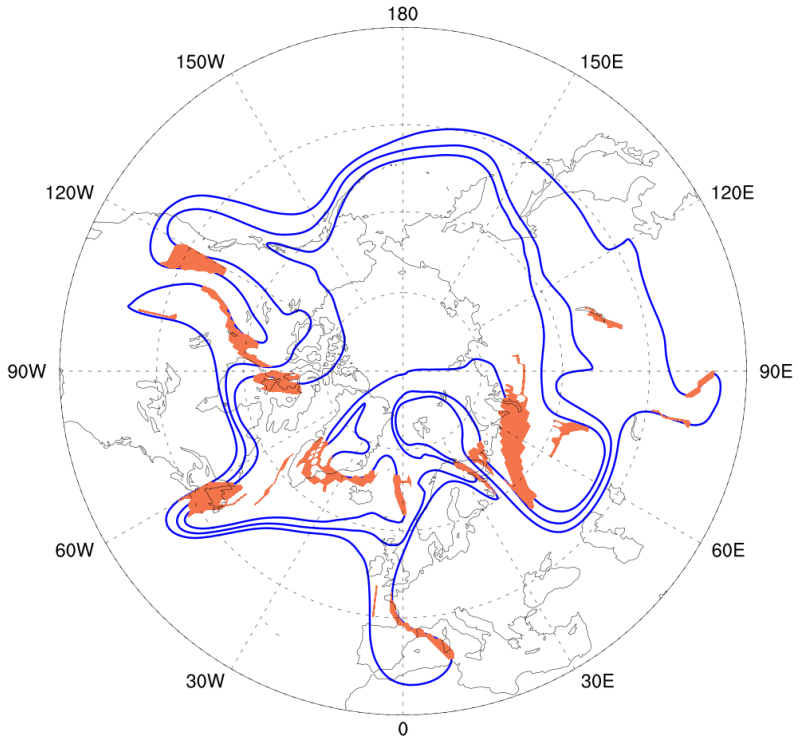

Figure 4.4: *Example plot of RW breaking objects and the quantities used for their identification: isentropic (320 K) PV contours are shown as blue contours for the 2, 4, 6 PVU values; RW breaking objects appear as dark orange shapes containing all grid points identified as RW breaking points (see text). Only circumpolar PV contours are shown for the sake of clarity.*

Similarly to RW packets, RW breaking objects are identified in both analysis and ensemble forecast data and characterized by the following properties, whose forecast statistics are discussed in Chapter 6: occurrence, position, area, distance between the object position and that of the Medicane, closest distance between the object and the cyclone (defined as the shortest distance between any object grid point and the cyclone), easternmost longitude, zonal extent, northernmost latitude, and meridional extent. For an output time to be considered as having RW breaking, a RW breaking object has to be found within 1500 km from the Medicane; RW breaking objects having a smaller area than 100 000 square kilometers are discarded.

4.3 Cyclone detection and tracking

Many available cyclone detection methods (Neu et al. 2013) are not suitable for Medicanes, as they have a much smaller radius compared to most types of cyclones (see e.g. Miglietta et al. 2011; Picornell et al. 2014). This issue is especially apparent when the input data have a relatively low horizontal resolution (Walsh et al. 2014),

which is the case for ECMWF ensemble forecast data. For this reason, an improved detection method was designed to identify pressure lows in both analysis and forecast data. This method has proven effective in detecting very small cyclones, while still being capable of detecting larger cyclones as well as filtering out spurious ones produced by noise or orographic effects.

The cyclone detection method used in this study is based on MSLP contours, spaced at 1 hPa intervals, and low-level vorticity, defined as relative vorticity averaged over the 1000, 925 and 850 hPa levels. Given the focus on the mature stage of cyclones, only closed contours are considered, thereby neglecting open systems (e.g. diminutive waves, see Hewson 2009). Pressure lows are identified as objects falling into at least one of two categories: (1) a set of four or more concentric contours; and (2) a set of two or more concentric contours with a radial MSLP gradient of 5 hPa/400 km or larger, calculated within a 400 km distance from the centre of the innermost contour, over at least 4 consecutive 30°-spaced azimuthal directions. The second category is necessary to include also earlier stages of a cyclone when its closed circulation is still developing but a small pressure low is already present at the boundary of a larger region of low pressure, with a large MSLP gradient in its vicinity.

Detected lows are discarded when at least one of the three following conditions is met: (1) the area of all MSLP contours exceeds 500 000 square km (low is too large); (2) the area of the second innermost contour is at least 50 times larger than the area of the innermost contour and the MSLP gradient is smaller than 5 hPa/400 km in all directions (low is considered noise); and (3) contours are too elongated and/or irregularly shaped (low is considered noise – this typically occurs in the vicinity of high orography). The centre of each pressure low is finally placed where low-level vorticity reaches a local maximum within a 100 km distance from the MSLP minimum. The values of thresholds and parameters have been chosen conservatively, so as to minimize the number of discarded lows. The outcome of cyclone detection shows little sensitivity to small variations of these thresholds and parameters.

After being detected, pressure lows are tracked in time using a method adapted from Hewson and Titley (2010), which uses 1000-500 hPa geopotential height (GPH) difference (thickness) and 500 hPa wind speed: while a short description is given here, the reader is referred to the article above for a detailed explanation. In this tracking scheme, a likelihood score (expressed in km) is computed for each possible pairing of a pressure low at the previous output time and one at the current output time (hereafter referred to as “past low” and “present low”, respectively). The score estimates the

likeliness of the pairing being correct: that is, how likely the present low is the result of the past low advancing to a new position.

In the present study, the likelihood score is built on two parameters: half-time separation and thickness change. Half-time separation is the distance between the past and the present low, after they are moved forward and backward in time, respectively, for 60% of the time interval, considering 500 hPa wind as the steering flow. Thickness change is the difference in 1000-500 hPa thickness between the positions of the past and the present low. A third parameter that was originally used in the likelihood score formula, namely feature type transition (Hewson and Titley 2010), is kept fixed to 60% (Hewson 2009, Table 2) when calculating the likelihood score, as the only type of feature considered in the present study is the closed low.

The smaller the likelihood score is, the more likely the pairing is correct – a low score results from a small half-time separation and a small thickness change. Pairings are discarded if the past and the present low are more than 600 km apart or if their likelihood score is higher than 700 km. After computing the likelihood score for all possible pairings, they get ranked from the lowest (most likely) to the highest (least likely). The ranking is finally read from top to bottom and each pairing is either accepted, if neither low was already previously paired, or rejected otherwise. When a pairing is accepted, the present low becomes the last element of the track that contains the past low. At the end, the remaining present lows form new tracks.

4.4 Evaluation parameters

In order to evaluate ensemble forecasts four parameters are used that are deemed to provide an adequate picture of each cyclone's intensity, kinematics and thermal structure: these are central pressure, symmetry, compactness and the upper-level thermal wind. The statistics of ensemble forecasts of these parameters will be examined in Chapter 6, together with those of storm position forecasts (see also explanation in Section 4.9).

Storm intensity is represented by the cyclone's central pressure (CP), i.e. its lowest MSLP. The intensity of Medicanes may be slightly underestimated by ECMWF operational analysis data due to insufficient horizontal resolution, an effect that is estimated to be around 2 hPa (see e.g. Cioni et al. 2016; Pytharoulis 2018). An even larger underestimation can be expected for ensemble forecasts, given their resolution (Picornell et al. 2014; Walsh et al. 2014), which is only half of that of the analysis data.

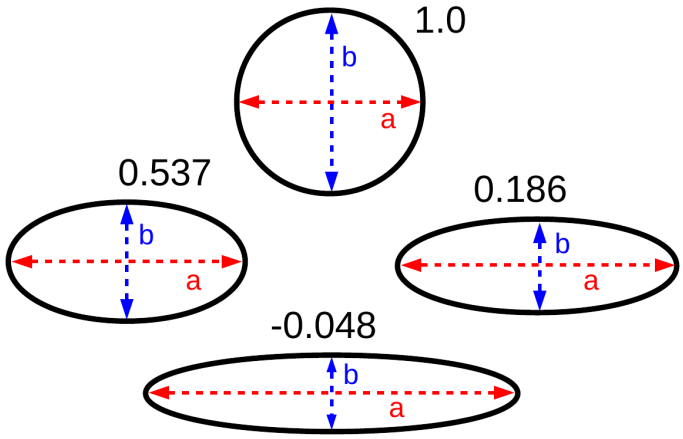

Figure 4.5: *The value attained by the S parameter is shown here for four ellipse-shaped contours, with semiaxes $a = 1$, $b = 1$ (top), $a = 2$, $b = 1$ (left), $a = 3$, $b = 1$ (right), and $a = 5$, $b = 1$ (bottom).*

In order to quantify the symmetry of the cyclone's low-level circulation, a symmetry parameter S is defined for any MSLP contour as follows: $S = 1+\arctan(\pi(4\pi A/P^2-1))$, where A is the area and P the perimeter of the contour. This seemingly complex formula is based on a straightforward expression of symmetry (A/P^2); this function is then scaled ($4\pi A/P^2$) such that maximum symmetry – a perfectly round contour – equals 1, and finally stretched by applying the arctangent, so as to more widely space high symmetry values, which would otherwise tend to bunch towards 1. The last step allows to better identify the highly symmetric, mature stage of the cyclone and interpret the ensemble statistics more clearly. An example of values attained by the S parameter for simple ellipse-shaped contours is shown in Figure 4.5. The symmetry parameter of any pressure low (hereafter referred to as just "symmetry", for the sake of brevity) is obtained by averaging S over the four innermost MSLP contours, spaced at 1 hPa intervals. During their mature, tropical-like phase, Medicanes attain high symmetry, with S values exceeding 0.8, as opposed to their early stages as well as the majority of extratropical cyclones which have much lower S values.

Medicanes also tend to be much smaller than extratropical cyclones, as already pointed out, with strong pressure gradients in the vicinity of their centres. In order to give a measure of such gradient, a "compactness" parameter (hereafter referred to as just "compactness") is defined as the azimuthally averaged radial MSLP gradient within a 150 km radius around the cyclone centre, expressed in hPa/100 km.

Finally, to quantify the cyclone's upper-level thermal structure – i.e. its cold or warm core – the three-dimensional CPS introduced by Hart (2003) is used, which is defined by 925-700 hPa storm-relative thickness asymmetry (B), lower-level (925-700 hPa) thermal wind ($-V_T^L$) and upper-level (700-400 hPa) thermal wind ($-V_T^U$). A positive (negative) sign of the $-V_T^U$ parameter indicates an upper-level warm (cold) core, while

the absolute value is proportional to its magnitude[2]. Given the lower height of the tropopause in the midlatitudes with respect to the tropics (Picornell et al. 2014) and the far smaller size of Medicanes compared to TCs (Miglietta et al. 2013), CPS parameters are calculated in a slightly different way from Hart (2003), using a smaller radius of 100 km (instead of 500 km) and lower levels of 925, 700 and 400 hPa (instead of 900, 600 and 300 hPa), similarly to Picornell et al. (2014). A 12-hour running mean is used in the present study to smooth CPS trajectories, differently from Hart (2003) who uses a 24-hour mean: this choice is motivated by the short life of most Medicanes and of their tropical-like phase in particular.

The calculation of CPS parameters can be very sensitive to the radius in case the cyclone has an extremely small size (see, for instance, the description of Medicane Qendresa in Chapter 5, Subsection 5.1.4). However, the evolution of these parameters in time tends to be very similar regardless of the radius used, with only the actual values depending on it, while the time series simply shift towards higher or lower values. Since the focus of this thesis is the predictability of Medicanes rather than a quantitative assessment of their dynamics, a fixed radius of 100 km has been deemed the best choice to produce consistent results between different cases. Nevertheless, the decision to include each Medicane event in the list of analyzed cases presented in Chapter 5 was subject to the requirement that the given Medicane attains an upper-level warm core, as computed using any CPS radius equal to or larger than 50 km, for at least two time outputs (corresponding to 12 hours), consistently with previous Medicane definitions (see e.g. Cavicchia et al. 2014a; Picornell et al. 2014).

4.5 Evaluation time window

Ensemble forecasts are evaluated against analysis data over a time window rather than at a single forecast time. This approach has the benefit of enhancing signals, in that the desired features – e.g. a storm intensity maximum – can be spotted over a larger set of forecast times (see also Section 4.9), thereby overlooking small timing errors (e.g. the maximum occurring a few hours earlier or later than forecast). The rationale for this approach is to focus on specific storm features and to consider a forecast to

[2]Lower-level thermal wind is not used in this analysis, as positive values of $-V_T^L$ characterize not only Medicanes, but also extratropical cyclones with a warm seclusion (Hart 2003). Thickness asymmetry B is also not used, as symmetry information is already contained in the symmetry parameter explained above. However, for the sake of completeness, both B and $-V_T^L$ are shown alongside $-V_T^U$ when describing the eight Medicane events in Chapter 5.

be sufficiently accurate if the features are successfully predicted, albeit at a slightly incorrect time. This strategy is especially valuable in extracting information from early forecasts, for which only few members may have a cyclone and even fewer may have it at the right place and time: in this case, tolerating small timing errors allows to extract more information from the forecast, as to e.g. whether a cyclone is predicted at all or whether it exhibits tropical-like traits.

The evaluation time window (ETW) is 24 hour long, corresponding to 5 points (i.e. 5 output times) of the cyclone track extracted from analysis data (hereafter "reference track"). Slightly shorter or longer ETWs were tested before settling on 24 hours, showing little sensitivity. The ETW is subjectively selected for each event to best represent the mature, tropical-like phase of the cyclone, on the basis of the symmetry, compactness and $-V_T^U$ parameters introduced in Section 4.4 (CP is not used as the mature stage of Medicanes often does not correspond to their most intense one).

An example of ETW selection is shown in Figure 4.6. As a first step, the 5 consecutive reference track points having the highest average $-V_T^U$ value are selected, given that $-V_T^U$ is considered the most relevant parameter in distinguishing TLCs from fully baroclinic cyclones (see e.g. Mazza et al. 2017). As a second step, the initial 5-point selection is shifted by at most 2 points, corresponding to maximum 12 hours earlier or later. This adjustment is only applied when necessary, to select output times with as high symmetry and compactness as possible: for storm Qendresa (Figure 4.6), for instance, the initial selection is shifted 1 point to the left (6 hours earlier) thereby increasing the average value of symmetry and compactness.

4.6 Track matching

The tracking procedure outlined in Section 4.3 is used for each storm to retrieve the reference track as well as tracks of MSLP lows in individual forecasts. The next step is to compare all tracks from a single member of the ensemble with the reference track in order to find the best match, i.e. the closest and most similar track, which is to be considered as the given member's cyclone. In order to avoid penalizing (small) discrepancies in the timing of storm motion and take into account the overall spatio-temporal similarity between tracks, a DTW technique (Berndt and Clifford 1994) is used, which has been successfully applied to a recent case study of North Atlantic TT (Maier-Gerber et al. 2019). Originally developed for speech recognition (Sakoe and Chiba 1978), DTW is able to match two time series nonlinearly, thereby taking into

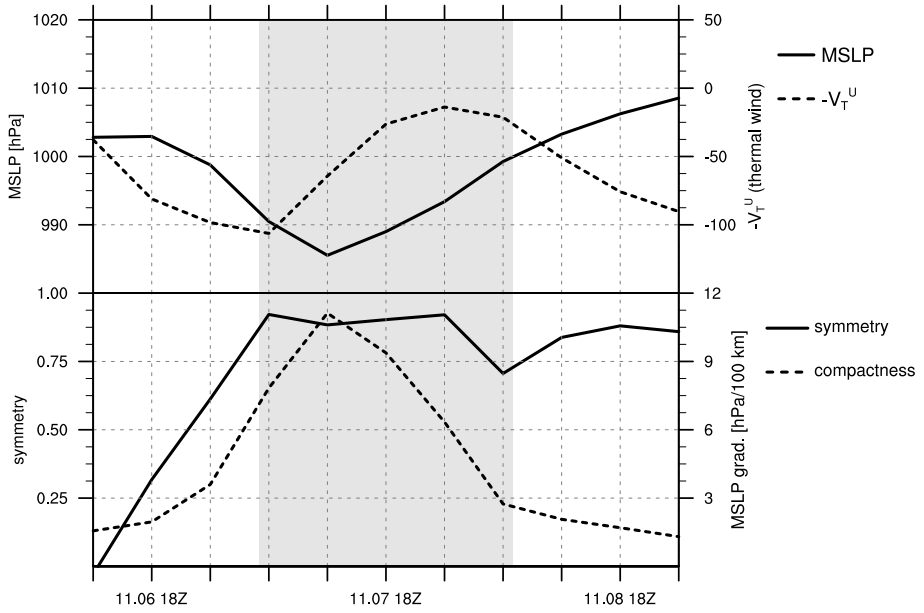

Figure 4.6: *Features of storm Qendresa (November 2014) as retrieved from analysis data. Upper panel: CP (hPa) and upper-level thermal wind $-V_T^U$; lower panel: symmetry and compactness. The ETW is highlighted in gray: in this case the selected period is from 0600 UTC on 7 November 2014 to 0600 UTC on 8 November 2014. Reprinted with permission from Di Muzio et al. (2019). © The Authors.*

account differences in signal speed and providing a more intuitive matching (Keogh and Ratanamahatana 2005). Using the DTW technique to match cyclone tracks allows to focus on the spatial accuracy of forecasts, ignoring small (local) timing errors as long as the forecast track bears a high spatial similarity to the reference one. The average time difference between DTW-paired track points may be later used to assess whether there is an early or late bias. In the following, the structure of the DTW technique is briefly described, to illustrate how it is applied to matching cyclone tracks. The reader is referred to Berndt and Clifford (1994) and Keogh and Ratanamahatana (2005) for more detailed explanations of the algorithm.

DTW requires first a suitable metric to express the spatial distance between each pair of track points: great circle distance has been chosen in this case, though any distance metric could be used in principle. The aim is then to minimize the overall distance between the two input tracks $R = r_1, r_2, \dots r_m$ and $S = s_1, s_2, \dots s_n$ by finding the best possible way of matching them. In order to do so, a $m \times n$ distance matrix D is first computed: $D(i,j) = d(r_i, s_j)$ for each $i = 1, \dots m$ and $j = 1, \dots n$, where $d(r_i, s_j)$ is the spatial distance between the r_i and s_j track points. A cumulative distance matrix M is then defined recursively as follows: $M(i,j) = D(i,j) + \min[D(i-1,j), D(i-1,j-1), D(i,j-1)]$. The optimal match is finally obtained as the *warping path*, defined as

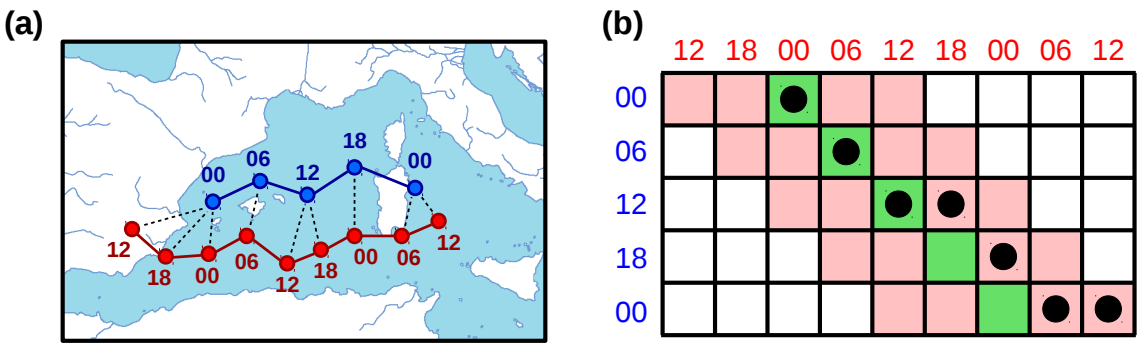

Figure 4.7: *Example of DTW matching of the reference track (blue) and a forecast track (red). Numbers denote UTC times. a) Spatial match; matched track points are highlighted by a black dashed line. b) Cumulative distance matrix M and warping path, represented as black filled circles, for the track match in a). The warping window is highlighted in red while the equal-time match is highlighted in green. Reprinted with permission from Di Muzio et al. (2019). © The Authors.*

the succession of M elements minimizing the cumulative distance at every point. Each element of the warping path represents a pair of matched track points, as shown in the fictitious example in Figure 4.7. It is worth noting that the two tracks have different lengths and that multiple points of one track are matched to a single point of the other.

A DTW technique is usually applied with some constraints, which introduce physically meaningful requirements (Berndt and Clifford 1994). Monotonicity and continuity constraints are first imposed to assure that all track points are matched at least once and with increasing time. A warping window (highlighted in red in Figure 4.7) only allows the warping path to exist in the vicinity of the diagonal of the M matrix (i.e. the succession of equal-time elements), thereby restricting the time difference between any pair of matched track points to a maximum absolute value of 12 hours. Using a warping window ensures a physically meaningful track match, preventing the match of two points that are spatially close but very distant in time. Finally, boundary conditions require the warping path to start from (end at) the forecast track point that is closest to the first (last) analysis track point, to prevent the algorithm from matching too many far away forecast track points to the first or last analysis point, which it would be forced to do if the forecast cyclone moves fast (an example is seen in Figure 4.7, where the first two forecast track points are not matched to the first analysis track point). These conditions ensure that similarity is maximized in the matching process.

DTW is applied to match the reference track's 24-hour ETW to each track in an ensemble member. Only forecast tracks that are at least 24 hours long (5 output times) are considered. Furthermore, a 48-hour interval is selected from each track, spanning the ETW plus further 12 hours (2 output times) at both ends, to meet the warping

window constraint. If the forecast track only exists for a fraction of these 48 hours, only the existing part is considered (the example in Figure 4.7 shows the longest possible forecast track, at 48 hours or 9 output times). The spatio-temporal distance between (the selected interval of) the forecast and reference tracks is finally computed in two steps: the average distance between a single reference track point and all associated forecast track points is first computed; the final track distance is then obtained by averaging the result of the above calculation over all reference track points.

For a given ensemble member, forecast tracks having a 600 km or larger spatio-temporal distance from the reference track are discarded. If no tracks are left, the member is considered to have no cyclone; such members are named "no-storm members" hereafter. Otherwise, the track with the shortest spatio-temporal distance is considered to be the best match, i.e. the most similar to the reference track. Members having a best match are named "storm members" hereafter. The DTW technique has ultimately a twofold purpose: it yields the exact point-by-point matching between any forecast track and the reference track, and thereby it assists in finding the best match among all tracks in a given member.

The 600 km threshold has been chosen after testing the sensitivity of the results to its value, similarly to Maier-Gerber et al. (2019), as represented in Figure 4.8: here the number of storm members, averaged over all eight cases for each lead time, is shown for all threshold values between 100 and 1000 km, at 100 km intervals. Short-term forecasts are sufficiently accurate and consequently exhibit a strong saturation, reaching the highest number of storm members already at a 200 km threshold; on the other hand, long-term forecasts have a much higher uncertainty and therefore a lower number of storm members overall, while exhibiting a slower, smoother saturation. The 600 km value has been chosen as it is found at the lower end of the saturation regime at most lead times. This value is also sensible in that it is comparable to the spatial scale of most Mediterranean sub-basins and hence the maximum distance a cyclone can travel uninterruptedly over water in the Mediterranean region.

4.7 Empirical Orthogonal Function analysis

Principal Component Analysis is one of the most widely used multivariate statistical techniques, first gaining the attention of the atmospheric science community following the work of Lorenz (1956), who called the technique Empirical Orthogonal Function (EOF) analysis. Both names are used today and essentially refer to the same technique.

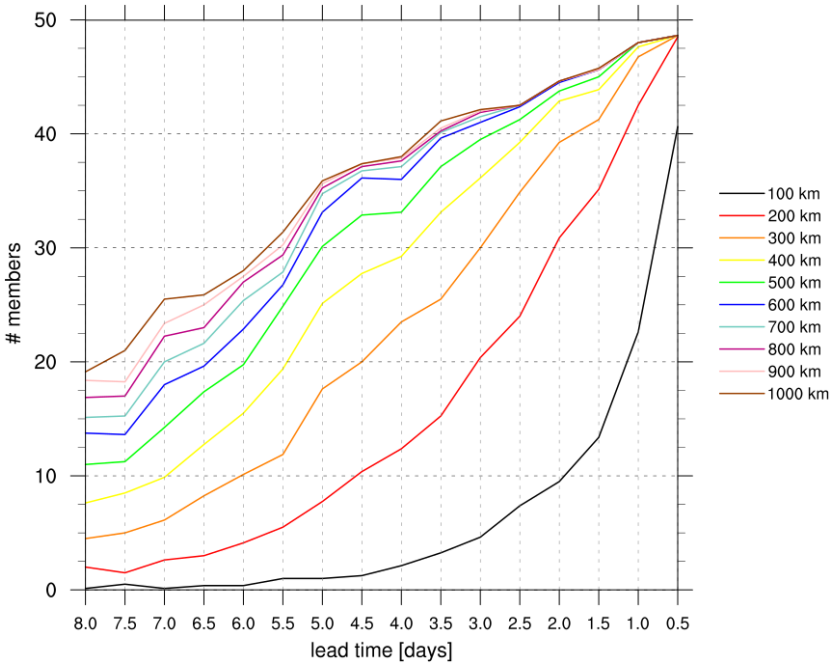

Figure 4.8: *Number of storm members, averaged over all eight cases for each lead time, for 10 values of the distance threshold between 100 and 100 km.*

While the basic structure and principles of EOF analysis are outlined here, the reader is referred to Wilks (2011) for a detailed description of this technique.

The goal of EOF analysis is to reduce a large data set containing many variables to a smaller one containing fewer new variables. The new variables are obtained as linear combinations of the old ones, which are computed so as to represent the maximum possible fraction of the variability of the original data. This approach works best when there is significant correlation among the old variables, i.e. when the original data contain redundant information, which is often the case for atmospheric data variables. EOF analysis thus filters out redundant information, being an effective method for 1) data compression and 2) data exploration, whereby the analysis of the spatio-temporal variability of the original data enables new interpretations of the physical processes hidden therein.

The starting point of EOF analysis is an $N \times 1$ data vector $\boldsymbol{x}$ representing a single "measurement" (e.g. for $N = 2$, temperature and pressure measured by a weather station or output by a model at a given location, at a given time). From a time series of K measurements $\boldsymbol{x}_t$, where $t = 1, \ldots K$ one can calculate the anomalies: $\boldsymbol{x}'_t = \boldsymbol{x}_t - \bar{\boldsymbol{x}}$. EOF analysis yields a new vector $\boldsymbol{u}$, whose components u_m are called the Principal Components (PCs):

$$u_m = \boldsymbol{e}_m^T \boldsymbol{x}' = \sum_{n=1}^{N} e_{nm} x'_n, \quad m = 1, \ldots M \tag{4.5}$$

The first PC, u_1, is the linear combination of $\boldsymbol{x}'$ having the largest variance. The subsequent principal components u_m, $m = 2, 3\ldots$ are the linear combinations having the largest possible variances, subject to the condition that they are uncorrelated with the PCs having a lower m. The result is that all the PCs are mutually uncorrelated. In order to obtain the PCs, there is a unique choice for the $\boldsymbol{e}_m$ vectors, which must be the eigenvectors of the covariance matrix of $\boldsymbol{x}$, $\boldsymbol{S}$. The m^{th} PC is then interpreted as the projection of the anomaly vector $\boldsymbol{x}'$ onto the m^{th} eigenvector. The eigenvectors are generally referred to as EOFs.

The variance of the m^{th} PC is the total variability of the data vectors $\boldsymbol{x}_t$ along the direction of the m^{th} eigenvector and is expressed by the m^{th} eigenvalue λ_m. The first eigenvector $\boldsymbol{e}_1$ is associated with the largest eigenvalue λ_1 and oriented along the direction in which the data vectors exhibit the largest variability. The second eigenvector $\boldsymbol{e}_2$ is associated with the second-largest eigenvalue λ_2 and oriented along the direction perpendicular to that of $\boldsymbol{e}_1$ in which the data vectors exhibit the next largest variability, and so on. All together, the eigenvectors define a new vector space, corresponding to a new coordinate system in which each data vector can be expressed.

Equation 4.5 can also be written in the form

$$\boldsymbol{u} = \boldsymbol{E}^T \boldsymbol{x}' \tag{4.6}$$

Inverting now Equation 4.6, $\boldsymbol{x}'$ can be expressed as

$$\boldsymbol{x}' = \boldsymbol{E}\boldsymbol{u} \tag{4.7}$$

In principle, E is an $N \times N$ matrix. This means that Equation 4.7 is an exact form of the $\boldsymbol{x}'$ vectors. In practice, one usually keeps an arbitrary number of eigenvectors M, representing a large fraction of the total variability, and discards the remaining ones. This way, E becomes an $M \times N$ matrix composed by the first $\boldsymbol{e}_m$, $m = 1, \ldots M$ eigenvectors.

When $N = 2$, EOF analysis can be easily interpreted, as it yields a rotated two-dimensional space in which the first axis (defined by the first eigenvector) corresponds to the direction of maximum variability of the data, and the second axis is simply oriented along the perpendicular direction. An example of this will be discussed in Section 4.9, where the application of EOF analysis to the uncertainty of cyclone position is illustrated.

EOF analysis is typically applied to time series, that is to series of data vectors $\boldsymbol{x}_t$, $t = 1, \ldots K$ each representing a quantity at a different time. In this thesis, however, this technique will be applied to the "ensemble member" dimension of ensemble forecasts, with each data vector representing a different member, with the aim of investigating variability in space and among ensemble members.

4.8 Statistical significance

In Section 6.2, a compositing approach is employed to analyze the influence of large-scale precursor processes on the occurrence and thermal structure of the predicted cyclones. Two types of composites are computed, concerning respectively the occurrence of a cyclone *per se* and that of a warm-core cyclone as opposed to a cold-core one. For the first type, the average 300 hPa GPH of the no-storm members is subtracted from that of the storm members; the difference is then normalized by dividing by the ensemble standard deviation (this allows a straightforward comparison of different composites in space, time and lead time, see e.g. Torn et al. 2015). For the second type of composites, the average 300 hPa GPH of the lowest tercile of storm members (having ordered them according to their $-V_T^U$ value, i.e. the warm core magnitude) is subtracted from that of the highest tercile of storm members; the difference is then normalized by dividing by the ensemble standard deviation (considering only the storm members). In addition to Earth-relative, Eulerian composites, cyclone-relative, Lagrangian composites are also computed for the thermal-structure type of composites: in such case, only the region within 750 km from the cyclone center is considered.

Statistical significance of composite differences is assessed via a bootstrap method (Wilks 2011) with $n = 10\,000$ random draws. The two-sided significance level of 5% is used to test whether the composite difference is significantly different from zero at each grid point. The same resampling is used for all grid points and forecast times for a given forecast, to minimize potential misinterpretations and maximize spatial and temporal correlation (Wilks 2016). The bootstrap method used allows for comparison between different sample sizes, which is useful when calculating composites of two unequally large subsets of ensemble members.

The same bootstrap method is used to test the statistical significance of the linkage between the forecast distribution of RW-related variables and that of cyclone occurrence (storm vs no-storm members) or $-V_T^U$ (warm-core vs cold-core members). The procedure is as follows. All ensemble members are first sorted into two subsets, those

having the RW object and those without it. The bootstrap method is then applied to the difference between the two subsets in 1) the number of no-storm members and 2) the average $-V_T^U$ value; the same resampling is used for the two applications. For each RW variable (e.g. area, position etc.), the bootstrap method is also applied to its ensemble distribution, i.e. considering only members having the RW object; for the sake of clarity, RW packet area will be used here as an example. In this case, the statistic to test is either the average or the standard deviation of the distribution of 1) no-storm members and 2) high-$-V_T^U$ members (warmer-core members, i.e. the upper $-V_T^U$ tercile). For the average, the two-sided significance level of 5% is used, as no-storm/high-$-V_T^U$ members might have a significantly high or low average RW packet area; for the standard deviation, the one-sided significance level is used, as the only interesting case is when no-storm/high-$-V_T^U$ members are concentrated around a certain value of RW packet area.

4.9 Evaluation of ensemble forecasts

The ensemble forecasts of the eight storms are evaluated in Chapter 6 from a fixed-event perspective (Pappenberger et al. 2011), that is by examining multiple consecutive forecasts while focusing on a fixed period of forecast time (the ETW in this case). Given that forecasts are evaluated over a time window rather than at a fixed forecast time, lead times refer to the central time of the ETW. For each storm, the latest forecast considered is the one initialized either at the beginning of the ETW, if it begins at 0000 or 1200 UTC, or 6 hours earlier, if the ETW begins at 0600 or 1800 UTC. For the sake of simplicity, the latest forecast is always labeled as "0.5 day" (see Chapter 6) despite being actually an 18-hour forecast in cases where the ETW begins at 0600/1800 UTC (this small 6-hour difference between cases does not affect the results). A total 16 forecasts are examined for each case, the earliest being an 8-day forecast.

Instead of using standard box-and-whisker plots, box-percentile plots (Esty and Banfield 2003) have been preferred when displaying ensemble forecast statistics (see Figures 6.2 and 6.5, for instance) in that they display the whole distribution of input data: the width of each irregular "box" is proportional to the percentile p of the ordinate if $p \leq 50$, or to $100-p$ if $p > 50$; the maximum width is thus reached at the median, while outliers are revealed by thin spikes at each tail.

In order to further enhance signals and relax the requirement of an exact match between forecasts and the analysis, the extreme value of each parameter (the lowest

value for CP, the highest value for symmetry, compactness and $-V_T^U$) is considered when evaluating forecasts. The extreme value of a given parameter is computed for each storm member within the DTW-matched interval of its track (the best match found by applying DTW as described in Section 4.6) and compared with the extreme value computed within the reference track's ETW.

Cyclone position forecast statistics, shown in Figure 6.4, are investigated by means of EOF analysis (see Section 4.7). For each storm member, a 2D cyclone position error is expressed as the average longitude and latitude difference between the reference track and the forecast track, computed using the DTW-matched points in an analogous manner as the spatio-temporal distance. EOF analysis is then performed on all 2D error values for each forecast (one value for each storm member). The eigenvectors of their covariance matrix define a rotated coordinate system where variability is maximized along the x-axis, as already mentioned in Section 4.7. The spread of cyclone position errors is proportional to their variance in this coordinate system and is represented as an ellipse whose axes are aligned to the ones of the rotated system and have lengths proportional to the variance along each eigenvector. Such ellipse is essentially a bivariate normal distribution fit to the position errors, and can be arbitrarily scaled with respect to the variance so as to encircle a chosen fraction of error points. This compact representation, shown for one example forecast in Figure 4.9, has the benefit of providing an immediate visual grasp of the extent and spatial distribution of cyclone position errors. Furthermore, this method is not limited to latitude and longitude, but can be applied in principle to any pair of parameters, allowing an analysis of their joint variability.

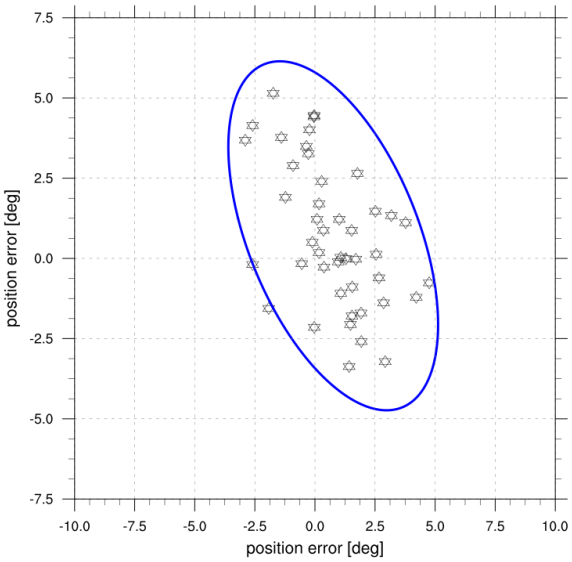

Figure 4.9: *Compact representation of cyclone position errors using EOF analysis. Each star represents cyclone position error in one storm member. The ellipse has the major axis oriented along the direction of maximum variability of the error values (i.e. the direction of the first EOF) and is scaled so as to encircle 95% of error points. In this case, about 77% of the total variability is associated with the first EOF, while the remaining 23% is associated with the second EOF. This forecast, pertaining to cyclone Qendresa (Section 5), was initialized at 1200 UTC on November 1, 2014.*

Chapter 5

Case characterization

The evolution of the eight cyclones analyzed in this study is illustrated in this chapter, from the large-scale processes leading to their formation to cyclone development, intensification and final dissipation. In Section 5.1, each event is described in detail in a separate subsection. In each of these subsections, focus is first given to the large-scale precursors of the cyclone: 1) a RW packet forming far upstream of the Mediterranean, typically over the North American continent or the western Atlantic, and subsequently travelling eastward towards Europe; 2) RW breaking occurring over the eastern Atlantic or western Europe at the end of the lifetime of the RW packet; and 3) an upper-level trough penetrating into the Mediterranean as the RW breaks. The attention then shifts to the cyclone, describing its evolution and salient features and quantifying its kinematic and thermal structure using ECMWF analysis data.

The trajectories, intensity and upper-level thermal-wind values of all events are displayed in Figure 5.1. A summary of the main characteristics of the eight storms, as derived from analysis data, is then given in Table 5.1, where cyclone duration, period and region of occurrence are provided along with maximum intensity (i.e. minimum CP), symmetry, compactness, 10 m wind speed and upper-level thermal wind $-V_T^U$. Storm names were chosen by the Institute of Meteorology at the Free University of Berlin in all cases but for Trixie (Subsection 5.1.7; also known as "Trixi", depending on the source), which was nicknamed by the media.

The geographical distribution of the eight storms is consistent with the findings of Miglietta et al. (2013), Cavicchia et al. (2014a) and Nastos et al. (2018), with seven out of eight storms forming or spending a significant part of their lifetime in two known Medicane "hotspots": the western Mediterranean and the Ionian Sea. Storm Stephanie is technically not a Medicane, having occurred outside of the Mediterranean

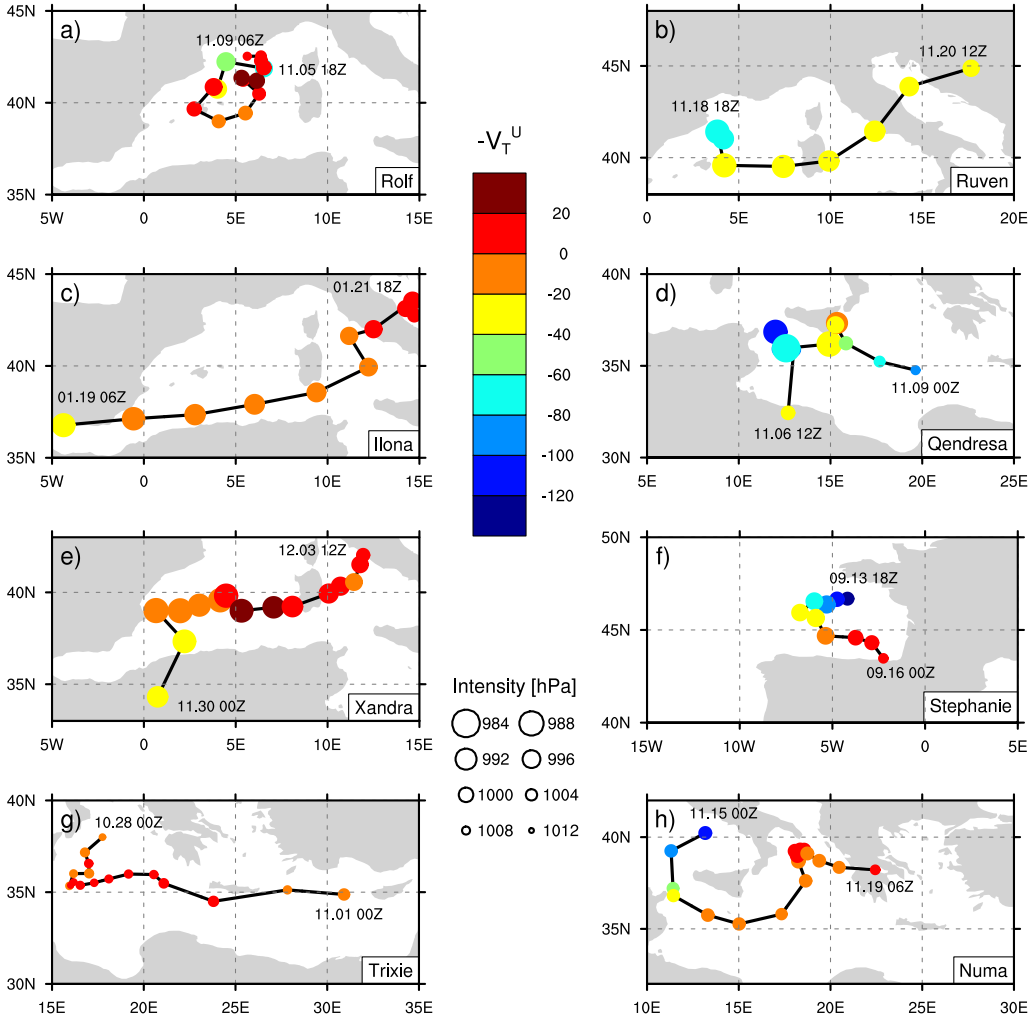

Figure 5.1: *Tracks of the eight storms. The colour of each circle represents the $-V_T^U$ value, while its size represents the CP value. Reprinted with permission from Di Muzio et al. (2019). © The Authors.*

Sea, but was included in this list because of its structural similarity and geographical proximity to other Medicanes. The seasonal distribution of the eight storms is instead slightly different from both the one in Cavicchia et al. (2014a) and the one in Nastos et al. (2018), as five of the eight storms occurred in November. However, the period considered in this thesis is too short to attribute any statistical significance to this different seasonality.

The data in Table 5.1 and the cyclone tracks in Figure 5.1 illustrate the high heterogeneity of the eight events in terms of their duration (Ruven developed rapidly and only lasted 48 hours, Numa remained almost stationary over the Ionian Sea for 36 hours and lasted 120 hours), intensity (almost 20 hPa difference between the most intense, Qendresa at 986 hPa, and the least intense, Trixie at 1005 hPa), compactness

Table 5.1: *Period and region of occurrence, duration, presence of an upper-level cut-off trough, SST anomaly [K], 10 m wind [ms^{-1}], CP [hPa], symmetry, compactness [hPa/100 km], upper-level thermal wind $-V_T^U$ for the eight storms, as inferred from operational analysis data. The lowest value reached during the lifetime of the cyclone is shown for CP, the average value for SST anomaly and the highest value for every other parameter; 10 m wind is computed within 250 km from the center of the storm. Adapted from Di Muzio et al. (2019). © The Authors. Used with permission.*

Storm	Period	Region	Dur.	UCT	SSTA	W10	CP	Symm.	Comp.	$-V_T^U$
Rolf	Nov 2011	WM	96 h	yes	1.6	22	997	0.95	6.6	26
Ruven	Nov 2013	WM, TS, AS	48 h	prior	0.9	22	990	0.85	3.8	-31
Ilona	Jan 2014	WM, TS, AS	60 h	no	0.6	23	991	0.83	3.2	8
Qendresa	Nov 2014	SM	60 h	yes	0.9	27	986	0.92	10.8	-14
Xandra	Nov/Dec 2014	WM, TS	84 h	early	1.6	19	989	0.95	3.6	22
Stephanie	Sep 2016	BB	54 h	yes	1.8	22	998	0.96	6.0	11
Trixie	Oct/Nov 2016	SM, EM	96 h	yes	1.7	24	1005	0.96	4.9	18
Numa	Nov 2017	TS, SM, IS	120 h	early	0.6	19	1002	0.98	5.1	20

Abbreviations: *dur. = duration; UCT = upper-level cut-off trough; SSTA = SST anomaly; W10 = 10 m wind; symm. = symmetry; comp. = compactness.*
Regions: *WM = Western Mediterranean; SM = Southern Mediterranean; EM = Eastern Mediterranean; TS = Tyrrhenian Sea; AS = Adriatic Sea; IS = Ionian Sea; BB = Bay of Biscay.*
UCT: *yes = is present throughout the mature stage of the cyclone and during at least 75% of its lifetime; no = is not present at all or only for less than 20% of the lifetime of the cyclone; early = is not present throughout the mature stage of the cyclone, but it is for all of its early stage; prior = is not present during the lifetime of the cyclone, but it is prior to its development.*

(Qendresa reached 10.8 hPa/100 km MSLP gradient, Ilona only 3.2 hPa/100 km) and thermal structure (most storms developed a moderate upper-level warm core, yet Ruven and Qendresa attained only an extremely small one, which does not show up using the same CPS radius as in the other cases).

5.1 Individual events

5.1.1 Rolf (November 2011)

With a lifetime of 96 hours and exhibiting a strong Medicane signature for at least 48 hours, cyclone Rolf is one of the longest-lived Medicanes on record and one of only two Medicanes on which National Oceanic and Atmospheric Administration (NOAA) released official information[1], recognizing it as a tropical storm and naming it M01. Rolf formed northeast of the Balearic Islands, off the southern coast of France, on November 5, 2011 and remained in the same region throughout its lifetime, slowly

[1] https://www.ssd.noaa.gov/PS/TROP/2011/bulletins/archive.html; the other Medicane on which NOAA issued a report is cyclone Trixie, which is presented in Subsection 5.1.7.

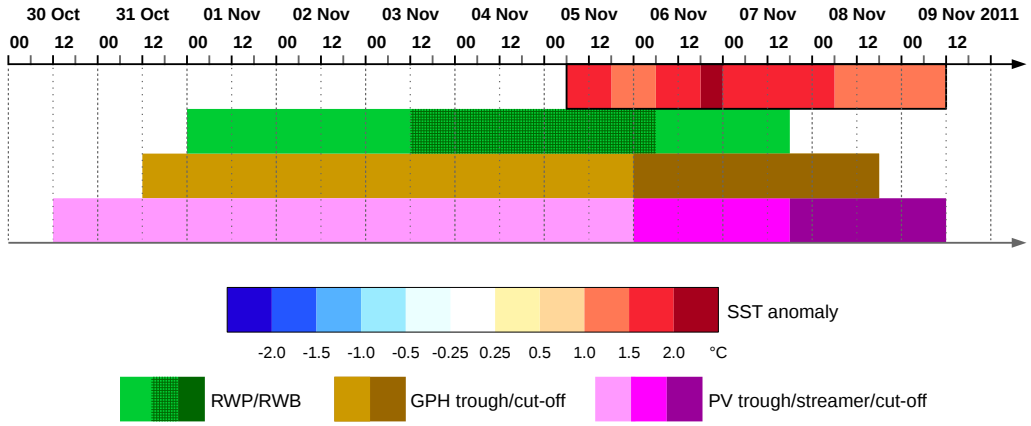

Figure 5.2: *Event calendar of cyclone Rolf as derived from analysis data. The cyclone occurrence time is represented as a black rectangle, containing SST anomaly averaged within 200 km from the cyclone center and shown in shading. Dynamical precursors are represented below as colored bars: a RW packet (light green), RW breaking (dark green), or both of them if they occur at the same time (dark green hatching on light green); a 300 hPa GPH trough (light brown) or cut-off trough (dark brown); a 320 K isentropic PV trough (pink), streamer (light purple) or cut-off trough (dark purple). At each time along the calendar and for each precursor structure, only the one that is associated with the storm is shown, provided it exists. The entire lifetime of all precursors is displayed, from the time they form to the time they dissipate, with the exception of RW breaking objects: GPH and PV troughs are tracked back in time visually, while RW packets are tracked using the technique mentioned in Subsection 4.2.1; RW breaking objects are also tracked back visually, but they only appear in the calendar as long as at least one object is found within 1500 km from the cyclone.*

moving in a loop and briefly making landfall on the Balearic Islands on November 6 (see map in Figure 5.1). Rolf produced intense wind gusts in excess of 40 ms^{-1}, torrential rainfall and floods[2].

A timeline of Rolf is shown in Figure 5.2, including its dynamical precursors. A small upper-level trough formed over the northeastern USA on October 30 and grew in size while crossing the Atlantic (see Figure 5.3). A RW packet formed over the North Pacific on November 1 and subsequently crossed the North American continent and the Atlantic Ocean. The RW broke over the eastern Atlantic while the trough penetrated into the western Mediterranean and later developed into a cut-off a few hours after Rolf's formation. An almost perfect vertical alignment was maintained between the upper-level and lower-level lows throughout the early and mature stages of the cyclone. Rolf encountered anomalously warm SST throughout its lifetime, which may have promoted the emergence of its tropical-like traits.

[2]See http://www.weathercast.co.uk/nc/weather-news/news/article/medicane_hits_the_western_med.html and https://www.thinkspain.com/news-spain/20339/roads-closed-by-flooding-in-mallorca-and-menorca.

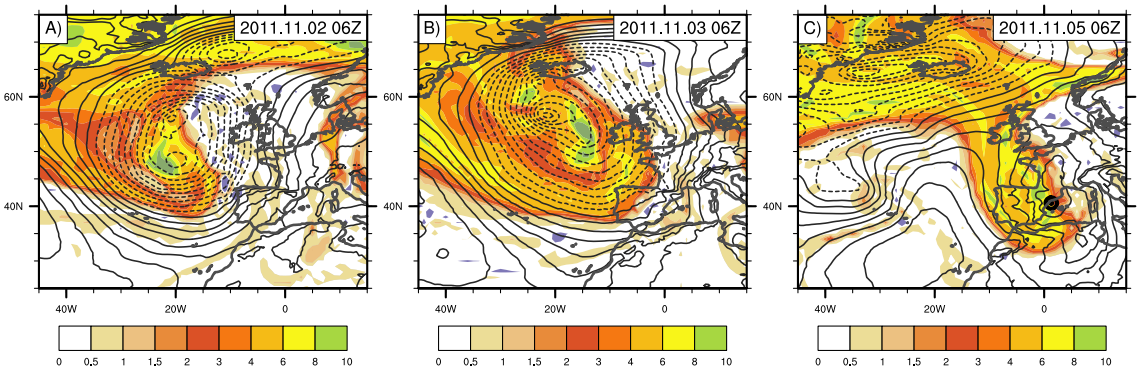

Figure 5.3: *Precursor trough of cyclone Rolf. Maps of 320 K isentropic PV (PVU, shading) and 1000 hPa GPH (dashed/solid contours for negative/positive values, interval 25 gpm), respectively 72 hours* (A) *and 48 hours* (B) *prior to the time of cyclone development* (C)*, where the black circle represents the position of the cyclone.*

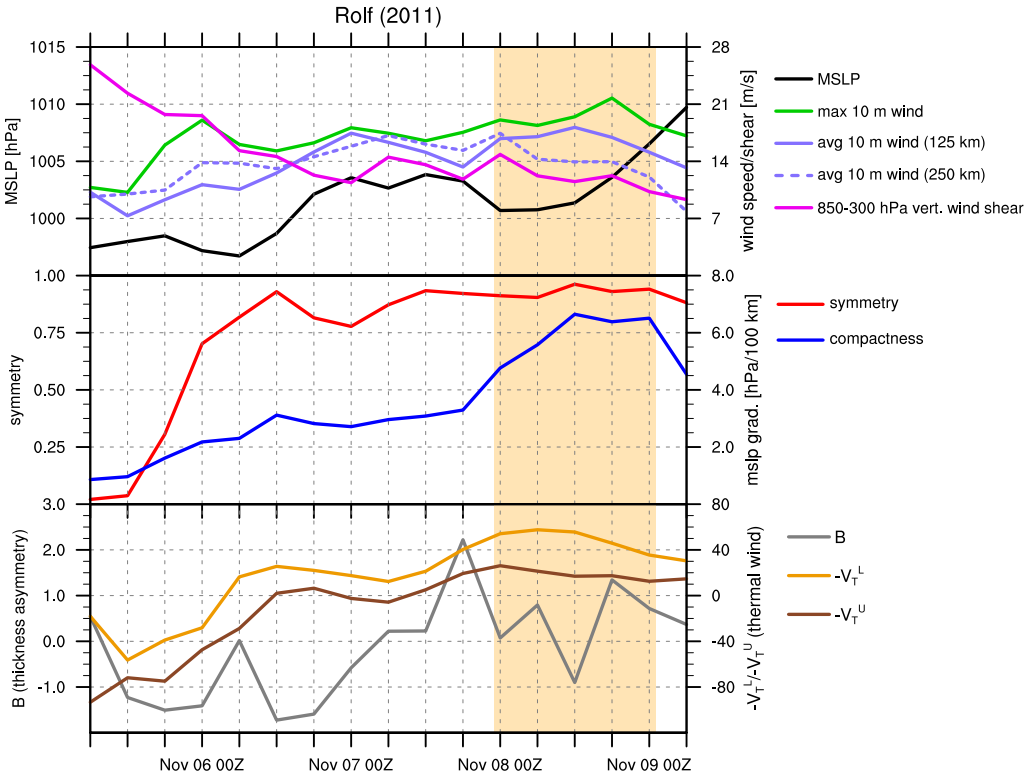

Figure 5.4: *Key features of cyclone Rolf.* (Upper plot) *CP (hPa, black line), maximum 10 m wind speed (ms^{-1}) within a 250 km distance (green line), average 10 m wind speed (ms^{-1}) within a 125 km (light blue solid line) and 250 km distance (light blue dashed line), and 850–300 hPa VWS (ms^{-1}) averaged within a 500 km distance (purple line); all distances are with respect to the center of the cyclone.* (Middle plot) *Symmetry (non-dimensional, red line) and compactness (hPa/100 km, blue line).* (Lower plot) *The CPS parameters: thickness asymmetry B (m, grey line), lower-level thermal wind $-V_T^L$ (m, dark yellow line) and upper-level thermal wind $-V_T^U$ (m, brown line). The ETW (see Section 4.5) is highlighted in light orange throughout all plots.*

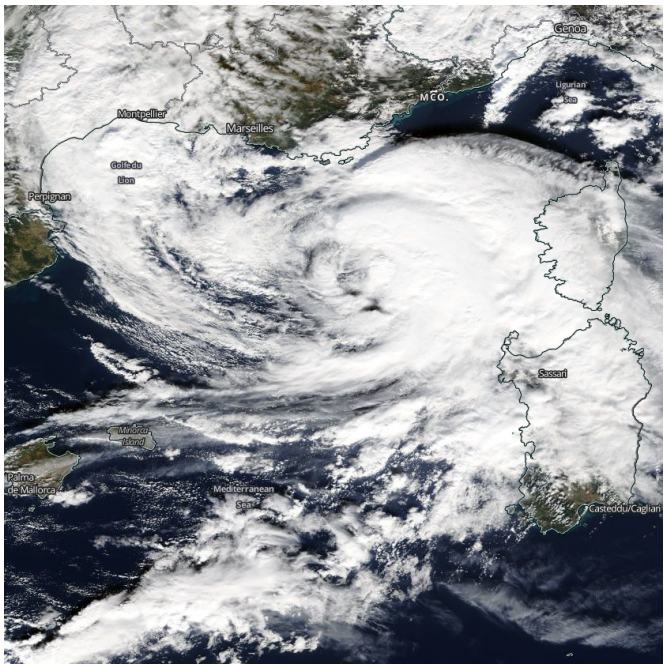

Figure 5.5: *False-color image of storm Rolf captured by NASA's MODIS Terra satellite at 1030 UTC on November 8, 2011. The picture was captured around the time the warm core magnitude peaked, during Rolf's late stage. The small scale of the cyclone is apparent at this time.*

The evolution of the kinematic and thermal structure of the cyclone is shown in Figure 5.4. Despite the fact that Rolf reached its lowest CP early on, the maximum 10 m wind speed exhibited a steady increase through most of its lifetime, reaching tropical storm intensity during the cyclone's mature stage, while VWS initially decreased and then remained stable throughout the cyclone's mature stage. The increase in wind speed was associated with 1) a contraction of Rolf's size, as indicated by the increase of compactness, which was initially slow but much faster in the cyclone's mature stage, and 2) a strong symmetrization already in the early stage. As the storm contracted and became more symmetrical, it also gradually developed a warm core, as seen from the steady increase of $-V_T^L$ and $-V_T^U$ which both peaked in the cyclone's late stage. Due to Rolf's small size, especially during its mature stage (see the satellite image in Figure 5.5), CP is overestimated in ECMWF analysis data: for instance, Miglietta et al. (2013) report a far lower MSLP (about 990 hPa) on November 8; wind speed is also likely underestimated.

5.1.2 Ruven (November 2013)

Storm Ruven developed on November 18, 2013 northeast of the Balearic Islands and underwent a very rapid evolution, crossing the western Mediterranean, the Tyrrhenian Sea and the Adriatic Sea and dissipating over the Balkan Peninsula after making landfall twice in Sardinia and in peninsular Italy (see map in Figure 5.1). Despite its short

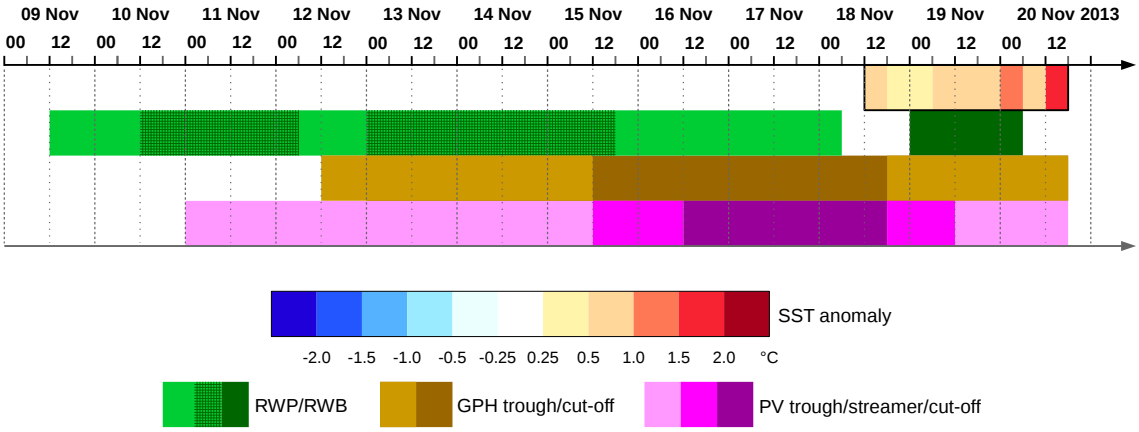

Figure 5.6: *Event calendar of cyclone Ruven, as in Figure 5.2.*

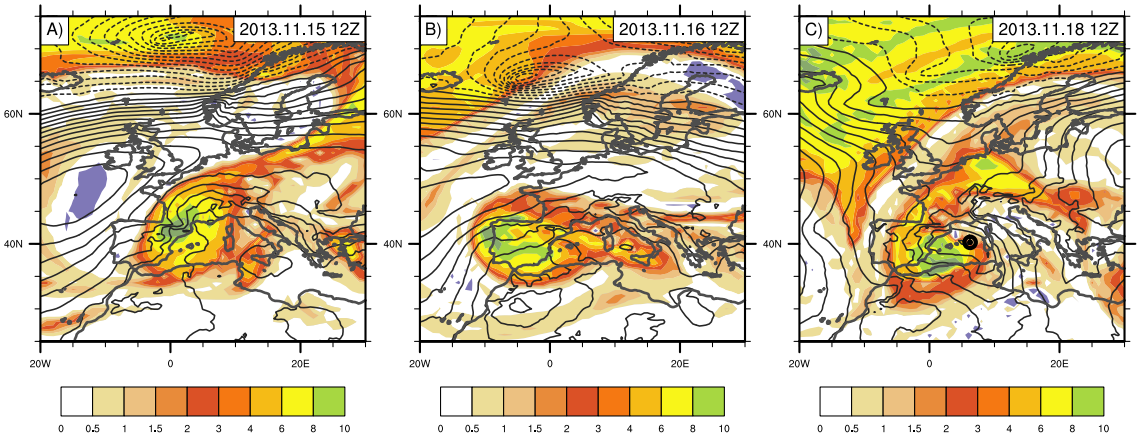

Figure 5.7: *Precursor trough of cyclone Ruven; as in Figure 5.3.*

lifetime of 48 hours, Ruven caused widespread damage and destruction in Sardinia, as well as eighteen casualties[3], mostly due to intense floods associated with torrential rainfall, which peaked at over 400 mm.

The large-scale dynamical precursors of Ruven are shown schematically in Figure 5.6. A RW packet formed on November 9 over the Atlantic and underwent RW breaking over western Europe two days afterwards; this RW packet was associated with a deep upper-level trough which developed into a cut-off over the Central Mediterranean and remained there for 2 days, promoting cyclogenesis and helping to create a conditionally unstable environment in the region. Meanwhile, another RW packet had formed on November 9 over the North Pacific, subsequently crossing the North American continent and the Atlantic and eventually breaking over Northwestern Europe on November 15. This RW packet was associated with a persistent ridge over the eastern Atlantic

[3]See for instance https://en.wikipedia.org/wiki/2013_Sardinia_floods and https://www.bbc.co.uk/news/world-europe-24996292.

and a trough downstream (see Figure 5.7), which penetrated into the Mediterranean region on November 15 and quickly developed into a cut-off, remaining over Spain and the western Mediterranean for 3 days. Ruven formed, as most Medicanes, under this cut-off trough. However, shortly after the cyclone formed, the trough rapidly weakened, broadened and moved eastward, causing Ruven to undergo a more rapid evolution than other Medicanes, as it was rapidly steered through the western Mediterranean and across Italy and dissipated over the Balkan Peninsula a day later.

The evolution of the cyclone's kinematic and thermal structure, shown in Figure 5.8, suggests that Ruven may be considered a "failed Medicane", as its intensification, contraction and warm-core development were likely hindered, if not interrupted, by a variety of factors such as 1) its landfall in Sardinia and afterwards in Italy, 2) weak positive SST anomalies (see Figure 5.6) and 3) an insufficient reduction in VWS as the upper-level cut-off dissipated. Nevertheless, Ruven exhibited typical Medicane features to some extent, including 1) intense winds reaching tropical storm intensity in its early stage, 2) an eye-like feature at its center, visible in the satellite image in Figure 5.9, 3) an initial tendency to contract and become more symmetrical, reaching relatively high values of symmetry and compactness (Figure 5.8), and 4) a lower-level warm

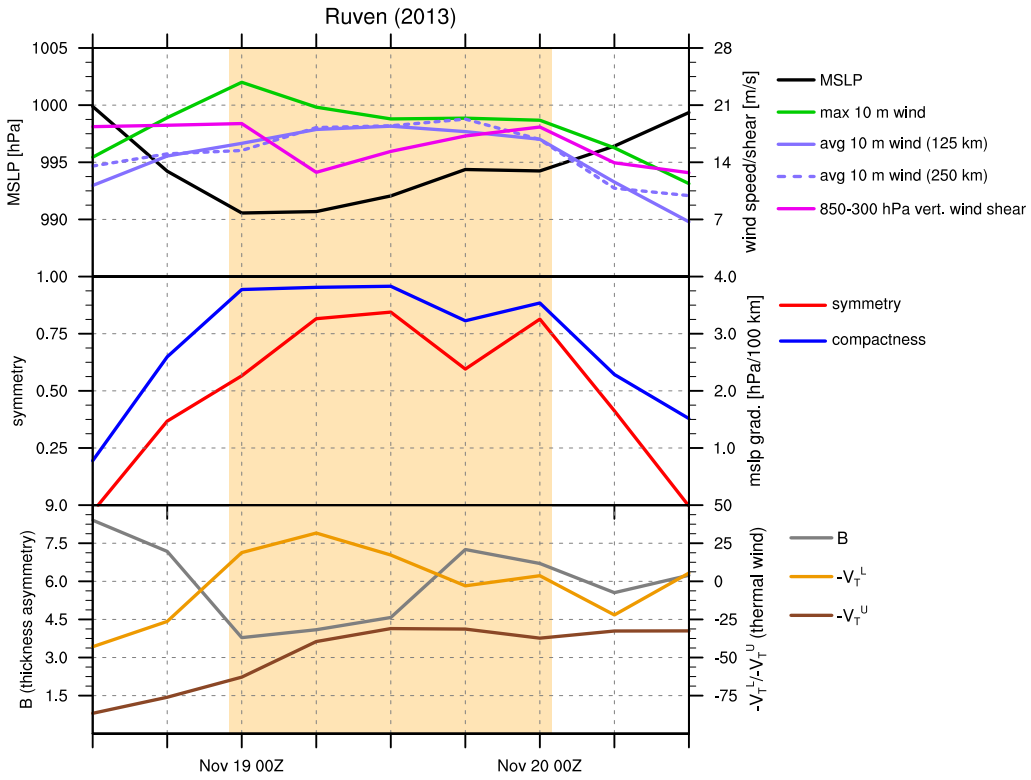

Figure 5.8: *Key features of cyclone Ruven, as in Figure 5.4.*

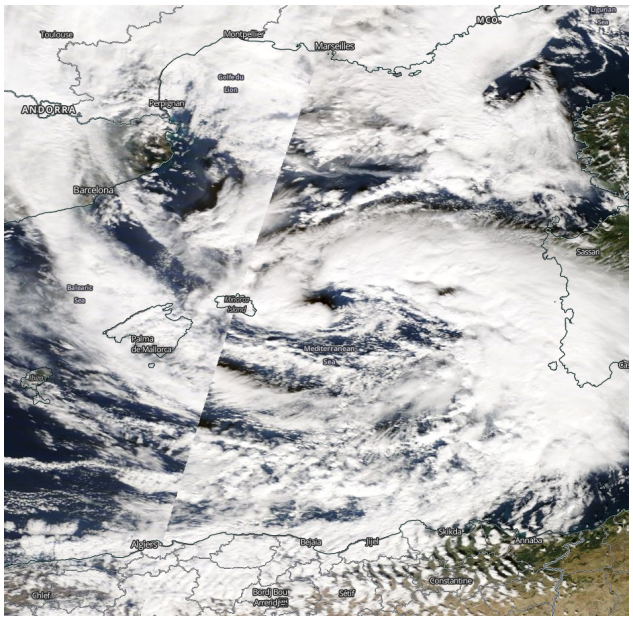

Figure 5.9: *False-color composite image of storm Ruven captured by NASA's MODIS Terra satellite at 0955 UTC (right part) and at 1130 UTC (left part) on November 19, 2013.*

core. On the other hand, Ruven never attained an upper-level warm core, although the value of $-V_T^U$ is sensitive to the chosen calculation radius in this case: if a much smaller radius of about 50 km is chosen instead of the 100 km radius used (Section 4.4), $-V_T^U$ exceeds the 0 threshold for a short time, indicating that the storm indeed developed a tiny, weak, short-lived upper-level warm core during its mature stage.

5.1.3 Ilona (January 2014)

Storm Ilona developed on January 19, 2014 near Gibraltar and quickly crossed the western Mediterranean, the Tyrrhenian Sea and the Italian Peninsula, eventually weakening over the Adriatic Sea 60 hours later (Figure 5.1). The cyclone's evolution was markedly perturbed by the orography of Sardinia and the Apennines. Ilona caused intense rainfall and wind gusts up to 30 ms^{-1} and featured deep convection at times (see also Cioni et al. 2016).

The large-scale dynamical precursors of Ilona are shown schematically in Figure 5.10. A RW packet formed on January 11 over the North Pacific, crossed the North American continent and the Atlantic and eventually underwent RW breaking over western Europe prior to Ilona's formation (further RW breaking was found to occur also during the storm's early stage). The RW packet was associated with an upper-level trough that originally formed over North America on January 11, subsequently crossed the Atlantic and deepened upon reaching western Europe (see Figure 5.11). Unlike

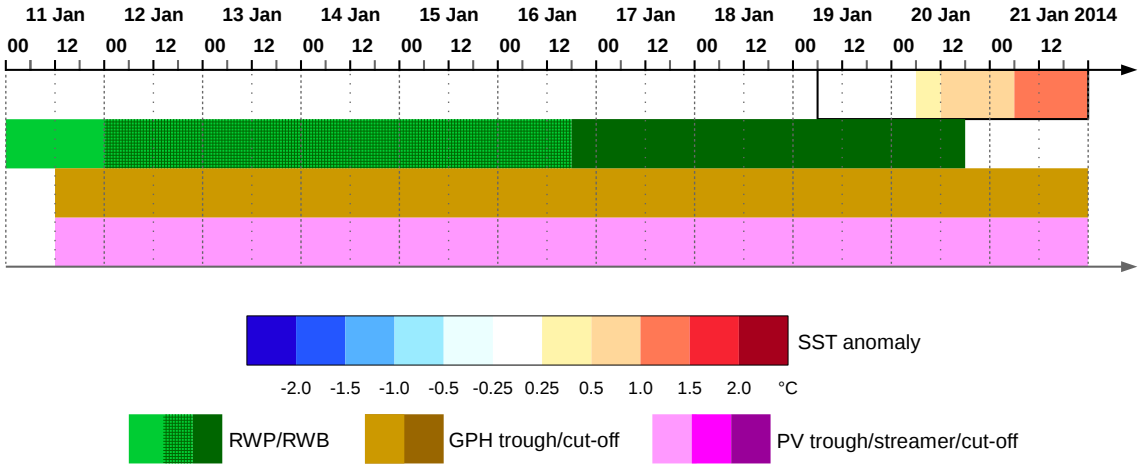

Figure 5.10: *Event calendar of cyclone Ilona, as in Figure 5.2.*

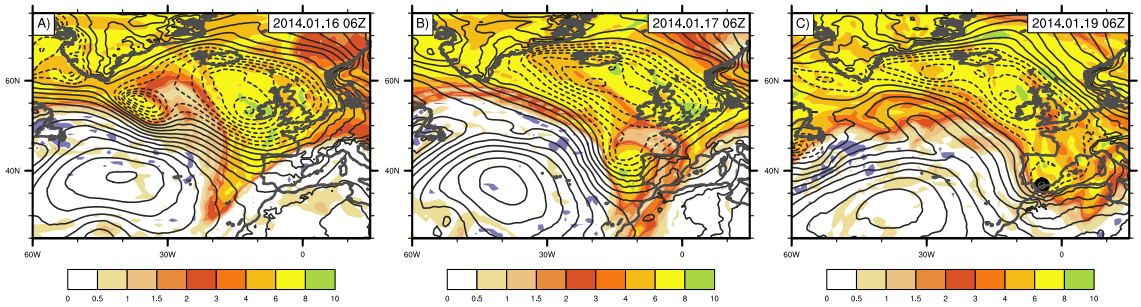

Figure 5.11: *Precursor trough of cyclone Ilona; as in Figure 5.3.*

other Medicane cases, the trough never developed into a cut-off and weakened quickly while moving northeastward, steering the storm in the same direction.

The evolution of cyclone structure is shown in Figure 5.12. Unlike other Medicanes, Ilona did not intensify after its development. The lowest CP, the most intense winds – reaching tropical storm intensity – and the highest values of symmetry and compactness are all found during the cyclone's early stage, while the storm is much weaker during its late stage. This may have been caused by the repeated interaction with orography, of Sardinia early on January 20 and of peninsular Italy a few hours later[4] (see also Cioni et al. 2016); this hypothesis is also supported by the fact that both symmetrization and the development of a warm core (successful in the lower troposphere, not in the upper troposphere) came to a halt shortly after the cyclone interacted with Sardinian orography. Another factor likely playing a role in the storm's evolution was VWS, which remained high throughout its early stage due to the absence of an upper-level cut-off.

[4]This caused the pressure low to split into two separate minima, which made cyclone tracking particularly challenging.

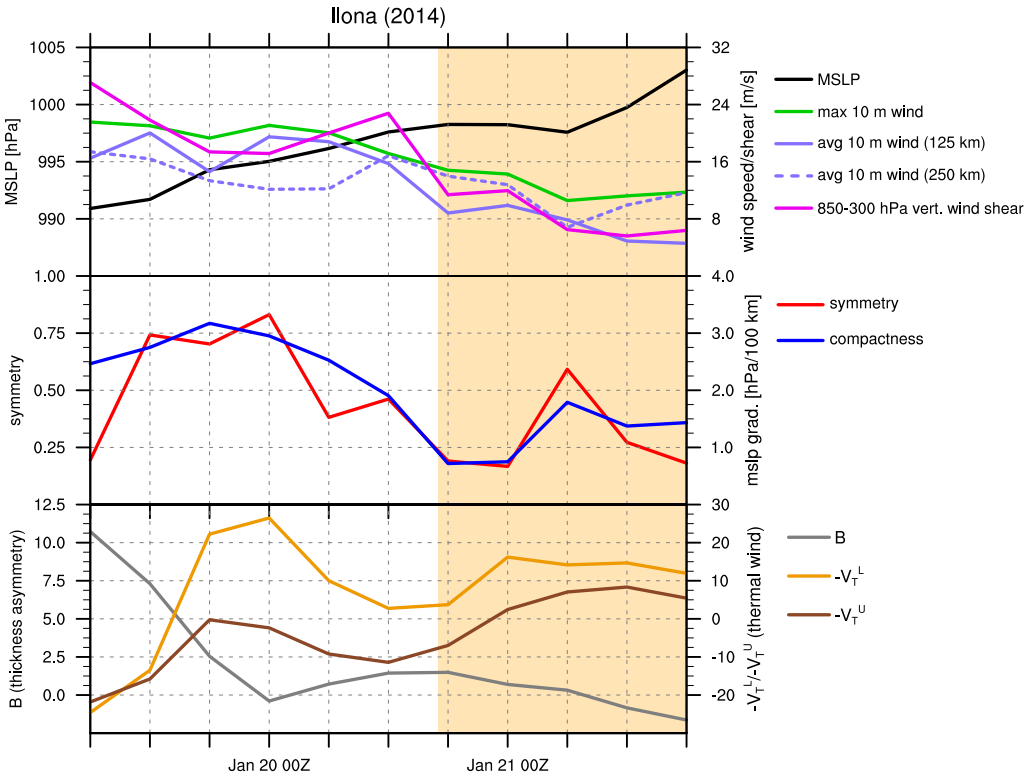

Figure 5.12: *Key features of cyclone Ilona, as in Figure 5.4.*

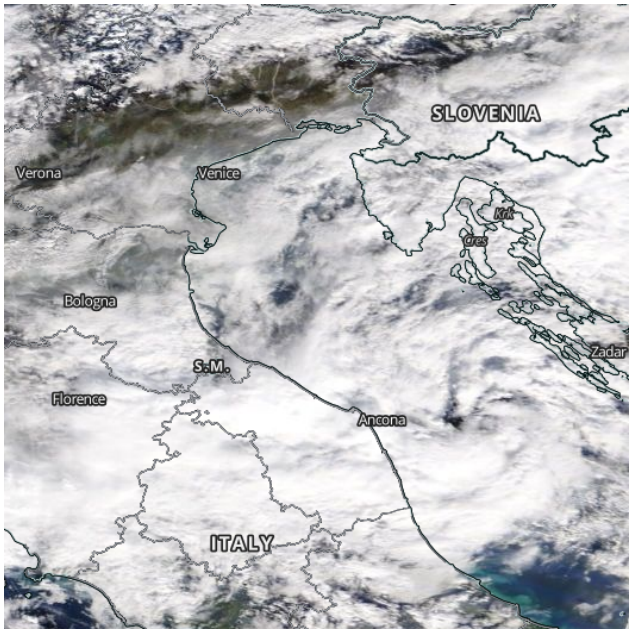

Figure 5.13: *False-color image of storm Ilona captured by NASA's MODIS Terra satellite at 1050 UTC on January 21, 2014. The picture was taken around the time the warm core magnitude peaked, during Ilona's late stage. The very small scale of the cyclone is apparent at this time.*

Ilona's intensity plateaued when it reached the Adriatic Sea, and contraction, symmetrization and warm core development all started again, attaining a weak upper-level warm core for less than one day, with $-V_T^U$ peaking just a few hours before the storm dissipated; at this time Ilona was extremely small, as can be seen in the satellite image in Figure 5.13. Anomalously warm SST in the Adriatic Sea (Figure 5.10) may have helped restart tropical transition, as also observed by Cioni et al. (2016). These authors report higher values of $-V_T^L$ and $-V_T^U$ along with lower CP, most likely due to the relatively low resolution of ECMWF analysis data and the fact that they use a much smaller radius when computing CPS parameters.

5.1.4 Qendresa (November 2014)

Probably one of the most famous recent Medicanes, storm Qendresa immediately gained the attention of the media as it occurred[5] and has been extensively studied afterwards (Carrió et al. 2017; Pytharoulis et al. 2017; Cioni et al. 2018; Pytharoulis 2018). Qendresa developed over Libya on November 6, 2014 (Figure 5.1) and underwent explosive intensification as it moved northward towards Sicily, with a drop in CP of nearly 20 hPa in 18 hours. Wind gusts exceeded 42 ms^{-1} in Malta on November 7 and extensive floods were produced[6]. Overall the storm caused over €200 million in damage, power outages, disruption to airport operations and three fatalities.

The large-scale dynamical precursors of Qendresa are shown schematically in Figure 5.14. A RW packet formed on November 3 over the Atlantic, moved towards Europe and eventually underwent RW breaking over western and southwestern Europe prior to cyclone formation. The RW packet was associated with an upper-level trough that formed over the eastern North Atlantic on November 3 (see Figure 5.15), penetrated into the Mediterranean region 2 days later and eventually developed into a cut-off during the early stage of the cyclone. The vertical alignment between the storm and the upper-level cut-off was virtually perfect during Qendresa's mature stage; as soon as the upper-level trough moved further east and vertical alignment was lost, the storm quickly weakened and eventually dissipated after few hours.

The structural evolution of the cyclone is shown in Figure 5.16. The explosive intensification of the storm was accompanied by an equally rapid symmetrization and contraction, with both symmetry and compactness peaking at the same time CP reached

[5] See e.g. https://www.washingtonpost.com/news/capital-weather-gang/wp/2014/11/07/wicked-mediterranean-storm-whips-up-95-mph-wind-gusts-in-malta.

[6] See e.g. https://www.timesofmalta.com/articles/view/20141107/local/update-3-airport-operations-resume-several-areas-without-power-cars.

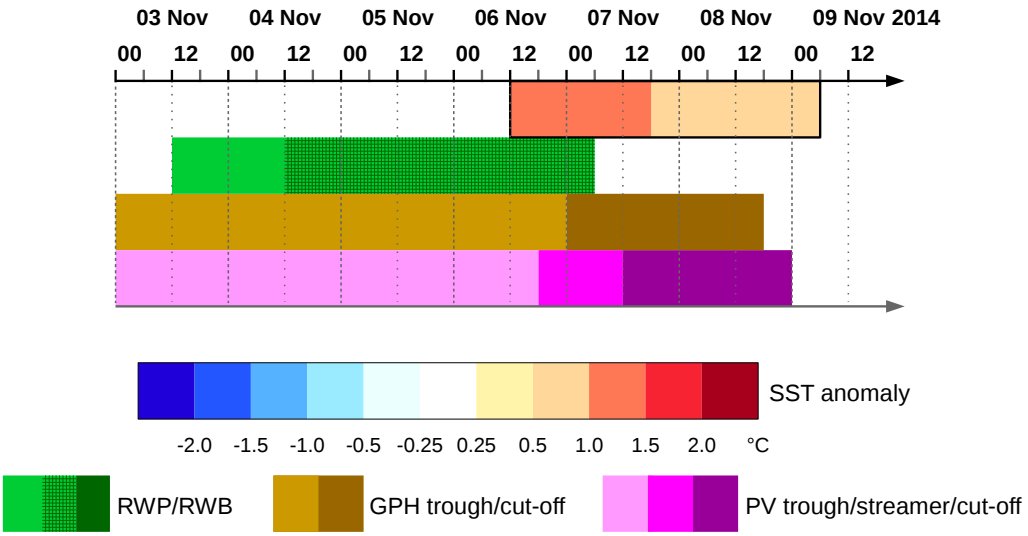

Figure 5.14: *Event calendar of cyclone Qendresa, as in Figure 5.2.*

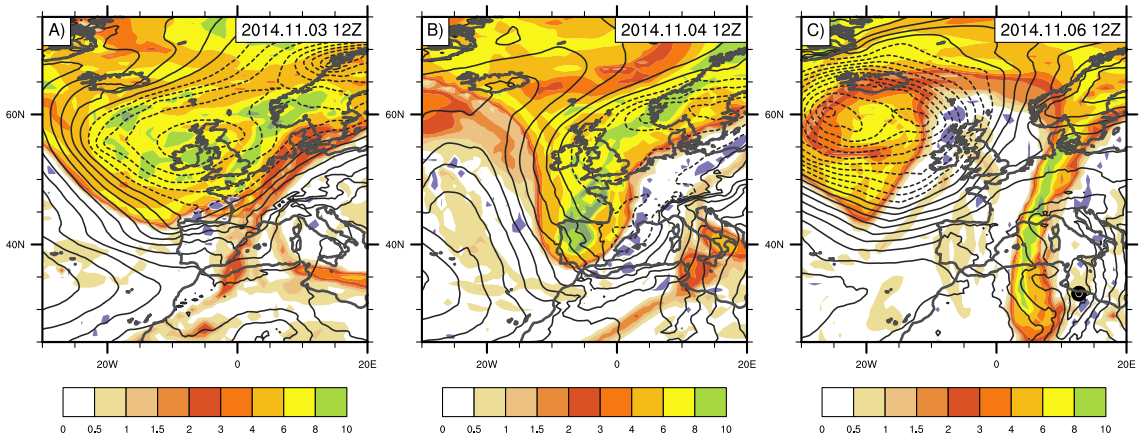

Figure 5.15: *Precursor trough of cyclone Qendresa; as in Figure 5.3.*

a minimum and wind a maximum; tropical storm intensity was attained throughout the mature stage of the cyclone. The development of a warm core was somewhat slower, with $-V_T^L$ and $-V_T^U$ peaking 12 hours later than the other parameters (Figure 5.16). Qendresa spent the first half of its lifetime over anomalously warm water (Figure 5.14), which likely promoted its intensification, as also shown by Pytharoulis (2018).

Qendresa reached an extremely small size during its mature stage, as indicated by the strong pressure gradients (compactness exceeding 11 hPa/100 km at its peak) and apparent in the satellite image in Figure 5.17. Consequently, the 100 km radius chosen here to compute CPS parameters is sufficiently large to yield lower values of $-V_T^L$ and $-V_T^U$ than those reported by Carrió et al. (2017) and Pytharoulis (2018). In fact, judging from the $-V_T^L$ and $-V_T^U$ values in Figure 5.16, there is barely a lower-level warm core for a few hours, early on November 8, while an upper-level one is not even

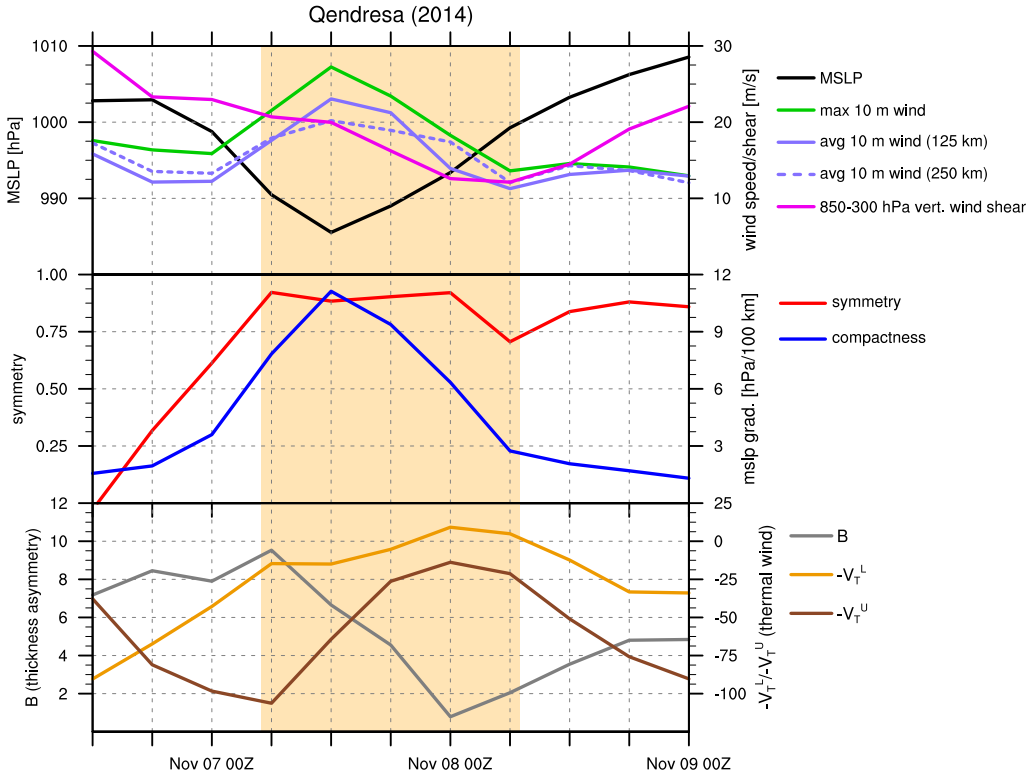

Figure 5.16: *Key features of cyclone Qendresa, as in Figure 5.4.*

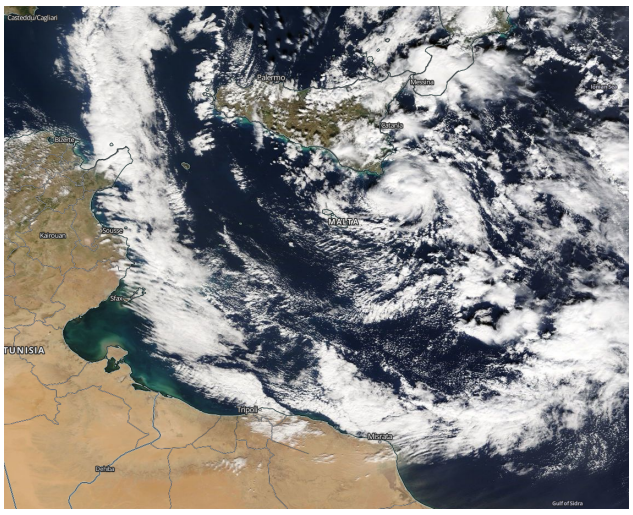

Figure 5.17: *False-color image of storm Qendresa captured by NASA's MODIS Terra satellite at 1040 UTC on November 8, 2014. The picture was captured around the time the warm core magnitude peaked, during Qendresa's mature stage. The extremely small scale of the cyclone is apparent at this time (compare with Figure 2.7 which shows approximately the same region 22 hours earlier).*

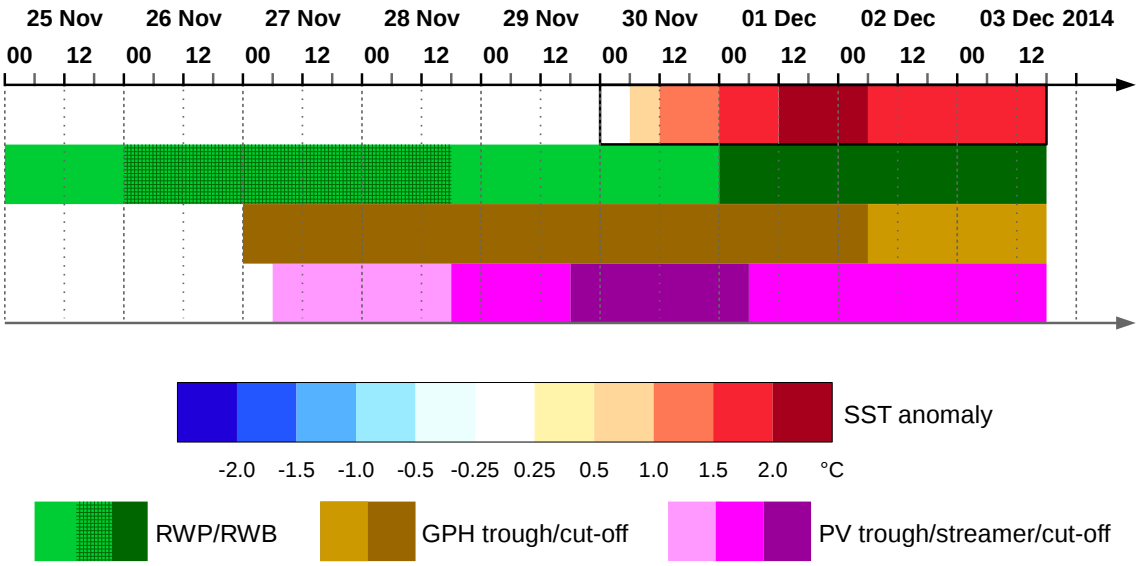

Figure 5.18: *Event calendar of cyclone Xandra, as in Figure 5.2.*

attained. This is not an error[7], but simply the result of the very high sensitivity of CPS parameters to the radius used for their calculation in case the cyclone has an extremely small size. Both $-V_T^L$ and $-V_T^U$ are much higher when computed with a smaller radius of 50–70 km[8], though their evolution in time is very similar to that of Figure 5.16, with the two curves just shifted towards higher values.

5.1.5 Xandra (November–December 2014)

Storm Xandra developed on November 30, 2014 over northern Algeria (Figure 5.1), moved northward at first and subsequently turned eastward, slowly crossing the western Mediterranean and making landfall in Sardinia on December 2, where it caused intense rainfall and some damage[9]. The storm later crossed the Tyrrhenian Sea and made landfall again in peninsular Italy, where it rapidly weakened and eventually dissipated.

The large-scale dynamical precursors of Xandra are shown schematically in Figure 5.18. A RW packet formed on November 25 over the western USA, at the same time a preexisting RW packet was crossing the Atlantic. As the first RW packet crossed the North American continent, the second underwent RW breaking over the eastern Atlantic

[7] There is ample evidence that Qendresa attained an upper-level warm core and exhibited a very similar dynamical evolution to TCs, as demonstrated by Cioni et al. (2018) and Pytharoulis (2018), who both studied this Medicane by means of dedicated high-resolution simulations.

[8] Specifically, $-V_T^L$ peaks at 37 and $-V_T^U$ at 16 if a 50 km radius is used. Such a small radius would not be suitable for ensemble forecast data, as its grid spacing is only 30 km.

[9] See https://www.centrometeoitaliano.it/notizie-meteo/maltempo-sardegna-abbondanti-precipitazioni-forte-vento-02-12-2014-22979 (in Italian).

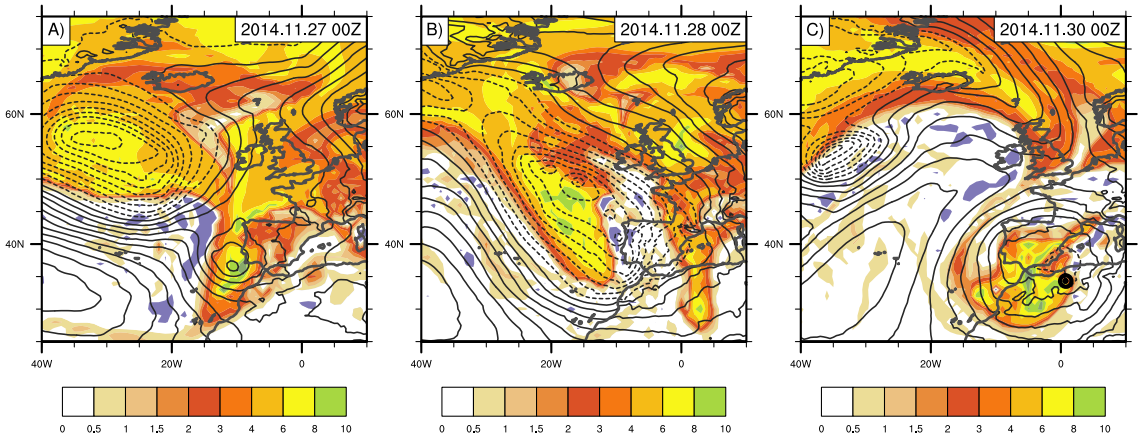

Figure 5.19: *Precursor trough of cyclone Xandra; as in Figure 5.3*

and southwestern Europe; meanwhile, a precursor low-pressure system, associated with an upper-level cut-off trough, formed over the eastern Atlantic and quickly moved towards Spain, weakening and dissipating afterwards. At this point, the first RW packet was located over the North Atlantic and a large-scale surface low had formed not far downstream. As the RW packet moved towards Europe, the pressure low shifted southeastward, followed by the associated upper-level trough (see Figure 5.19), which eventually aligned with the surface low while developing into a cut-off west of the European Atlantic coast. After reaching Spain, the low-pressure system began to shrink and it was eventually identified as a mesoscale cyclone on November 30. The RW packet began to break over western Europe a few hours later, while the cyclone started its journey through the western Mediterranean. RW breaking was observed until the storm made landfall in Sardinia and subsequently lost alignment with the upper-level cut-off, which dissipated as it moved northeastward. The weakening and dissipation of the cut-off is apparent in the PV framework, with a PV cut-off being observed only during Xandra's early stage, while an elongated, almost zonally oriented PV streamer was observed at a later time.

The evolution of cyclone structure is shown in Figure 5.20. Xandra underwent rapid symmetrization and contraction in its early stage, with a marked reduction in VWS as the cyclone became perfectly aligned with the upper-level cut-off. The lowest CP was reached just 12 hours after cyclone formation, while 10 m winds peaked 12–24 hours later. A lower-level warm core was rapidly attained during the storm's early stage, while an upper-level warm core was reached a few hours later. The mature stage of Xandra exhibits peaks of all parameters, with winds reaching tropical storm intensity for at least 36 hours and the upper-level warm core lasting equally as long,

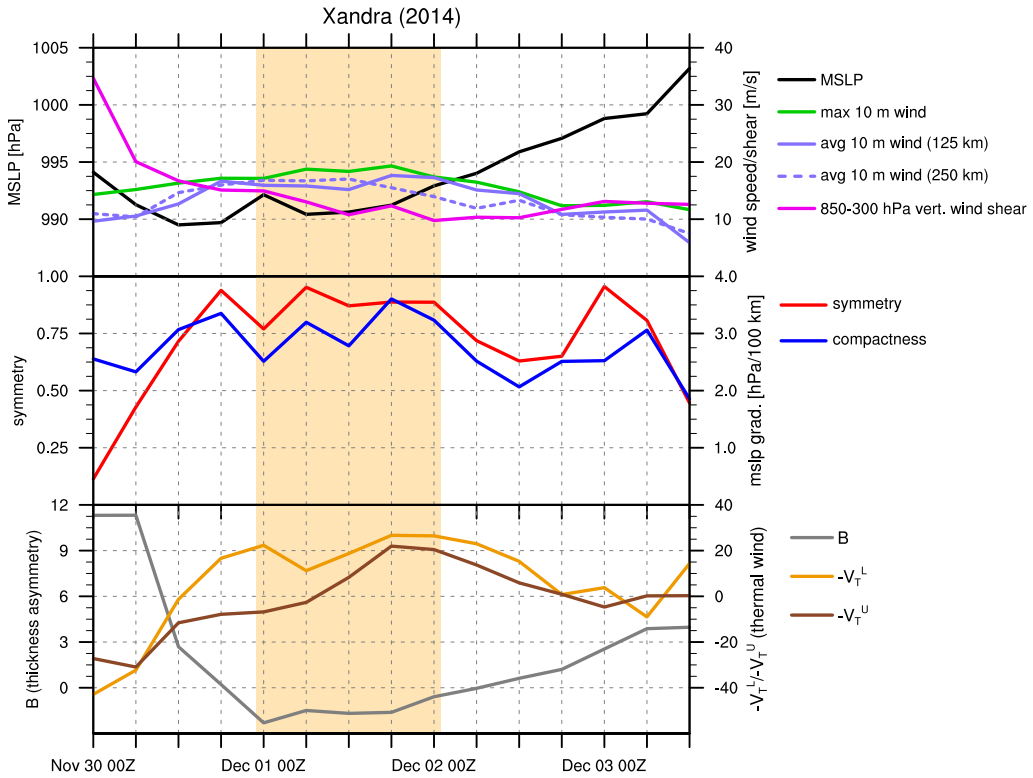

Figure 5.20: *Key features of cyclone Xandra, as in Figure 5.4.*

almost until the cyclone died out. Xandra weakened and likely lost its symmetry after interacting with the orography of Sardinia on December 2, while its long lifetime may have been favored by the large SST anomaly the storm encountered throughout its mature stage (Figure 5.18).

5.1.6 Stephanie (September 2016)

Storm Stephanie developed on September 13, 2016 over the northern Bay of Biscay (Figure 5.1), remaining in the region throughout its lifetime. The cyclone moved westward at first and subsequently turned southeastward, dissipating immediately after its landfall in northern Spain on September 16. Stephanie was clearly not a Medicane, as it occurred outside the Mediterranean. However, its appearance, structure, evolution and formation pathway are highly similar to those of most Medicanes; moreover, this storm occurred in a region that is geographically and climatologically close to the Mediterranean; for these reasons, it was considered to be akin to Medicanes and therefore included in the list of analyzed cases. Stephanie was an unprecedented storm, the first TLC ever to develop over the Bay of Biscay, and as such it immediately gained

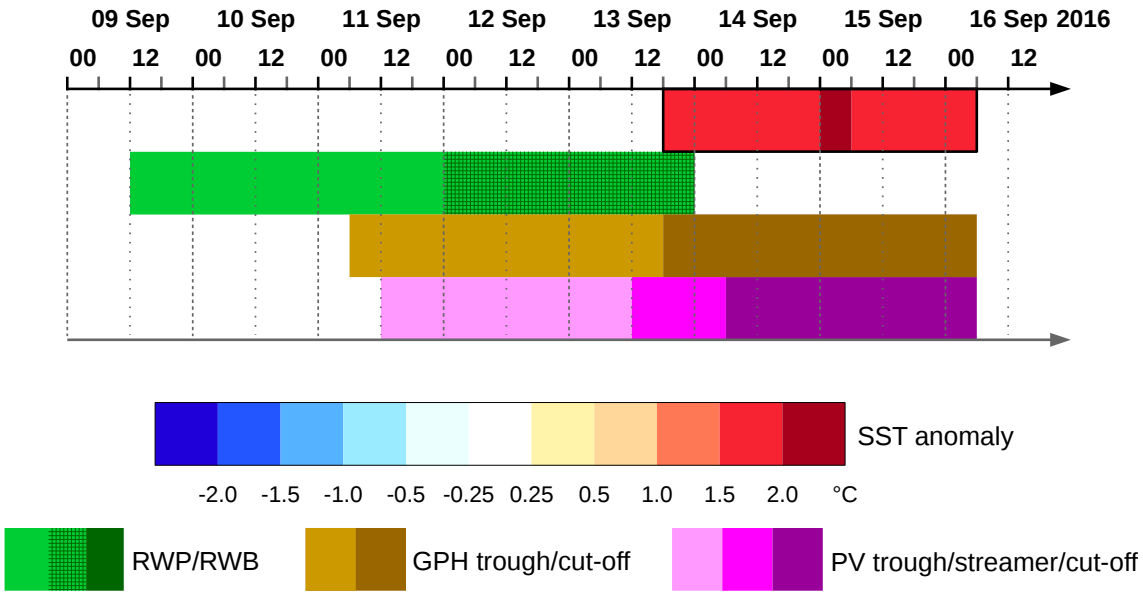

Figure 5.21: *Event calendar of cyclone Stephanie, as in Figure 5.2.*

the attention of the media as it occurred[10] and was later studied by Maier-Gerber et al. (2017). This storm did not cause extensive damage like other Medicanes, though it produced a storm surge, wind gusts over 35 ms^{-1} on the northern coast of Spain[11] and significant rainfall throughout the region[12].

The large-scale dynamical precursors of Stephanie are shown schematically in Figure 5.21. A RW packet formed on September 9 over the northwestern USA and subsequently crossed the American continent and the Atlantic, to eventually break over the eastern North Atlantic and off the coast of western Europe prior to cyclone formation. The RW packet was associated with an upper-level trough which formed over the central North Atlantic on September 11 (see Figure 5.22), moved towards western Europe and finally developed into a cut-off at the time Stephanie formed. The alignment between the storm and the upper-level cut-off was not perfect, with the latter located further to the southeast; nevertheless, the two features decayed at the same time.

The evolution of the kinematic and thermal structure of the cyclone is shown in Figure 5.23. Stephanie underwent rapid symmetrization and contraction in its early stage, with a parallel decrease in VWS, which, however, remained relatively high

[10] See e.g. https://www.bfmtv.com/planete/depression-subtropicale-dans-le-golfe-de-gascogne-un-phenomene-inedit-1037413.html (in French).

[11] See e.g. https://actualite.lachainemeteo.com/actualite-meteo/2016-09-16/un-enroulement-aux-allures-d-ouragan-sur-la-cote-atlantique-31100 (in French).

[12] See http://www.met.fu-berlin.de/wetterpate/Lebensgeschichten/Tief_STEPHANIE_12_09_16.htm (in German).

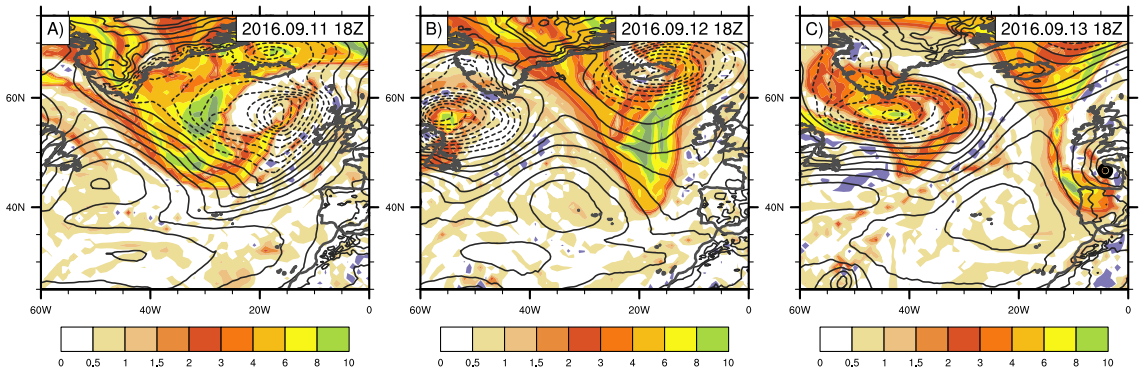

Figure 5.22: *Precursor trough of cyclone Stephanie; as in Figure 5.3, but 48 hours* (A) *and 24 hours* (B) *prior to the time of cyclone development* (C).

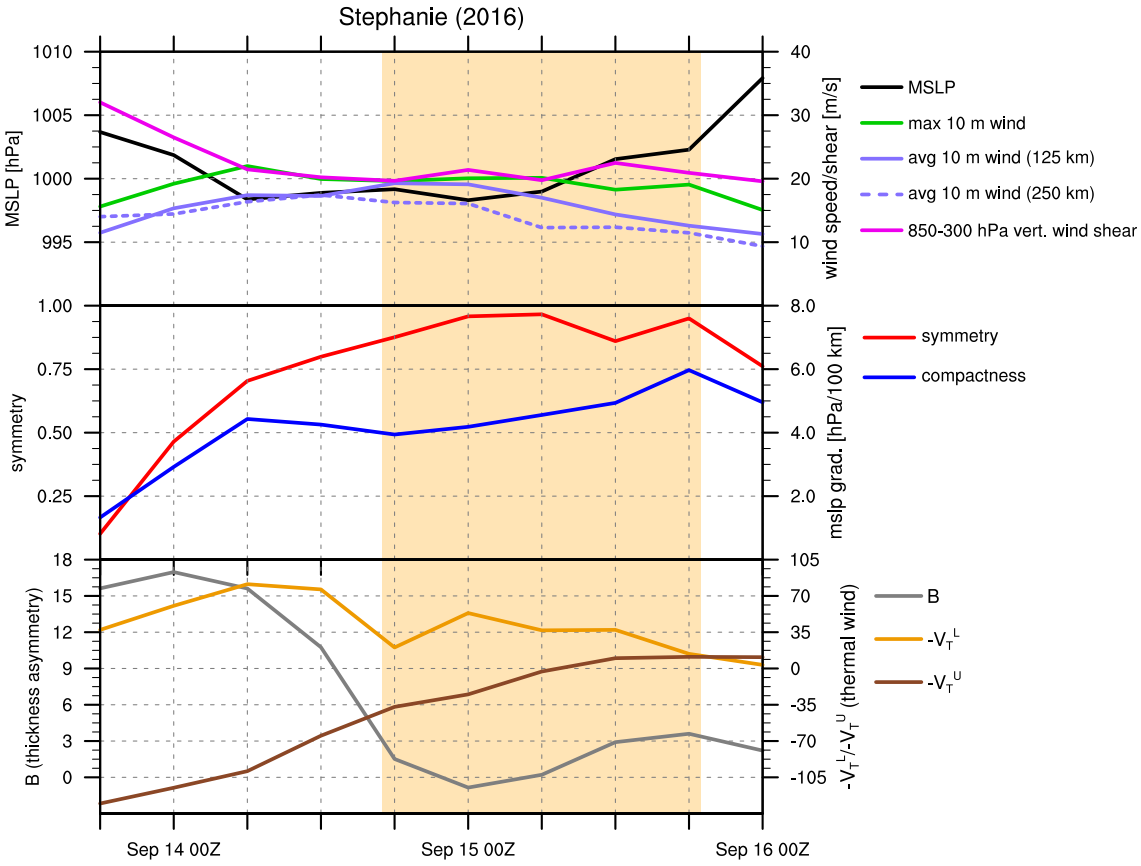

Figure 5.23: *Key features of cyclone Stephanie, as in Figure 5.4.*

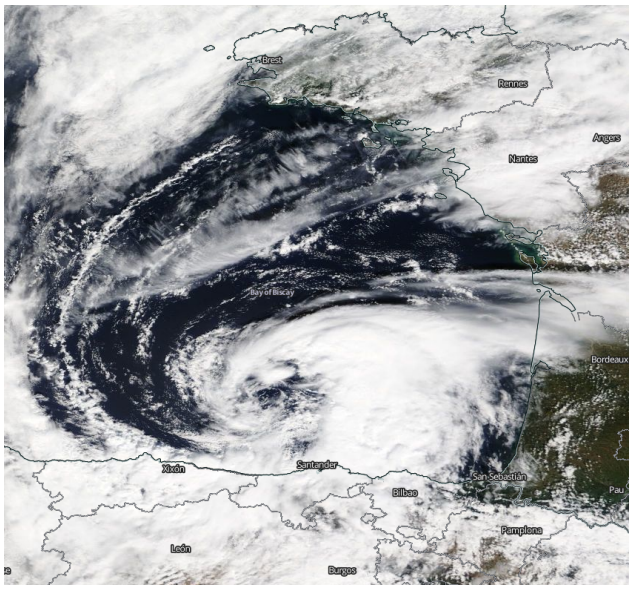

Figure 5.24: *False-color image of storm Stephanie captured by NASA's MODIS Terra satellite at 1135 UTC on September 15, 2016. The picture was captured around the time the warm core magnitude peaked, during Stephanie's mature stage.*

throughout the cyclone's lifetime. CP and 10 m winds reached a nearly steady state a mere 12 hours after the cyclone's development and tropical storm intensity was maintained until the cyclone dissipated. The build-up of an upper-level warm core was much slower, with $-V_T^U$ peaking only a few hours before the cyclone made landfall and dissipated, and may have been favored by the large SST anomaly the storm encountered throughout its lifetime (Figure 5.21). Stephanie's tropical-like traits, such as its small size, axial symmetry and central cloud-free "eye", are apparent in the satellite image in Figure 5.24.

5.1.7 Trixie (October–November 2016)

Storm Trixie developed over the Ionian Sea on October 28, 2016 (Figure 5.1). The cyclone moved very slowly during its early stage, essentially remaining in the same region, while it was much faster in its late stage, as it crossed the eastern Mediterranean, hit Crete and finally dissipated near Cyprus. Trixie was one of two Medicanes on which NOAA issued an official report[13], recognizing it as a tropical storm and naming it 90M. Trixie was one of the longest-lived Medicanes on record and produced sustained winds of nearly 30 ms^{-1} as well as significant rainfall and flooding in Malta and Crete, gaining

[13] https://www.ssd.noaa.gov/PS/TROP/2016/bulletins/archive.html; the other Medicane is Rolf, as mentioned in Subsection 5.1.1.

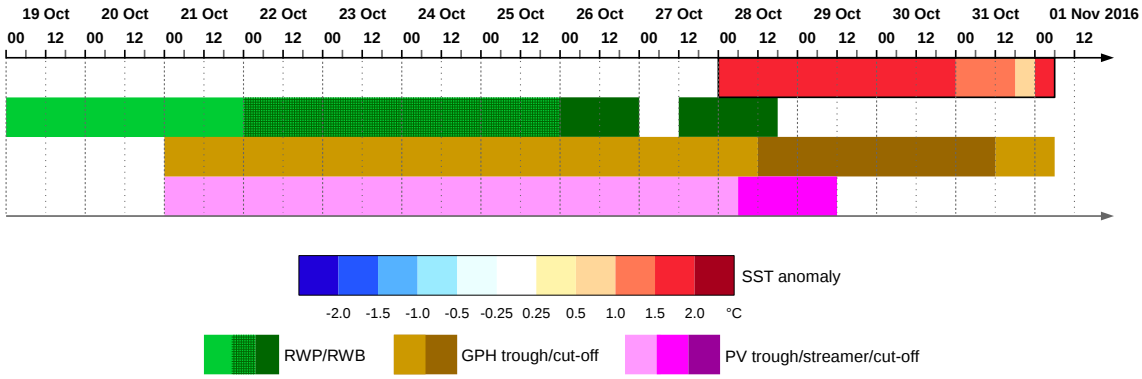

Figure 5.25: *Event calendar of cyclone Trixie, as in Figure 5.2.*

the attention of the media[14] and the Deutscher Wetterdienst (the German Weather Service)[15].

The large-scale dynamical precursors of Trixie are shown schematically in Figure 5.25. A RW packet formed on October 19 over the eastern North Pacific and subsequently crossed the American continent and the Atlantic, to eventually break over the eastern North Atlantic and northwestern Europe a few days prior to cyclone development. The RW packet was associated with an upper-level trough which formed over the North Atlantic on October 21, moved towards southwestern Europe and developed into a cut-off on October 23. While the cut-off dissipated off the western coast of Africa, the northern part of the trough continued to travel eastward (see Figure 5.26), albeit weakened, and finally penetrated into the eastern Mediterranean, where it developed into a cut-off a few hours after Trixie formed. The cut-off was vertically aligned with the surface low only during Trixie's early stage, while it later dissipated over northern Africa. Trixie was eventually reached by the jet stream, which quickly steered the storm eastward, while increasing VWS and contributing to its dissipation.

The structural evolution of the cyclone is shown in Figure 5.27. A rapid symmetrization during the storm's early hours was associated with a slight reduction of VWS and intensification, with 10 m winds reaching tropical storm intensity. The storm then reached a nearly stationary state, neither weakening nor intensifying significantly, with CP remaining around 1010 hPa – quite a weak intensity in fact; on the other hand, winds remained slightly less intense than during the cyclone's early stage. Trixie was highly axisymmetrical throughout its mature stage, while an upper-level warm

[14] See https://www.washingtonpost.com/news/capital-weather-gang/wp/2016/11/01/watch-this-rare-medicane-tropical-storm-take-shape-in-the-mediterranean, https://weather.com/news/weather/news/medicane-tropical-storm-mediterranean-sea-31oct2016 and https://www.wetteronline.de/wetternews/trixie-rauscht-auf-kreta-zu-tropensturm-im-mittelmeer-2016-10-30-me (in German).

[15] See https://www.dwd.de/DE/wetter/thema_des_tages/2016/11/1.html (in German).

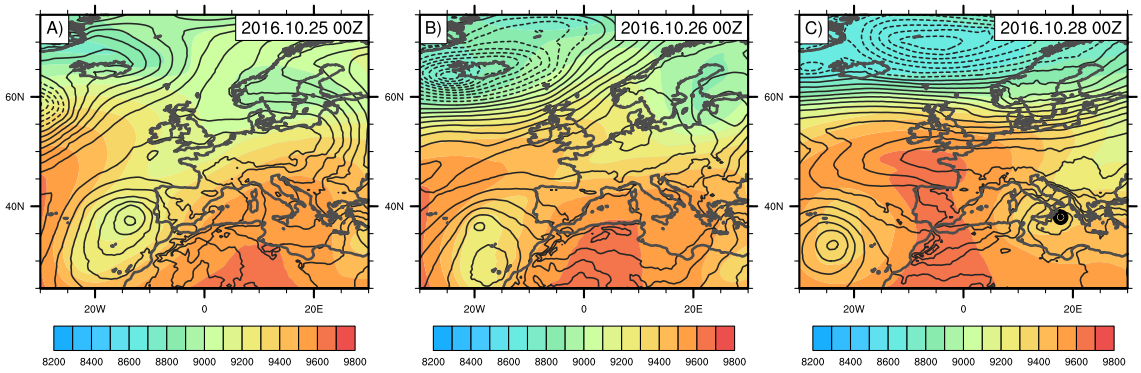

Figure 5.26: *Precursor trough of cyclone Trixie. Maps of 300 hPa (m, shading) and 1000 hPa GPH (dashed/solid contours for negative/positive values, interval 25 m), respectively 72 hours* (A) *and 48 hours* (B) *prior to the time of cyclone development* (C)*, where the black circle represents the position of the cyclone. Note that for Trixie, GPH is preferred to show the weak precursor trough, which is barely visible for PV.*

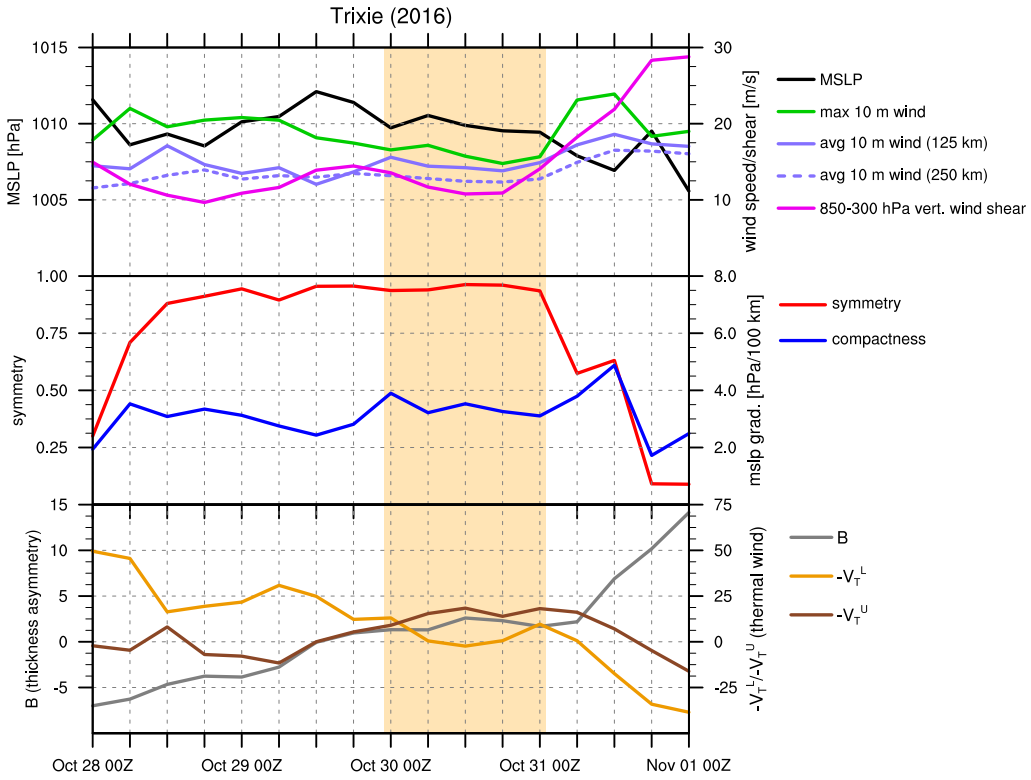

Figure 5.27: *Key features of cyclone Trixie, as in Figure 5.4.*

core slowly developed, until $-V_T^U$ peaked during the cyclone's late stage, a satellite image of which is shown in Figure 5.28. As the upper-level cut-off trough moved away from the surface low, Trixie was reached by the jet stream, as indicated by the rapid increase in VWS shown in Figure 5.27; this caused the storm to move eastward much faster than earlier and intensify again, while rapidly losing its axial symmetry and

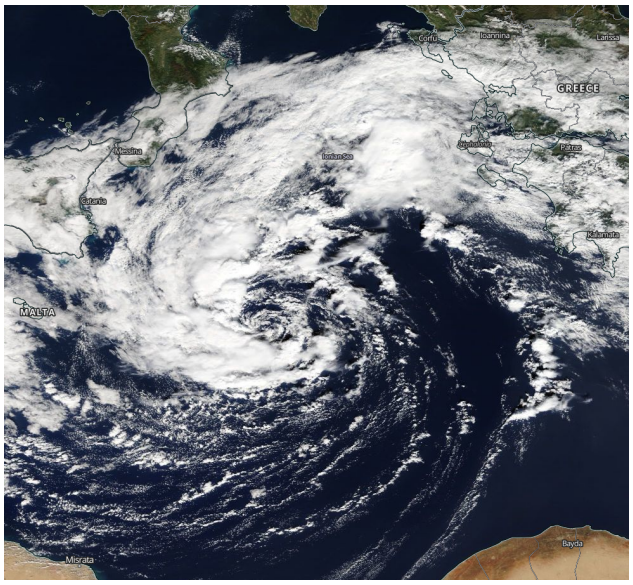

Figure 5.28: *False-color image of storm Trixie captured by NASA's MODIS Terra satellite at 0930 UTC on October 30, 2016. The picture was captured around the time the warm core magnitude peaked, during Trixie's mature stage.*

warm core. Trixie eventually dissipated as a mesoscale extratropical cyclone over the eastern Mediterranean. Anomalously warm waters in the Ionian Sea and the southern Mediterranean may have promoted the cyclone's symmetrization and the build-up of a warm core during its early and mature stage.

5.1.8 Numa (November 2017)

Storm Numa developed over the Tyrrhenian Sea on November 15, 2017 (Figure 5.1). The cyclone then quickly moved in a counterclockwise loop around Sicily and subsequently slowed down over the Ionian Sea, where it remained virtually stationary for nearly two days before moving eastward and eventually dissipating over Greece. With a 120-hour lifetime, Numa was one of the longest-lived Medicanes on record and the longest-lived among the eight events analyzed in this thesis. Furthermore, with sustained winds of nearly 28 ms^{-1}, it was also one of the most intense recent Medicanes[16]. Numa was born as a fully extratropical, synoptic-scale cyclone, and survived long enough to cause intense rainfall and floods in central and southern Italy as well as in Greece at different times during its evolution[17] and consequently gained the attention of the media[18]. However, some sources erroneously attributed the

[16] See https://medicane.wordpress.com/2017/11/17/medicane-numa-rapidly-intensifies.

[17] See http://www.met.fu-berlin.de/wetterpate/Lebensgeschichten/Tief_NUMA_12_11_17.htm (in German).

[18] See e.g. https://watchers.news/2017/11/17/rare-mediterranean-tropical-like-cyclone-forms-heading-toward-greece.

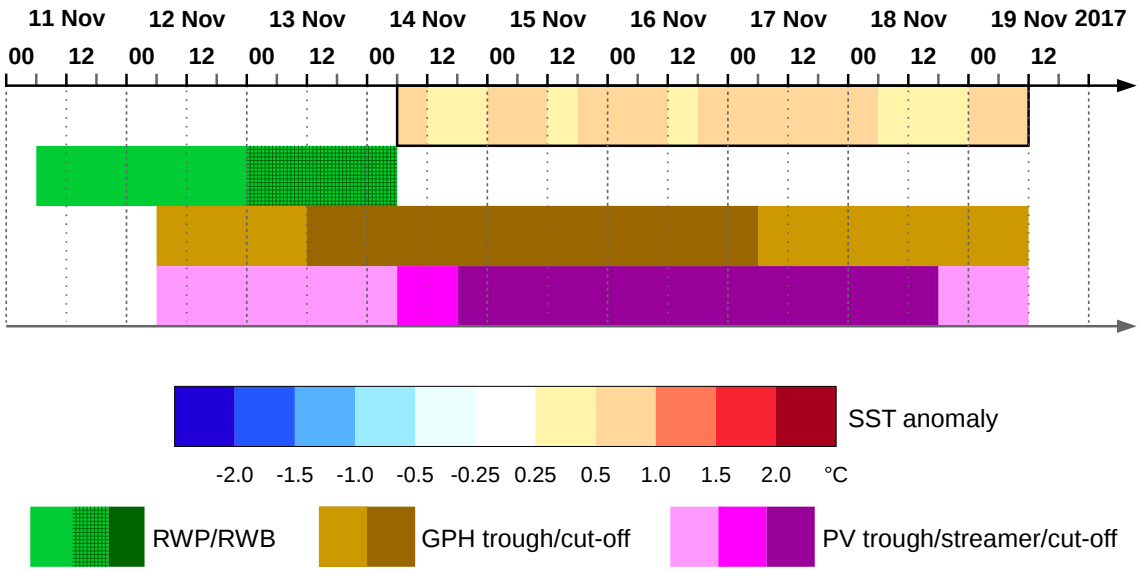

Figure 5.29: *Event calendar of cyclone Numa, as in Figure 5.2.*

considerable flood-related damage and death toll that occurred in Greece to Numa[19], whereas it was associated with a low-pressure system that preceded Numa[20].

The large-scale dynamical precursors of Numa are shown schematically in Figure 5.29. A RW packet formed on November 11 over eastern Canada and subsequently crossed the Atlantic, to eventually break over Europe and the Mediterranean region. The RW packet was associated with an upper-level trough which formed over northern Europe on November 12 (see Figure 5.30) and penetrated into the Mediterranean a day later, while developing into a large cut-off a few hours prior to cyclone formation. The alignment between the surface low and the upper-level cut-off was nearly perfect during the storm's early, baroclinic stage. However, the cut-off dissipated during the storm's mature, tropical-like stage, as the upper-level trough moved eastward and weakened. It is worth noting that two upper-level cut-off troughs had penetrated into the Mediterranean and remained in the region for many days in the two weeks preceding Numa's formation: this may have helped destabilize the atmosphere, creating an environment conducive to conditional instability and cyclogenesis.

The evolution of cyclone structure is shown in Figure 5.31. As already observed, Numa formed as a relatively large, baroclinic (cold-core) low-pressure system. An increasingly higher vertical alignment with the upper-level cut-off resulted in a decreasing VWS throughout the cyclone's early and mature stages. CP slightly increased, while

[19] See e.g. https://www.aljazeera.com/news/2017/11/storm-numa-forms-mediterranean-171119101236594.html.

[20] https://greece.greekreporter.com/2017/11/22/no-link-between-hurricane-numa-and-deadly-floods-in-greece-say-meteorologists

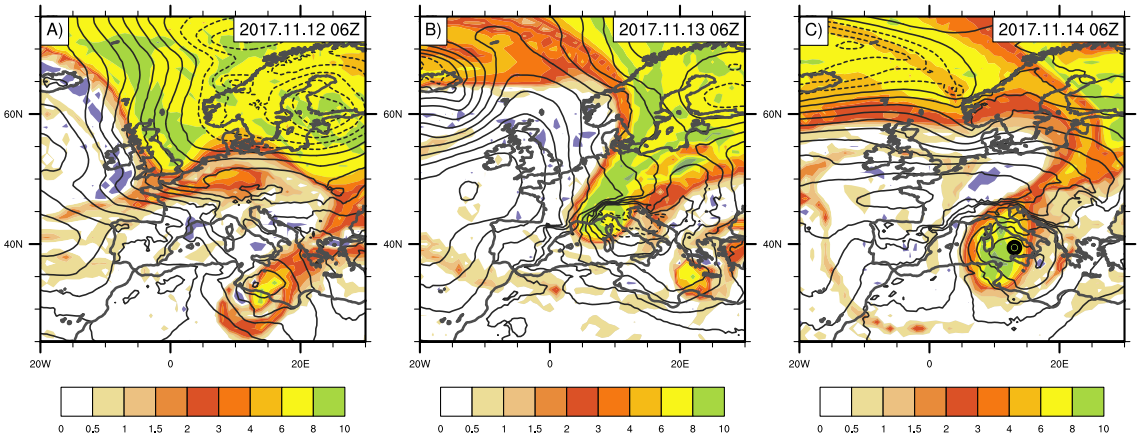

Figure 5.30: *Precursor trough of cyclone Numa; as in Figure 5.3, but 48 hours* (A) *and 24 hours* (B) *prior to the time of cyclone development* (C).

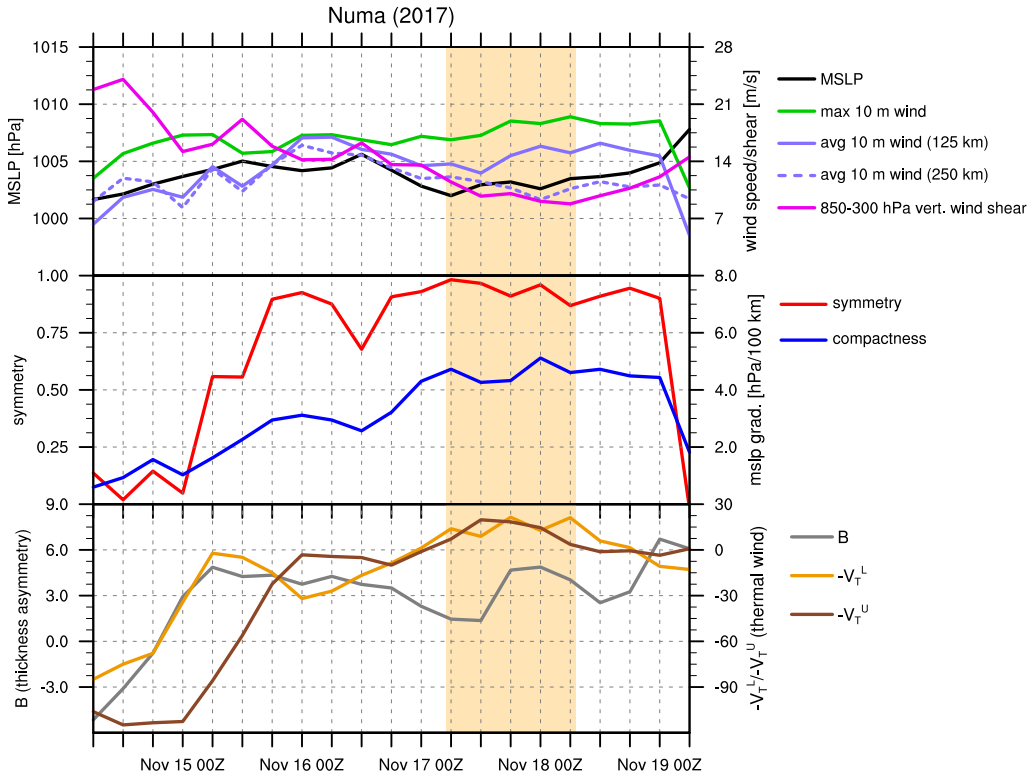

Figure 5.31: *Key features of cyclone Numa, as in Figure 5.4.*

10 m winds slightly increased as Numa underwent the structural change to tropical-like status, contracting and reaching nearly perfect axial symmetry after 36 hours. A rapid increase in both $-V_T^L$ and $-V_T^U$ in the storm's early stage indicates the build-up of a lower-level and upper-level warm core. After a short period of renewed intensification, Numa came to a halt over the Ionian Sea and a warm core was fully attained; at this time, 10 m winds reached tropical storm intensity and VWS reached its minimum; the

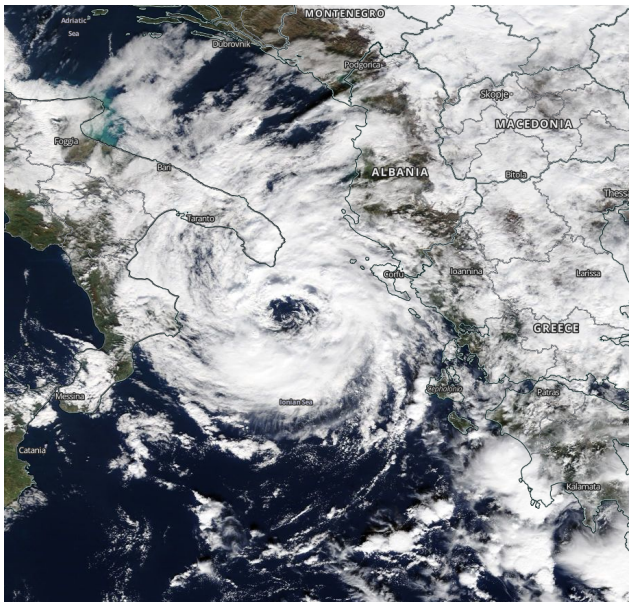

Figure 5.32: *False-color image of storm Numa captured by NASA's MODIS Terra satellite at 0930 UTC on November 18, 2017. The picture was captured around the time the warm core magnitude peaked, during Numa's mature stage.*

cyclone's small size and eye-like feature are apparent in the satellite image in Figure 5.32. After remaining in a quasi-stationary state for over one day, the storm was steered eastward, made landfall in Greece and eventually dissipated.

5.2 Overview

There seem to be common ingredients for all events, especially among precursor dynamical processes, specifically: 1) a RW packet travelling towards Europe and breaking not far upstream of the Mediterranean a few days before the storm develops; and 2) an upper-level trough penetrating into the Mediterranean prior to cyclone development and remaining somewhat vertically aligned with the surface low. However, a cut-off trough, which is generally considered to be a necessary ingredient for the development of a Medicane due to its role in promoting instability and decreasing VWS, is absent in one case, while it is only present prior to cyclone development in another case and only during the early stage in two more cases. Anomalously warm SST is found for all events and likely promotes air-sea interaction, contributing to maintain the storm even in the absence of an upper-level cut-off. However, the magnitude of the anomaly varies significantly among cases.

What emerges from the detailed description of the eight Medicane events is a complex picture, confirming what was already found in previous studies. A synergy of large-scale and mesoscale factors seems essential for the emergence of a Medicane from similar environmental conditions to those associated with fully baroclinic Mediter-

ranean cyclones. In particular, given the complex geography of the Mediterranean region, it is highly unlikely that a cyclone remains over open waters for a long time: the interaction with nearby orography is yet another factor at play which influences the evolution of the cyclone and therefore further increases the heterogeneity of Medicane events. While Medicanes share many aspects of their development pathway with North Atlantic TT events – above all, the role of air-sea instability and the trough-induced decrease of VWS – the additional complexity introduced by Mediterranean orography clearly distinguishes these two categories of subtropical cyclones. What additionally sets Medicanes apart from North Atlantic TT cases is the fact that they hardly ever reach hurricane intensity, which is mostly due to the lower SST of the Mediterranean Sea with respect to the subtropical Atlantic.

As already noted in Subsection 2.5.2, a unique, objective definition of Medicanes has not yet been established in the literature (Fita and Flaounas 2018). However, it is worth observing that all storms analyzed here share some distinctive traits, in that at some point of their lifetime they contract considerably, acquiring a largely axisymmetric circulation with strong MSLP gradients while quickly progressing towards positive values of upper-level thermal wind (i.e. building a warm core). Another feature shared by most storms is their weakening or even dissipating after making landfall, which is consistent with the fact that Medicanes, similarly to TCs, are strongly influenced by surface fluxes (Fita et al. 2007; Tous et al. 2013).

A significant underestimation of storm intensity has been found for all cases for which observational data were available (e.g. storm Rolf, Subsection 5.1.1), with ECMWF analysis data exhibiting a positive CP bias typically around 1–5 hPa, most likely owing to its relatively low resolution and the fact that it does not explicitly resolve convection. Discrepancies between the values shown in this chapter and other sources are also found for other parameters, such as the ones of the CPS (as remarked on for Qendresa in Subsection 5.1.4). While it can be expected that low-resolution analysis data underestimate storm intensity and other kinematic parameters that are strongly influenced by the small scale of Medicanes, it is worth noting that the evolution of the storm inferred from ECMWF analysis data bears a high similarity to that reported by other sources. This is an indication that Medicanes are overall well represented in ECMWF analysis data.

Chapter 6

Ensemble forecast evaluation

The results of this thesis are discussed in the present chapter, with a first focus on overall cyclone predictability in Section 6.1 and a later emphasis on the dynamics and predictability of large-scale precursor processes in Section 6.2. The rationale behind this approach is to first assess how predictable each cyclone is – specifically, how it is reproduced by ensemble forecasts and how forecasts evolve with lead time – and later concentrate on the large-scale factors influencing the cyclone's occurrence and characteristics, in an effort to understand the underlying mechanisms.

6.1 Overall predictability

In this section, a first insight into the predictability of the eight cyclones is provided in Subsection 6.1.1, where the EFI and SOT indices are used to assess the extremeness of the cyclones as far as surface winds and wind gusts are concerned. Forecasts of several cyclone-relative parameters are subsequently analyzed, with a special focus on the evolution of ensemble statistics with lead time (LT). Cyclone occurrence is first examined in Subsection 6.1.3. Cyclone position forecasts are then explored in Subsection 6.1.4. To analyze the storms' thermal structure, upper-level thermal wind is turned to in Subsection 6.1.5. The kinematic structure and intensity of the eight storms are finally discussed in Subsection 6.1.6.

6.1.1 Cyclone extremeness

Although Medicanes are relatively rare (Subsection 2.5.3), their high case-to-case variability implies that they do not necessarily belong to the most extreme Mediterranean

cyclones in terms of intensity. As a first insight into the predictability of the eight Medicane cases, it is thus worth to assess their extremeness in terms of surface winds and wind gusts by using the EFI and SOT indices: these forecast metrics, originally developed at the ECMWF and introduced in Section 4.1, provide a measure of how extreme the predicted values are with respect to the model climatology. EFI and SOT can be interpreted as follows: high EFI values (EFI $>$ 0.5) indicate a moderately (0.5 $<$ EFI $<$ 0.8) to exceptionally (0.8 $<$ EFI $<$ 1.0) high probability of unusually high winds/gusts occurring; high (positive) SOT values indicate a moderately (SOT $<$ 2) to considerably (SOT $>$ 2) high probability of extremely high winds/gusts occurring (i.e. speed exceeding the highest speed in the model climatology).

It is worth emphasizing that analyzing the mere EFI/SOT field – without any other knowledge of the ensemble forecast distribution – does not necessarily allow to deduce the cause(s) of high EFI and SOT values. These may not always be produced by the occurrence of a cyclone in each member the ensemble, but can be also due to other factors, such as fronts or orography-enhanced winds. In order to clearly separate the presence of a cyclone from other effects, each ensemble member is to be examined in detail. Nevertheless, an analysis of the geographical distribution of the EFI and SOT allows a first general assessment of the extremeness of winds and wind gusts predicted in the region and period of occurrence of a Medicane: for instance, the concentration of high values in a small, roughly circular region can be interpreted in terms of a high probability that a cyclone will cause unusually intense winds/wind gusts.

An analysis of the evolution with LT of EFI and SOT for the 24-hour time window of maximum intensity of each storm reveals a large case-to-case variability (not shown). In particular, five cases (Rolf, Qendresa, Stephanie, Trixie and Numa) show consistently high values of both indices in the region where the cyclone occurs starting from 4 to 5 days in advance, while three cases (Ruven, Ilona and Xandra) exhibit a far higher variability between different forecasts.

An example of a consistent forecast with LT is provided in Figures 6.1a and 6.1b, showing EFI and SOT respectively for 5-day and 2-day 10 m wind forecasts for storm Qendresa. The southern Mediterranean, the Ionian Sea and the Adriatic Sea exhibit extensively high values of both indices for all forecasts from 5 days LT onward. The geographical distribution of high EFI and SOT values does not change significantly with LT: in this case, the high value region does not become smaller with decreasing LT as cyclone position uncertainty is high and a significant fraction of members have the cyclone further north for LTs longer than 1 day. On the other hand, both indices tend

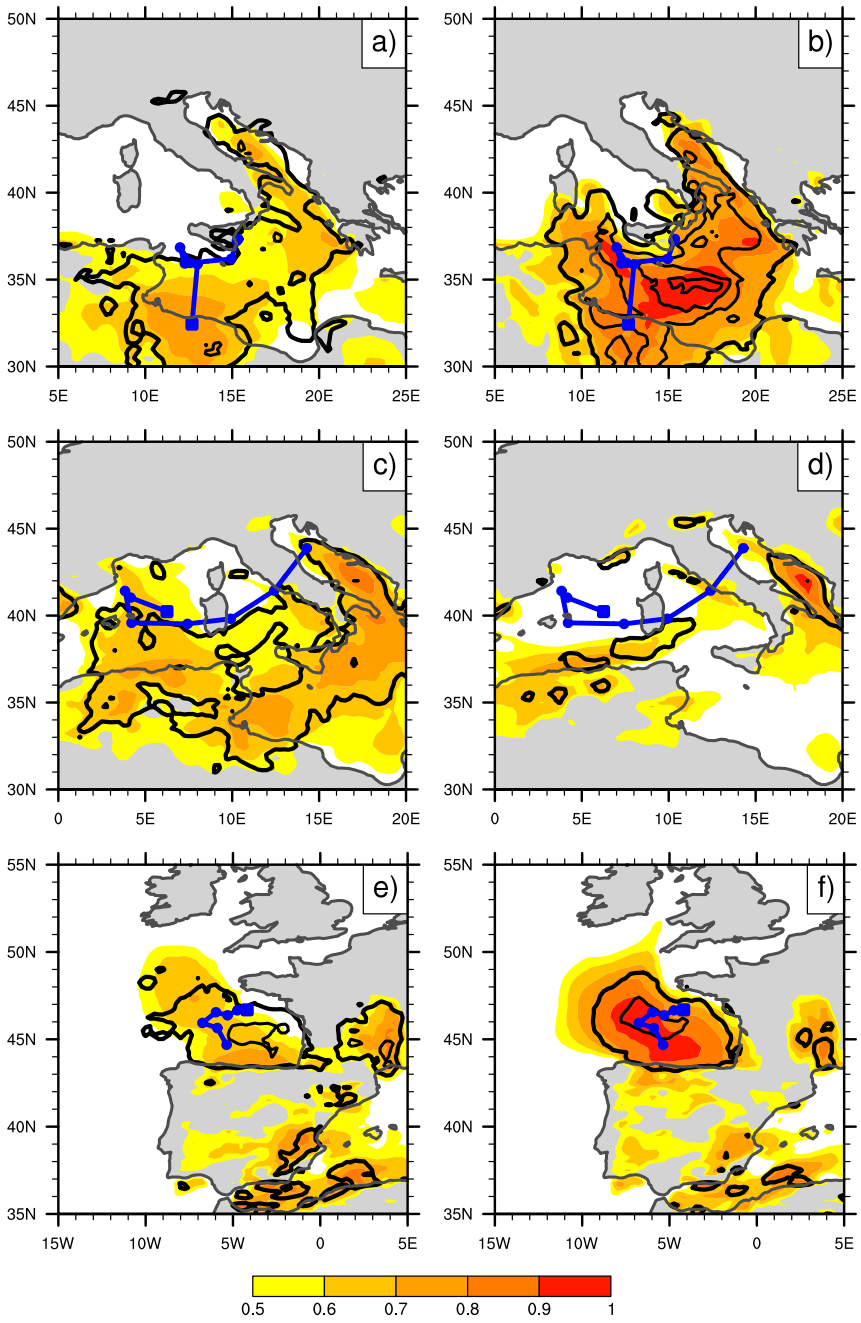

Figure 6.1: *EFI (shading) and SOT+ (black contours, thicker line is 0, interval is 1) for three cases:* (top row) *Qendresa (10 m wind), verification time window 07 to 08 November 2014 at 0000 UTC, initialization times 02 Nov. at 1200 UTC (a) and 05 Nov. at 1200 UTC (b);* (middle row) *Ruven (10 m wind gusts), verif. time window 19 to 20 November 2013 at 0000 UTC, init. times 14 Nov. at 1200 UTC (c) and 17 Nov. at 0000 UTC (d);* (middle row) *Stephanie (10 m wind gusts), verif. time window 14 to 15 September 2016 at 0000 UTC, init. times 11 Sep. at 0000 UTC (e) and 13 Sep. at 0000 UTC (f). The reference track is shown as a blue line until the final time of the verif. time window (the beginning point is shown as a square instead of a circle).*

to increase steadily with decreasing LT: the 2-day forecast exhibits a far higher chance of unusually high winds in the whole region than the 5-day forecast, with a very high chance of extreme winds southeast of Sicily (indicated by SOT exceeding 3 in Figure 6.1b). The spatial accuracy of the forecasts also tends to improve in this case, with high EFI and SOT values located closer to the observed position of the cyclone for late forecasts than for the early ones. However, such improvement is only observed for a subset of the five cases with consistent forecasts, namely Rolf, Qendresa and Stephanie, even though the overall evolution of both indices is highly similar in all five cases.

An example of distinctly variable, somewhat inconsistent forecasts is displayed in Figures 6.1c and 6.1d, showing respectively a 5-day and a 2.5-day 10 m wind gust forecast for storm Ruven. While some small regions (e.g. the southern Adriatic Sea, the northern Algerian coast and the central part of the western Italian coast) exhibit a higher consistency, EFI and SOT oscillate significantly between different forecasts in a large part of the western and southern Mediterranean. Specifically, the probability of unusually high gusts is high only in early forecasts in the southern Mediterranean (Figure 6.1c), while it fluctuates considerably in the western Mediterranean, suggesting an overall lower predictability for this case.

Two more cases are worth commenting. For storm Numa (not shown), high EFI and SOT values are confined in very small regions in the southern Mediterranean and the Ionian Sea and are lower compared to all other cases. Numa was indeed the second-weakest storm in terms of both 10 m wind and CP (Table 5.1) and the forecasts capture such aspect correctly. Conversely, storm Stephanie (Figures 6.1e and 6.1f, showing respectively a 3.5-day and a 1.5-day 10 m wind gust forecast) exhibits a consistent geographical distribution of high EFI and SOT values and a gradual increase over the Bay of Biscay, where the cyclone occurred, reaching very high EFI values in late forecasts. In this case the distribution of high values becomes increasingly round with decreasing LT and remains confined in the bay region, hinting that the high wind gusts predicted be caused by a mesoscale cyclone.

In conclusion, the qualitative analysis of EFI and SOT forecasts for all cases, albeit limited to 10 m wind speed and gusts, reveals a high case-to-case variability and a separation between five more predictable cases and three less predictable ones (predictability is to be intended here as the degree of confidence that unusual, possibly extreme conditions will occur). In three of the more predictable cases, the increasing concentration of the highest EFI and SOT values in a small, symmetrical region hints at the occurrence of an intense mesoscale cyclone.

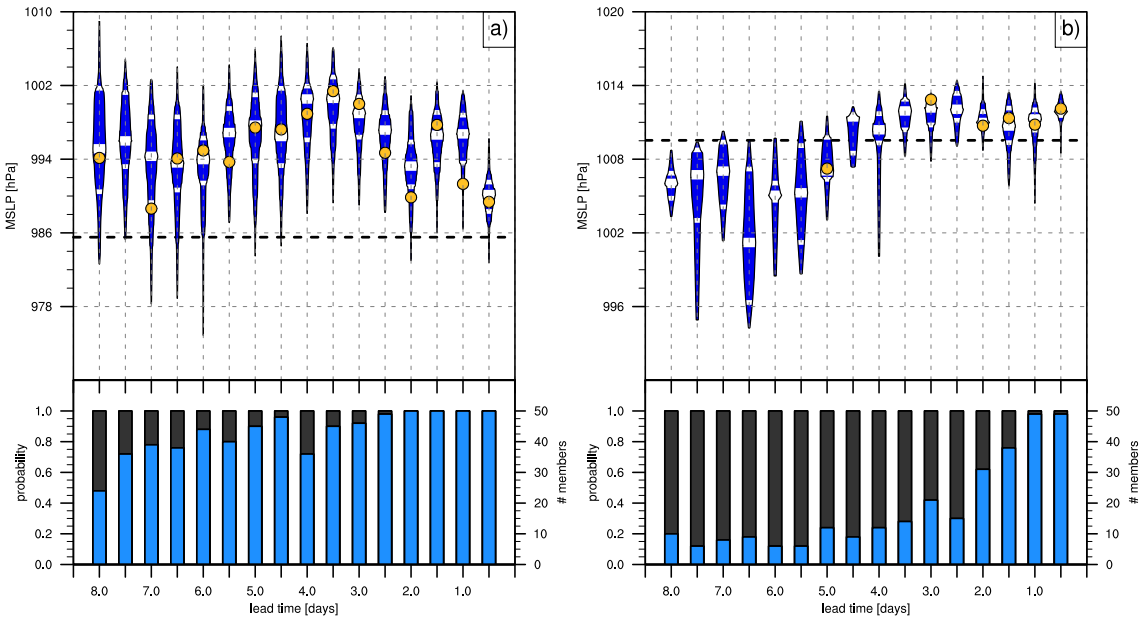

Figure 6.2: *Ensemble forecasts of CP for storms Qendresa* (a) *and Trixie* (b). *Upper panels: box-percentile plots, with white stripes marking the 25th, 50th (median) and 75th percentiles; the yellow circle denotes the control forecast value (provided it has the cyclone); the dashed line is the operational analysis value. Lower panels: number of members having the cyclone (no cyclone) are represented by blue (gray) bars. Adapted from Di Muzio et al. (2019). © The Authors. Used with permission.*

6.1.2 Case-to-case forecast variability

Two examples of the evolution of ensemble forecasts are provided in Figure 6.2, which shows CP forecasts for storms Qendresa and Trixie. These two cases illustrate the high variability among both Medicane features (see also Chapter 5) and their forecasts. Qendresa is the deepest cyclone among the eight cases, with 986 hPa minimum pressure in the ETW. For this case, the probability of cyclone occurrence (i.e. the number of storm members) is already high at 7.5 days LT (Figure 6.2a) and remains high throughout. Conversely, the ensemble median CP is far (up to 14 hPa) higher than the analysis value, with the latter consistently lying at the far lower end of the forecast distribution or even well below the lowest member. A small but evident dip is seen around 4 days LT for both occurrence probability and storm intensity. On the other hand, Trixie is the weakest cyclone among the eight cases, with over 1009 hPa, albeit very long-lived, with a lifetime of 96 hours (Table 5.1). For this case, occurrence probability is far lower than 0.5 at LTs longer than 3 days, with a considerable increase between 2.5 and 1 day LT (Figure 6.2b). The distribution of CP forecasts also shifts from having a large spread and being mostly or entirely below the analysis value (up to 5 days LT) to being mostly above it (LT shorter than 3 days) with a far smaller spread.

In both these cases, the evolution of ensemble forecasts with LT is far from gradual, with storm intensity forecasts showing little convergence towards the analysis value for Qendresa while an early convergence is followed by a plateau for Trixie; the probability of cyclone occurrence is consistently high for Qendresa, whereas it is very low for early forecasts, but grows rapidly for late forecasts for Trixie: such rapid change in the ensemble statistics is referred to as forecast jump (Section 2.2; see also Zsótér et al. 2009). It should be noted here that the distributions shown in the upper half of Figures 6.2, 6.5 and 6.6, and underlying the ellipses in Figures 6.4 and 6.7, are conditional distributions, i.e. they only comprise storm members, while leaving out no-storm members. Cyclone occurrence probabilities (appearing in the lower half of Figures 6.2, 6.5 and 6.6 and as color saturation in Figures 6.4 and 6.7) are then to be taken into account to get the full picture of, and correctly interpret, the forecast evolution.

6.1.3 Cyclone occurrence

Medicanes develop because of a combination of factors spanning multiple spatial and temporal scales and are therefore low-frequency events (Cavicchia et al. 2014a). Early signals of the occurrence of a cyclone, as seen in ensemble forecasts 5-8 days in advance, are then to be considered a first valuable piece of prognostic information. Given the greater consistency of ensemble forecasts with respect to deterministic ones (Section 2.2; see also Buizza 2008; Zsótér et al. 2009), one could expect a somewhat gradual increase of the probability of cyclone occurrence with decreasing LT. This is not the case for most cases, as forecasts often exhibit a distinctly rapid increase in occurrence probability at some LTs (forecast jump).

In order to extract such signal, the difference in the number of storm members between consecutive forecasts is computed and shown in Figure 6.3. Seven out of eight cases exhibit distinct positive peaks, i.e. a rapid increase in occurrence probability over a short interval of LT: Qendresa (7.5 days LT), Numa (around 7 days), Ruven (6 to 5 days), Rolf (around 5.5 days), Ilona (around 5 days), Stephanie (double peak around 5 and 3 days) and Trixie (2 to 1 day). These peaks stand out above the bulk of values which are contained between -1 and 5. Two cases also exhibit distinct negative peaks: Qendresa (4 days LT) and Ilona (3 to 2 days). Only one case, Xandra, shows a gradual increase of occurrence probability throughout all forecasts.

It is worth noting that six out of seven occurrence forecast jumps are found at LTs longer than 4 days. A notable exception is Trixie, for which occurrence probability

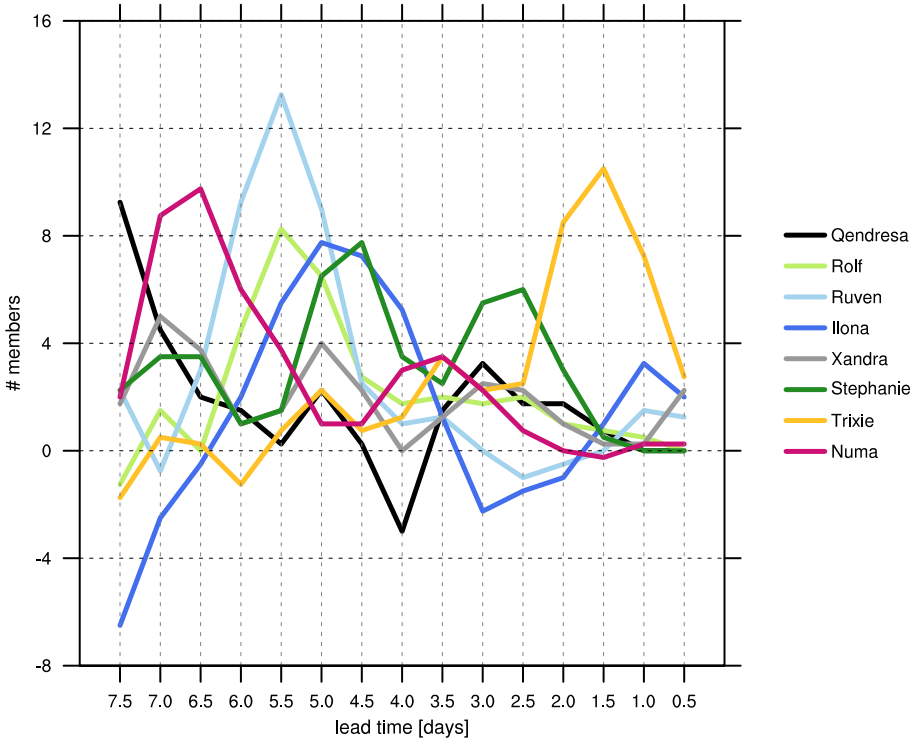

Figure 6.3: *Difference in the number of storm members (proportional to cyclone occurrence probability) between current and previous forecast, for each LT, for all cases. Values are smoothed with a 1-2-1 running mean to reduce noise. Reprinted with permission from Di Muzio et al. (2019). © The Authors.*

does not increase above 50% until 2 days LT. These results are consistent with the low likelihood of Medicane occurrence and the hypothesis that occurrence probability increases significantly only when the forecast model's initial data contain sufficient information on all processes impacting Medicane formation. Such predictability barriers constitute a source of significant unpredictability, as discussed e.g. in relation to bifurcation points in the context of extratropical transition, by Riemer and Jones (2014), and the interaction between a hurricane and an upper-level cut-off, by Pantillon et al. (2016).

6.1.4 Cyclone position

The impacts of Medicanes can be considerable (Cavicchia et al. 2014a) but spatially limited to small regions, due to their small size. For this reason, an accurate prediction of their trajectory is key in preventing and mitigating the damages they produce locally. The next step in evaluating ensemble forecasts of the eight cases is then to examine their predicted position during their mature, tropical-like phase.

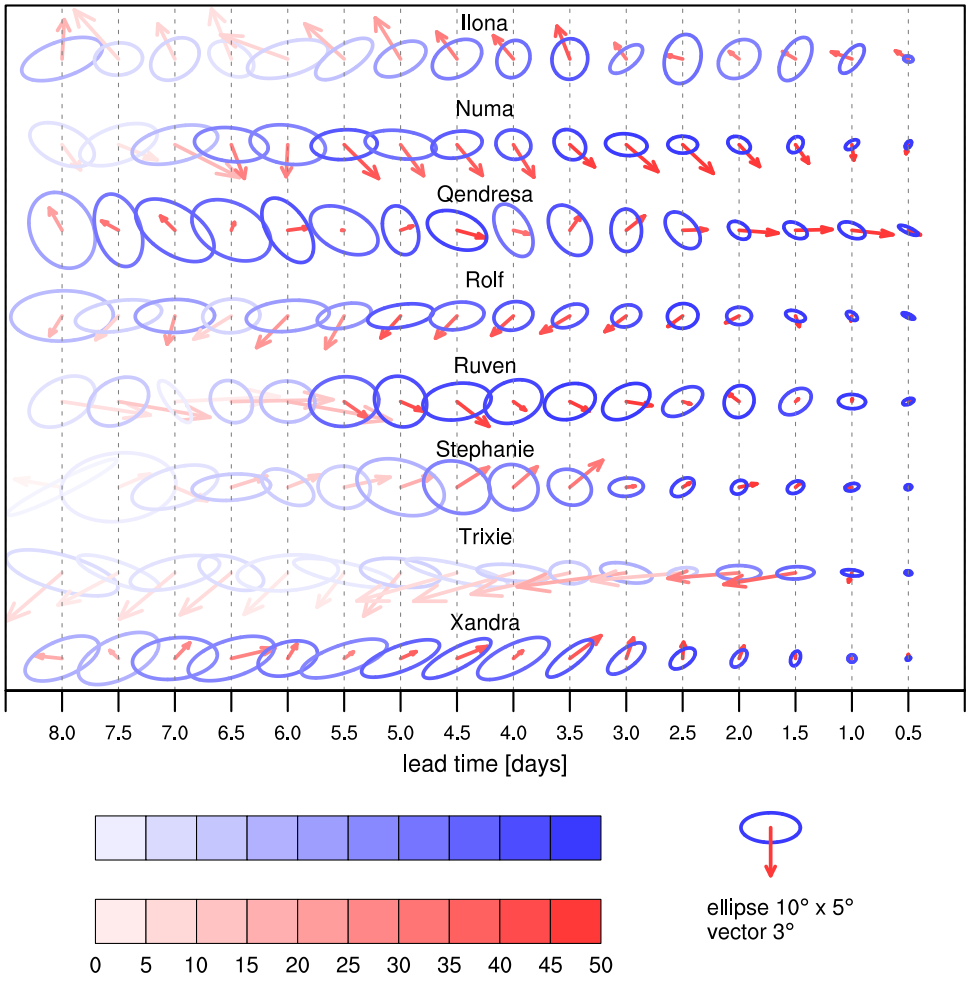

Figure 6.4: *Statistics of cyclone position forecasts. For any given forecast, only storm members are considered. The red arrow represents the median of position errors, its components being longitude (horizontal) and latitude (vertical). The blue ellipse is a bivariate normal distribution fit to the position errors, representing their spread; it is scaled so as to encircle 95% of error points. The ellipse is oriented along the direction of maximum variability of the error values and its axes are proportional to their variance in the 2D rotated coordinate system defined by the eigenvectors of their covariance matrix (see Subsection 4.9). For the sake of improving readability of the plot, two different scales are used for the median (arrows) and the actual errors (ellipses), and each arrow is made to begin from the center of the corresponding ellipse, even though such point does not correspond to zero error. The more storm members, the more saturated the colour of both ellipses and arrows. Reprinted with permission from Di Muzio et al. (2019). © The Authors.*

Cyclone position forecast statistics are shown in Figure 6.4, where the median of position errors is represented as an arrow and forecast spread as an ellipse whose axes (and hence its area) are proportional to the variance of position errors (see Subsection 4.9). These forecasts appear to converge more gradually compared with cyclone occurrence forecasts, as demonstrated by the overall slow variation of the size and tilt of both arrows and ellipses over LT (the convergence is towards a median and

spread value which is very close to zero, but not exactly zero as forecasts are evaluated in a time window). However, rapid changes of one or more of these quantities (referred to as position forecast jumps) are visible at some LTs for some cases. For instance, a sudden decrease in spread, with the ellipse decreasing in size by 30% or more between consecutive forecasts, is seen for Ilona (3 days LT), Numa (5.5 and 4.5 days), Qendresa (2 days), Rolf (5.5 days), Stephanie (3 days) and Xandra (6 days). Rapid changes in the magnitude of the median error are also apparent, e.g. for Ilona (3 days LT), Qendresa (5.5 days), Ruven (5.5 and 4 days), Stephanie (3 days), Trixie (1 day) and Xandra (3.5 days). Position forecast jumps occur in most cases at slightly shorter LTs than occurrence forecast jumps (difference is 2 days or less for Qendresa, Ilona, Numa, Ruven, Trixie, while the two jumps occur at the same LT for Rolf and Stephanie). This suggests the existence of a causal link between increased occurrence probability and higher accuracy of position forecasts.

It is worth noting that the spatial distribution of position errors tends to evolve slowly with LT. For instance, forecasts exhibit a consistent northwestern bias for Ilona (i.e. the cyclone is predicted to occur too far to the northwest), a southern to southeastern bias for Numa, a southwestern one for Rolf, a northeastern one for Stephanie (at least until 3 days LT) and a large western to southwestern one for Trixie (although in this case with low occurrence probability until 2 days LT). Similarly, position errors are consistently distributed from west to east for Numa and Trixie, from NW to SE for Qendresa and from SW to NE for Rolf and Xandra. In summary, the region where the cyclone is predicted to occur often tends to remain the same between consecutive forecasts. This implies that early forecasts may already contain valuable prognostic information, in that the actual cyclone position may be approximately estimated early on by examining the spatial distribution of position forecasts. One explanation to this may be that certain areas of the Mediterranean Sea are more conducive to Medicane development than others (Tous and Romero 2013; Cavicchia et al. 2014a) because of the spatial overlap of large-scale and small-scale favorable environmental conditions, such that it is more likely that the cyclone is predicted to spend its mature phase in these regions.

6.1.5 Thermal structure

After assessing whether a cyclone is going to occur or not and where it is going to occur, the next step is analyzing its thermal structure. For this reason, forecasts of upper-level thermal wind are now examined, as represented by the $-V_T^U$ parameter;

these forecasts are shown in Figure 6.5 for all cases. The evolution of these forecasts with LT is generally neither gradual nor monotonic, as already noted with regard to forecasts of cyclone occurrence (Subsection 6.1.3). Overall, the forecast spread does not consistently reduce with decreasing LT, with some cases exhibiting a smaller (Qendresa and Stephanie) or comparable (Ilona, Rolf, Ruven, Xandra) spread at long LTs compared with the latest forecasts. Similarly, in some cases the forecast distribution increasingly deviates from the analysis value with decreasing LT, only to get closer again in later forecasts (e.g. Ilona, Numa, Qendresa, Rolf, Stephanie).

Storms Rolf and Numa (Figure 6.5a and 6.5h, respectively) show a similar evolution, with the forecast distribution increasingly drifting away from the analysis value and the spread increasing in parallel, until the forecast distribution is mostly or even entirely below the analysis value. The forecast distribution then converges again towards the analysis, while the spread first decreases slowly, then much faster to eventually level off at short LTs. Storms Ilona and Ruven exhibit instead a contrasting evolution. For Ilona (Figure 6.5c) the forecast distribution drifts away twice from the analysis value with decreasing LT, to eventually approach it in the latest forecasts; the spread oscillates considerably between consecutive forecasts throughout the period considered. For Ruven (Figure 6.5b) the distribution changes little in shape and position, with the spread remaining nearly constant throughout all forecasts and the median always somewhat close to the analysis value.

A peculiar evolution is exhibited by storm Xandra (Figure 6.5e). Early forecasts have very little spread and the analysis value lies consistently beyond the upper end of the forecast distribution. The spread then increases considerably between 4 and 2 days LT as the distribution shifts to higher $-V_T^U$ values. The spread finally decreases again rapidly in the latest forecasts while the forecast distribution remains slightly below the analysis value for the most part. This behaviour can be interpreted as follows: with relatively high cyclone occurrence probability (0.6 and higher) and little spread at the longer LTs, ensemble forecasts indicate the development of a weaker warm core or a cold core. The increase in spread with decreasing LT, which is associated with a slight rise of the occurrence probability, indicates that new information available in the initial conditions allows the development of a warmer upper-level core to occur in some ensemble members, i.e. a higher probability of a Medicane developing.

Forecasts of cyclone thermal structure do not appear to be consistently linked to occurrence probability. However, some cases show interesting behaviours: for instance, for Rolf (Figure 6.5a) the forecast distribution approaches closely the analysis value

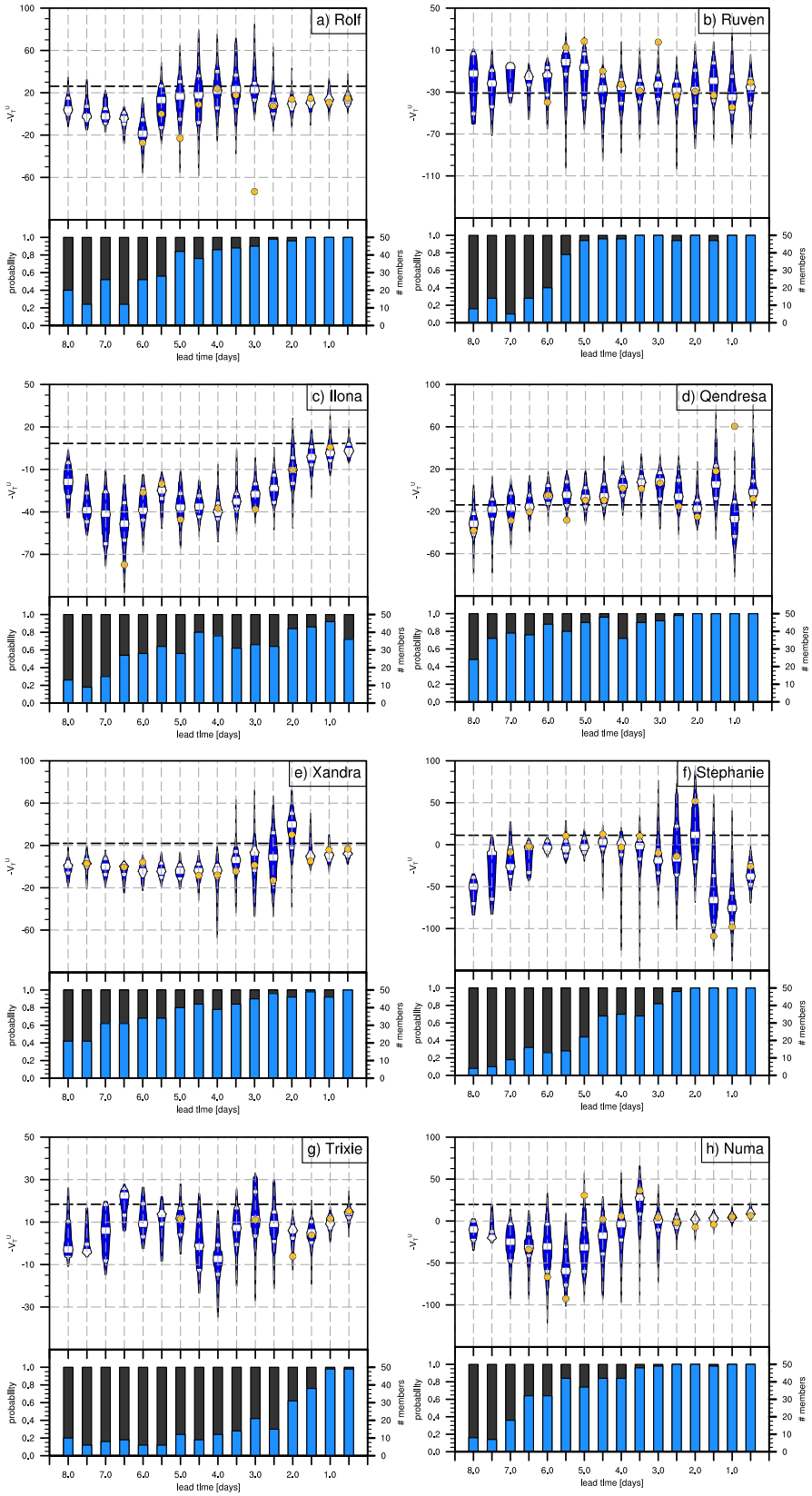

Figure 6.5: *As in Figure 6.2, but for upper-level thermal wind ($-V_T^U$) forecasts and for all cases. Adapted from Di Muzio et al. (2019). © The Authors. Used with permission.*

only when probability is higher than 0.8; for Stephanie (Figure 6.5f) the increase in occurrence probability around 4.5 days LT appears to be associated at first to a broadening of the $-V_T^U$ forecast distribution and later to its shift towards lower values; for Trixie (Figure 6.5g) the rapid increase in occurrence probability at 2 days LT is associated with a reduction in the $-V_T^U$ forecast spread.

In all cases, forecasts initialized when the cyclone has already developed have a far lower spread of upper-level thermal wind than previous forecasts and their distribution also tends to be closer to the analysis value. This is probably explained by the inherently low probability of Medicane occurrence and the fact that the development of a warm core depends on a variety of factors, including small-scale ones such as surface fluxes, such that a preexisting cyclone constitutes a marked improvement in the initial conditions. It is worth observing that the latest (0.5 day) $-V_T^U$ forecast is more accurate than earlier ones in most cases, in terms of the ensemble distribution being closer to the analysis value and its spread being lower, while the analysis value lies within the distribution in all cases. Overall, this is evidence that the ECMWF ensemble model can adequately reproduce warm-core cyclones despite its relatively low horizontal resolution.

6.1.6 Kinematic structure and intensity

The last step in analyzing the ensemble forecasts of the eight cases is assessing how their kinematic structure and intensity are predicted by examining forecasts of symmetry, compactness and CP. Overall, these forecasts also show a non-gradual evolution with LT, as previously observed for occurrence, position and thermal structure forecasts. Specifically, the forecast distribution often does not converge gradually and monotonically towards the analysis value, the spread does not always decrease gradually nor monotonically and forecast jumps occur at some LTs for most cases. However, the evolution of these forecasts is more gradual than that of the forecasts previously examined. For this reason, a particular focus is given here to the overall performance of these forecasts rather than on their evolution with LT. Full forecast statistics are only shown for two representative cases, namely Numa for compactness (Figure 6.6a) and Stephanie for symmetry (Figure 6.6b).

It is apparent that the forecast distribution of both compactness and symmetry consistently lies mostly, if not entirely, below the analysis value in these two cases, though with a clear convergence towards the analysis value at short LTs. These two forecasts are representative of compactness and symmetry forecasts for other cases, in

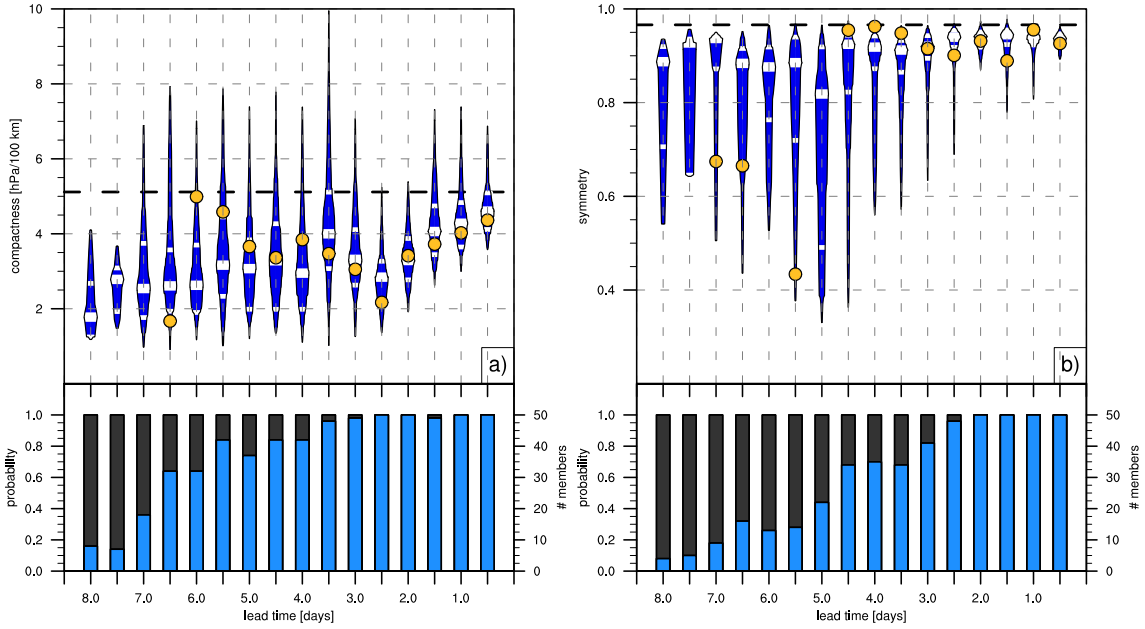

Figure 6.6: *As in Figure 6.2, but for a) the compactness forecast for Numa and b) the symmetry forecast for Stephanie. Adapted from Di Muzio et al. (2019). © The Authors. Used with permission.*

that a similar behaviour is seen in most cases. One could naturally expect compactness to be systematically underpredicted to some extent, given the low resolution of the ECMWF ensemble prediction model. However, the clear convergence of forecasts at short LTs, with a markedly reduced spread and an overall far closer distribution to the analysis value, as well as the fact that the distribution tails reach or exceed the analysis value even at long LTs, indicate that the model is capable of producing high values of compactness. Moreover, compactness and symmetry forecasts appear to be well correlated with each other, such that high values of either parameter are associated with high values of the other. In conclusion, the underdispersion arises at long LTs because the occurrence of a very symmetric and compact cyclone is a highly unlikely event and, as such, it is by nature near the tail of the forecast distribution (especially at long LTs), as observed by Majumdar and Torn (2014). Late forecasts thus tend to converge at short LTs as they benefit from improved initial conditions.

It is worth noting that CP forecasts (not shown) are overall the most gradually evolving forecasts with LT, albeit with a tendency for the distribution to lie mostly (more rarely entirely) above the analysis value at long LTs for many cases, which is associated with the low probability of cyclone occurrence in early forecasts. This hypothesis is supported by forecasts of Qendresa, the most intense of the eight storms (see Section 5), for which the analysis value lies consistently at the far lower tail of the forecast distribution at long LTs (Figure 6.2a). Qendresa indeed underwent an

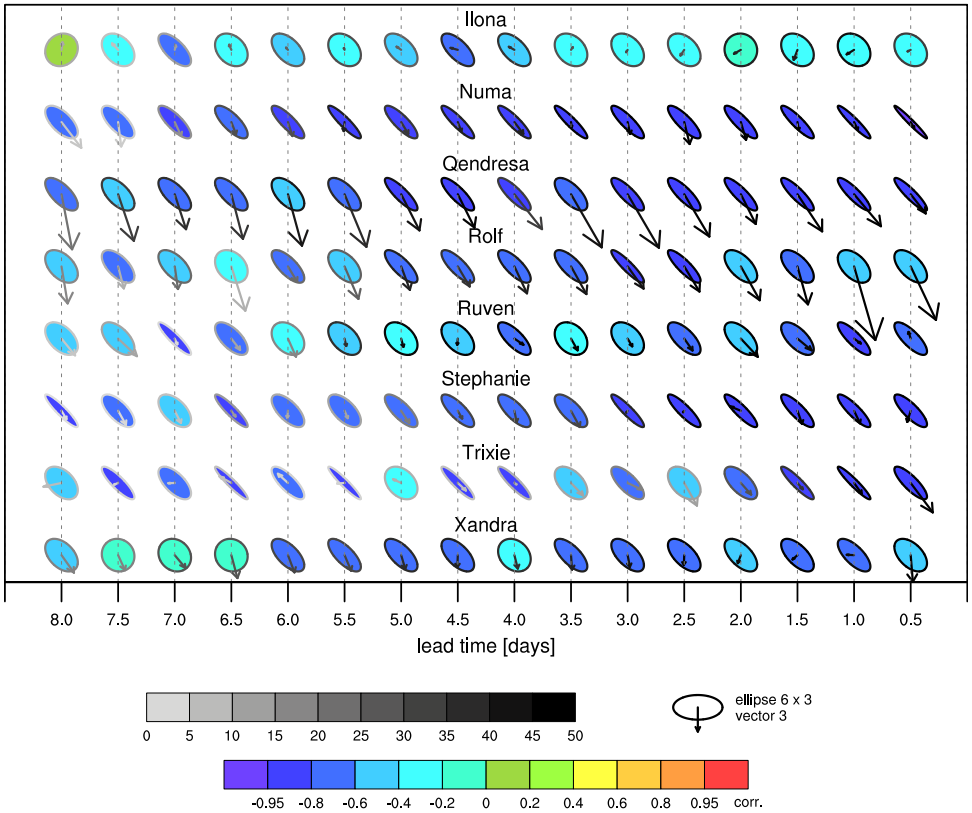

Figure 6.7: *As in Figure 6.4, but for CP and compactness standardized errors. For each member of each forecast, the standardized error is calculated as the difference between the member value and the reference (analysis) value, divided by the ensemble standard deviation; for this reason, errors are nondimensional here, unlike in Figure 6.4. CP corresponds to the x axis, compactness to the y axis of each ellipse. For each forecast, the ellipse and arrow lines are colored according to the number of storm members, while the ellipse fill color indicates the correlation between CP and compactness errors.*

extremely rapid development (more than 15 hPa pressure drop in 18 hours, see Cioni et al. 2018) which appears as highly unlikely especially in early forecasts, even though the probability of cyclone occurrence is high from 7 days in advance (Figure 6.2). The fact that the underdispersion is more evident for symmetry and compactness than for CP supports the idea that Medicanes are more distinctly characterized by their high compactness and symmetry than by their intensity, with the former far less predictable than the latter, especially at long LTs.

Finally, the joint variability of CP and compactness forecasts is examined and displayed in Figure 6.7. Here, as in Figure 6.4, the arrows represent the median forecast error, while the ellipses show the two-dimensional distribution of forecast errors. An overall tendency to underpredict compactness is apparent, with most arrows oriented nearly vertically, as the compactness component has a larger influence than the

CP one on the standardized (nondimensional) error. As was already commented above, the fact that the larger errors are found for the two cases with the highest compactness, namely Qendresa and Rolf, and a general decreasing tendency with decreasing LT, can be interpreted as a consequence of the low probability of the occurrence of a highly compact cyclone.

More interestingly, the large anticorrelation that is apparent for all cases – indicating that the members having the highest compactness also have the lowest CP and vice versa – hints at a strong link between the intensification and contraction of the predicted cyclones. This is consistent with the known intensification mechanisms of Medicanes (Subsection 2.5.1), with small-scale, convective processes playing a major role in maintaining the storm while promoting its contraction. Such intensification mechanisms are highly different from those of larger, fully baroclinic Mediterranean cyclones, for which CP and compactness would not be strongly related. The large anticorrelation in Figure 6.7 thus hints at the tropical-like nature of the eight cases, while confirming that ECMWF ensemble forecasts can effectively reproduce such nature.

At a closer look, it can be seen that five out of eight cases (namely Numa, Qendresa, Rolf, Stephanie and Trixie) exhibit consistently lower correlation (i.e. higher anticorrelation) than the other cases, whose correlation values oscillate more. This partitioning is the same found from the analysis of the EFI and SOT indices (Subsection 6.1.1): in both circumstances the consistency of forecasts is lower for Ruven, Ilona and Xandra than for the other five cases. In order to interpret this lower consistency in forecast evolution, one has to keep in mind that Ruven has been considered a "failed Medicane" (Subsection 5.1.2) and that Ilona reached its peak warm core shortly before its dissipation, while it was extremely weak and small (Subsection 5.1.3). The lower consistency may then be interpreted as reduced predictability in a situation of uncertain evolution pathway, as opposed to the higher consistency of the other five cases, which exhibit a higher predictability in terms of probability of an extreme, tropical-like cyclone occurring.

6.2 Large-scale dynamics and predictability

In this section, the focus shifts to the dynamics and predictability of large-scale processes that are typically associated with Medicanes, namely Rossby wave packets and Rossby wave breaking, which are examined in Subsection 6.2.1, and upper-level cut-off troughs, which are investigated in Subsection 6.2.2. The goal is here twofold: to determine

how predictable these precursor structures are on the one hand, and to assess what their influence is on the occurrence and structure of the cyclone on the other hand.

6.2.1 Rossby wave packets and breaking

In Chapter 5, a large-scale dynamical ingredient to the development of all Medicane cases was identified in a large RW packet forming far upstream of the Mediterranean Sea, usually over the western or central Atlantic, several days prior to Medicane occurrence. Such RW packet typically travels eastward, crossing the ocean and eventually breaking over the eastern Atlantic or western/southwestern Europe: this is in turn associated with the formation of an upper-level trough which constitutes the precursor dynamical feature to all Medicane events and often, though not always, survives throughout the cyclone's lifetime. In this subsection, the predictability of the RW packet and RW breaking is examined as well as their influence on the development and thermal structure of the cyclone.

RW packets are the largest-scale component in the downscale cascade of dynamical processes leading to Medicane development and therefore can be expected to exhibit the highest probability of occurrence in short-range to medium-range ensemble forecasts. An example of such forecasts is shown in Figures 6.8a and 6.8b for storm Qendresa, for the same RW packet at two different forecast times, at 0000 UTC on November 5 and November 6, 2014, respectively. While the RW packet was large and strong (in terms of magnitude) on November 5, RW breaking was already occurring over western Europe and the RW packet was much smaller and weaker on November 6, just one day before dissipating. As can be seen in Figure 6.8a, the majority of members have the RW packet in all forecasts, with occurrence probability higher than 75% at all LTs but those higher than 6 days. The spread of RW packet longitude forecasts decreases relatively steadily with decreasing LT, with few outliers for late forecasts (LTs of 4 days and shorter). This evolution is typical for large, mature RW packets and is seen for most cases and for most RW-related forecast metrics (not shown).

On the other hand, the evolution of forecasts for decaying RW packets usually shows a lower occurrence probability for early forecasts (LTs longer than 5 days) with a more marked increase with decreasing LT, as can be seen in Figure 6.8b. This can be interpreted as the consequence of both 1) the fact that a decaying RW packet can be considered as a transitioning feature and therefore has a reduced predictability (this is often seen for blocking, see e.g. Tibaldi and Molteni 1990), and 2) the definition of RW packets as objects through the use of an envelope threshold, which causes a

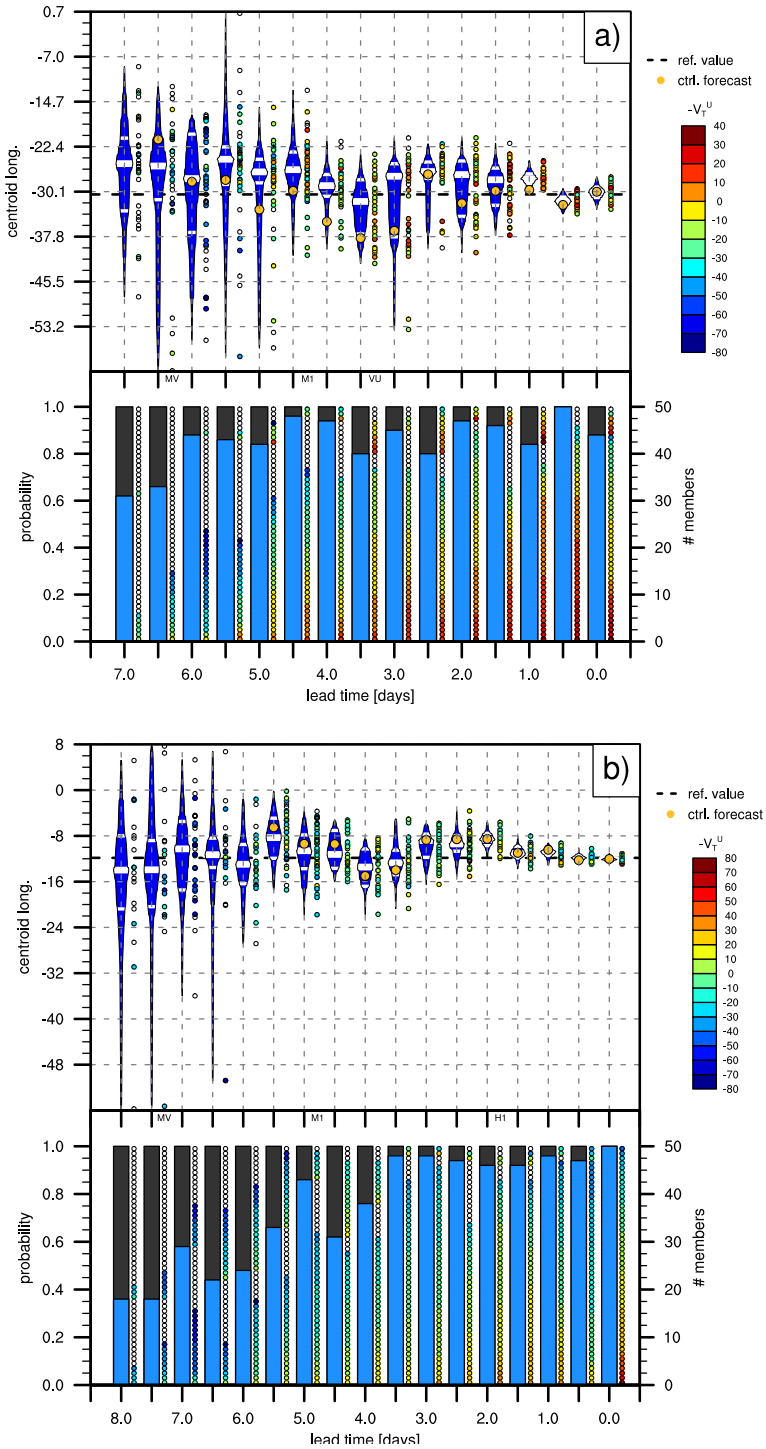

Figure 6.8: *[FC = forecast, MB = member only for this caption] As in Figure 6.2, but for different FC metrics related to RW objects:* (a) *RW packet (centroid) longitude at 0000 UTC on November 5, 2014 for Qendresa;* (b) *as* (a) *but at 0000 UTC on November 6. Note that the 0-day FC is shown here, unlike in previous figures, since FCs are evaluated at a fixed time.*

*In each sub-figure, the box-percentile plot at the top shows the FC distributions of MBs having the RW object (hereafter RW MBs), while the bar chart at the bottom shows the occurrence probability of the object, i.e. the fraction of RW MBs. Circles are additionally shown next to FC distributions and bars, each circle corresponding to a MB; storm MB circles are colored according to the $-V_T^U$ value, no-storm MB circles are white; in bar charts, circles are stacked in descending $-V_T^U$ order next to the blue (RW MBs) and grey (no-RW MBs) sections of each bar. Tags appearing above each bar denote statistical significance of the distributions of: no-storm MBs among all MBs (**MV** → no-storm MBs tend to have no RW object); $-V_T^U$ values among all MBs (**VU** → no-RW MBs have a lower average $-V_T^U$ value than RW MBs); no-storm MBs among RW MBs (**M1** and **M2** → the y-values of no-storm MBs have a significantly different average or lower standard deviation, respectively, than a random resampling); high-$-V_T^U$ (upper-tercile warmer-core) MBs among RW MBs (**H1** and **H2**, as **M1** and **M2**).*

higher sensitivity of RW packet existence to envelope values when these are close to the threshold. The first effect likely prevails on the second one, as the RW packet identification method was proved to be sufficiently robust and have little sensitivity to the chosen parameters within sensible ranges. A similar evolution to that shown in Figure 6.8b is seen in most cases and for most forecast metrics.

Figures 6.8a and 6.8b also show an almost complete lack of any statistically significant linkage between the occurrence and features of the RW packet and the occurrence and thermal structure of the cyclone, as indicated by the few "significance tags" that appear in both figures. The only, extremely weak exceptions are in these cases: a tendency for members without a RW packet (hereafter "no-RW packet members") to also have no cyclone and vice versa ("MV" tag), for the 6.5-day forecast in Figure 6.8a and the 7.5-day forecast in Figure 6.8b; a tendency for no-storm members to have a RW packet further eastward than it would be if they were randomly sampled from the forecast distribution ("M1" tag), for the 4.5-day forecast in Figure 6.8a. Other significance tags appearing in Figures 6.8a and 6.8b (whose meaning is explained in detail in the caption) are to be taken *cum grano salis*, due to the low corresponding forecast spread or number of no-RW packet members. A lack of statistically significant linkages between RW packet and RW breaking and cyclone occurrence and thermal structure is observed for almost all cases and all forecast metrics (see below for a discussion of this finding as well as a few minor exceptions, shown in Figure 6.9).

Forecast evolution is not always as smooth as observed in Figures 6.8a and 6.8b: an example of less gradual evolution can be seen in Figures 6.9a and 6.9b, showing respectively forecasts of RW packet distance at 1200 UTC on October 24, 2016 for Trixie and RW breaking latitude at 0000 UTC on November 5, 2011 for Rolf. In Figure 6.9a, RW packet occurrence probability jumps from 25% to nearly 80% between the 3.5-day and 3.0-day forecasts and from 90% to less than 40% between the 12-hour and the 0-hour forecasts. At this time, the RW packet was located over the eastern Atlantic and was about to dissipate one day later: while the first forecast jump is due to a sharp increase in RW packet occurrence probability, the second jump is due to an increased sensitivity of RW packet detection to the envelope threshold used (not shown)[1]. It is worth noting that no-storm members tend to have a closer RW packet to the cyclone than storm members in this case, with most lower outliers of forecast distributions being no-storm members; however, this is statistically significant only for the 1-day and

[1]While such undesirable circumstance is seen in a non-zero number of situations, their overall frequency is sufficiently low to not affect significantly the quality and reliability of results.

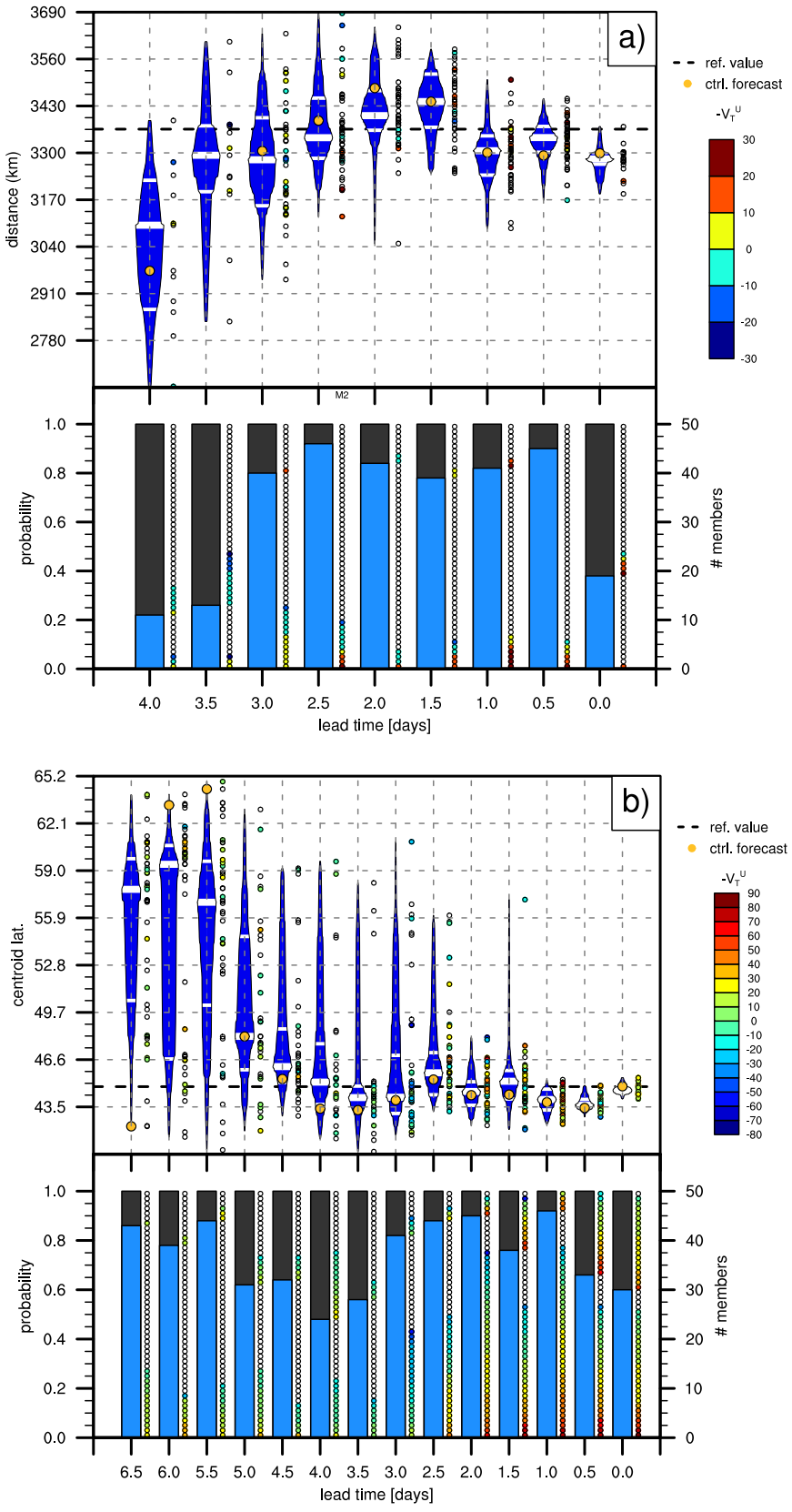

Figure 6.9: *As in Figure 6.8, but for:* (a) *distance of the RW packet from the cyclone at 1200 UTC on October 24, 2016 for Trixie;* (b) *RW breaking object latitude at 0000 UTC on November 5, 2011 for Rolf.*

2.5-day forecasts. This tendency may be interpreted in terms of members having the RW packet further downstream lacking the necessary timing as well as the dynamical conditions for cyclone development.

A non-gradual evolution of forecasts is also observed for RW breaking forecasts in some cases, one of which is evidenced in Figure 6.9b: in this case, the RW breaking object is predicted to occur much further north in early forecasts (LTs longer than 5 days), with a high ensemble spread which then decreases sharply to a much lower value; RW breaking occurrence probability also oscillates markedly between 80% or more (LTs longer than 5 days and between 3 days and 1 day) and 60% or less (LTs between 5 and 3 days and shorter than 1 day). This case exhibits relatively low predictability also because of the rapid evolution of the RW breaking object (not shown), which moved southward as the upper-level trough developed into a cut-off and dissipated one day later.

Stronger, statistically significant indications that the occurrence or features of a RW packet or RW breaking object be causally linked to the occurrence or thermal structure of the cyclone are only sporadically seen for some forecasts in some cases, an example of which is displayed in Figures 6.10 and 6.11.

Forecasts of the area and closest distance of the RW breaking object at 1200 UTC on November 13, 2017 for storm Numa are respectively shown in Figures 6.10a and 6.10b. A tendency for no-storm members to have a low RW breaking area is seen for most forecasts (Figure 6.10a), though it is only statistically significant for LTs between 3 and 2 days; the 2-day forecast also exhibits a propensity for high-—V_T^U (warmer-core) members to have a large RW breaking area. A similar tendency can be observed in Figure 6.10b for RW breaking closest distance, with no-storm members having a small distance; the 2-day forecast exhibits a similar pattern as for RW breaking area, with high-—V_T^U (warmer-core) members having a large distance. This behavior may be interpreted as follows: the occurrence of RW breaking over a sufficiently large region at the right place and time[2] constitutes a quasi-necessary dynamical precursor to the development of an upper-level cut-off trough, which then promotes cyclogenesis and (in some cases, see also Subsection 6.2.2) Medicane development. It is worth pointing out the large jump between the 1.5-day forecast and both the previous and next forecasts: in this case, such dip in RW breaking occurrence probability is to be attributed to a

[2]A smaller RW breaking closest distance is associated with a displaced or more rapidly evolving RW breaking object, as verified by examining the temporal and spatial distribution of predicted RW breaking objects (not shown).

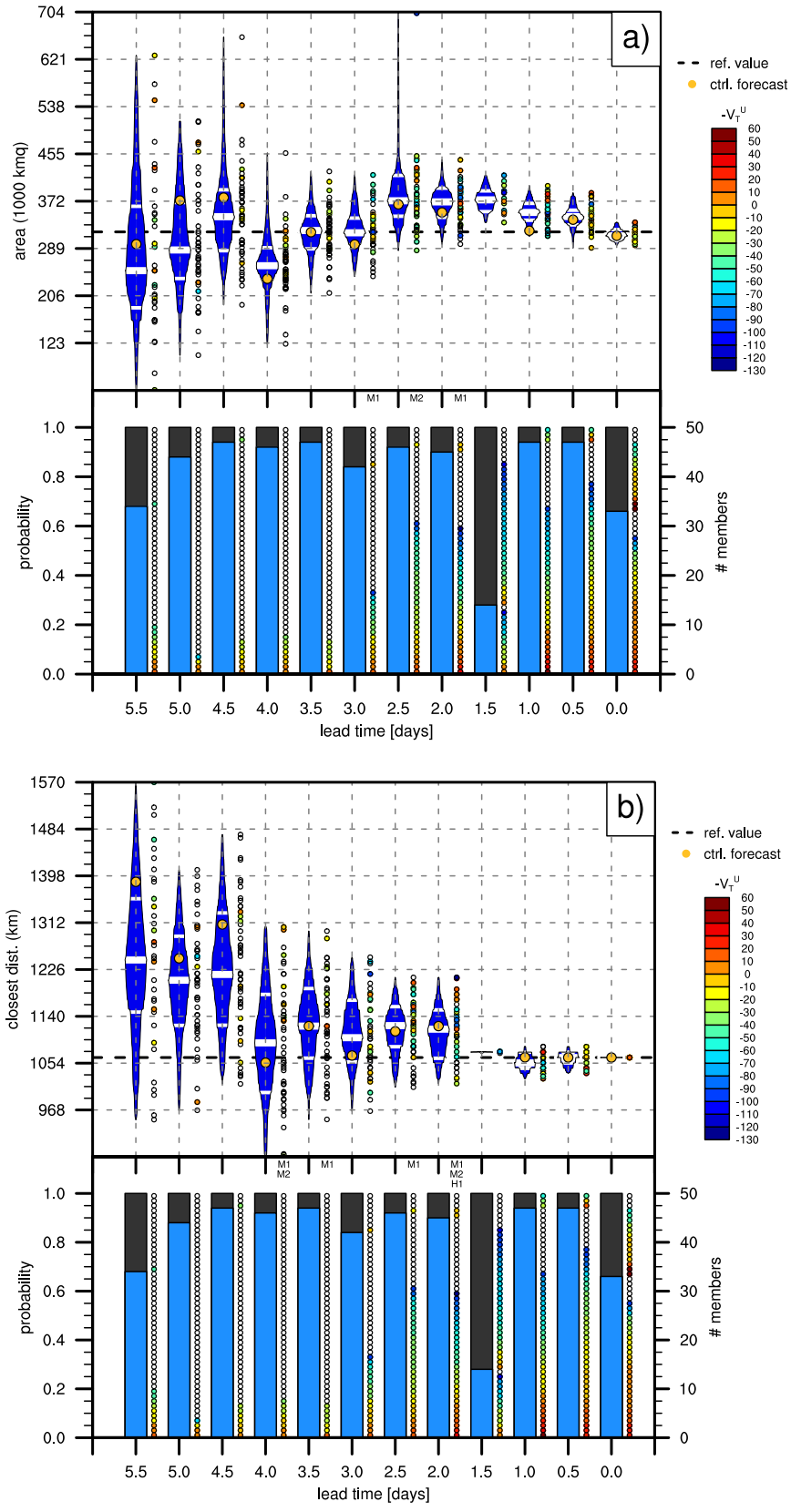

Figure 6.10: *As in Figure 6.8, but for:* (a) *area of the RW breaking object at 1200 UTC on November 13, 2017 for Numa;* (b) *closest distance between the RW breaking object and the cyclone at 1200 UTC on November 13, 2017 for Numa.*

highly variable shape of the PV trough, which caused the reversal of the PV gradient to be present only in some members, such that no RW breaking is identified in the others.

A slightly different behavior can be observed in Figure 6.11a, which shows forecasts of RW breaking closest distance at 0000 UTC on November 15, 2013 for storm Ruven. In this case, RW breaking occurrence probability remains relatively steady with decreasing LT, but two regimes can be identified: for early forecasts (3 days or longer LTs) ensemble spread is large and very few members have both RW breaking and the cyclone; for late forecasts, starting at 2.5 days LT, ensemble spread sharply decreases (with a brief dip in RW breaking occurrence probability) and number of storm members rapidly increases – this is the forecast jump that was already discussed in Subsection 6.1.3. As a similar evolution is also seen for other RW-related forecast metrics in this case (not shown), this suggests that cyclone predictability increases once RW breaking uncertainty is reduced. It should be noted that such behavior is not observed in other cases, confirming the high case-to-case variability among the eight Medicane events.

Finally, another example of statistically significant, albeit weak, linkages can be seen in Figure 6.11b, showing forecasts of RW packet area at 1200 UTC on November 12, 2017 for storm Numa. While early forecasts (LTs larger than 2 days) exhibit a large ensemble spread and have very few members with both the RW packet and the cyclone, later forecasts show a tendency for no-storm members to have low RW packet areas. This behavior is accompanied by a decrease in ensemble spread and a parallel increase in the number of storm members between 2.5 and 1.5 days LT, hence hinting at a dynamical linkage between RW packet position and features and cyclone occurrence.

In summary, the analysis of RW packet and RW breaking forecasts for all Medicane events indicates that these dynamical processes are predictable many days in advance (up to 10 days for RW packets, 8 days for RW breaking) and forecast consistency is far higher than that of cyclone-related forecasts. This is to be expected, given that RW packets and RW breaking are situated at the upper end of the multiscale cascade of phenomena leading to Medicane development and planetary-scale and synoptic-scale processes are typically more predictable than mesoscale ones (Kalnay 2003). Nevertheless, a non-gradual evolution of forecasts of RW-related metrics is observed in some cases and for some forecast times, mostly for RW packets and RW breaking objects that have recently formed or are soon to dissipate. Even though RW packets and RW breaking are found to be the dynamical precursors of all Medicane events analyzed in this thesis, ensemble forecasts rarely contain statistically robust indications of any linkage between the occurrence and features of the RW packet and RW breaking

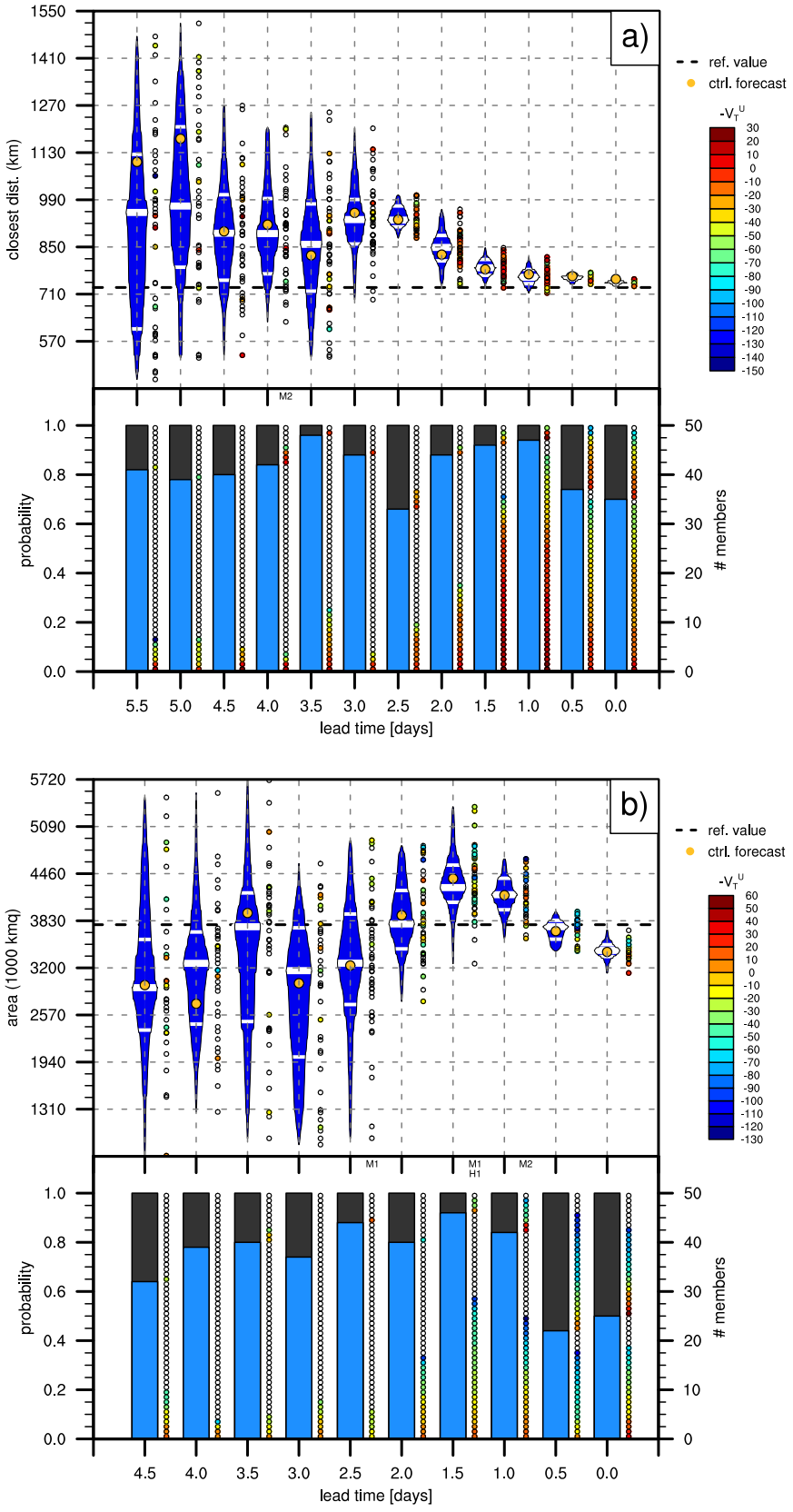

Figure 6.11: *As in Figure 6.8, but for:* (a) *closest distance between the RW breaking object and the cyclone at 0000 UTC on November 15, 2013 for Ruven;* (b) *area of the RW packet at 1200 UTC on November 12, 2017 for Numa.*

and those of the cyclone. In other words, it appears as though RW packets and RW breaking are necessary, but not sufficient ingredients for Medicane development. In the next subsection, the focus will shift onto the next-smaller dynamical precursor of Medicanes: the upper-level trough.

6.2.2 Precursor upper-level trough

The pathway leading to Medicane development was introduced in Subsection 2.5.1 and an upper-level trough was presented as one of the necessary synoptic-scale processes for instability to arise and cyclogenesis to ensue. As the eight cases were presented in Chapter 5, a large case-to-case variability emerged in terms of the structure, intensity and duration of the upper-level trough, ranging from cases with an intense cut-off maintaining good vertical alignment with the surface cyclone throughout its lifetime, to cases with a weak trough and no cut-off. In this subsection, the predictability of the upper-level trough is examined as well as its influence on the occurrence and thermal structure of the cyclone.

The influence of the intensity and position of the upper-level trough on cyclone occurrence is examined by using storm vs no-storm member composites (hereafter referred to as occurrence composites for brevity); 300 hPa GPH is chosen to represent the upper-level trough. For each case, an early forecast is chosen with a similar number of storm and no-storm members (each should be no lower than 20), while the composite time is chosen among all forecast times as the one with the clearest signal (the dependency of composites on this choice is discussed in detail below for each case). The average 300 hPa GPH value of no-storm members is then subtracted from that of storm members, and the difference is normalized by dividing by the ensemble standard deviation. This way ensemble variability is taken into account and statistically significant grid points (which are identified via a bootstrap method with 10 000 iterations, see Section 4.8) stand out more. The occurrence composites for all cases are shown in Figure 6.12.

The most striking similarity between all eight cases emerging from Figure 6.12 is the presence of a statistically significant negative difference (SSND) region in the vicinity of the cyclone: that is, a region where storm members have significantly lower GPH (i.e. a deeper trough in most cases) than no-storm members. This indicates that the presence of an upper-level trough is instrumental in enhancing air-sea instability and thus promoting cyclogenesis. This signal is sufficiently robust, as it is also found

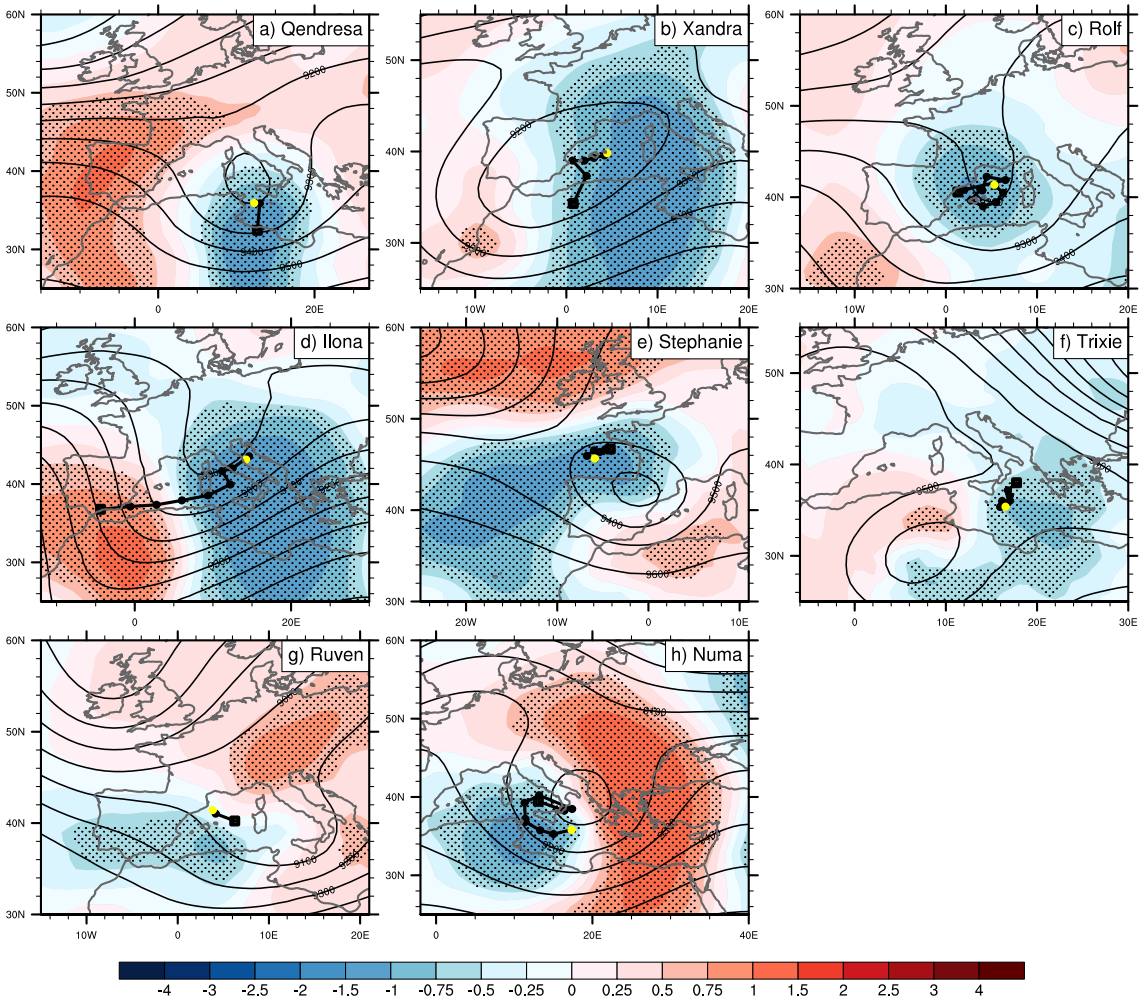

Figure 6.12: *Storm members vs no-storm members composites for all cases:* (a) *Qendresa, initialization time 0000 UTC on October 30, 2014, forecast time 0000 UTC on November 7, 2014;* (b) *Xandra, init. time 1200 UTC on November 23, 2014, fc. time 1200 UTC on December 1, 2014;* (c) *Rolf, init. time 0000 UTC on October 31, 2011, fc. time 0000 UTC on November 8, 2011;* (d) *Ilona, init. time 1200 UTC on January 14, 2014, fc. time 1200 UTC on January 21, 2014;* (e) *Stephanie, init. time 0000 UTC on September 10, 2016, fc. time 0000 UTC on September 15, 2016;* (f) *Trixie, init. time 0000 UTC on October 27, 2016, fc. time 0000 UTC on October 30, 2016;* (g) *Ruven, init. time 0000 UTC on November 13, 2013, fc. time 0000 UTC on November 19, 2013;* (h) *Numa, init. time 1200 UTC on November 10, 2017, fc. time 1200 UTC on November 16, 2017. Shading: 300 hPa GPH difference between the average of storm members and that of no-storm members, divided by the ensemble standard deviation; stippling shows statistically significant grid points at the 95% confidence level; contours: ensemble mean of 300 hPa GPH (m); the black line is the reference track, the first point represented by a square, the other points by a circle, the last point (corresponding to the fc. time for each case) is yellow.*

for neighboring forecasts and slightly different forecast times[3]; it was also verified that most forecast tracks are actually found within the SSND region at the composite time.

[3]For Trixie a much later forecast had to be chosen with respect to other cases, as early forecasts have few storm members (see also Subsection 6.1.2).

The eight cases can then be sorted into three groups, depending on their composite patterns as well as the ensemble average and the observed large-scale flow (see Chapter 5). Storms Qendresa and Xandra (Figures 6.12a and 6.12b) exhibit the strongest upper-level cut-off trough, which also remains vertically aligned with the cyclone for the longest time: in these two cases, the SSND region is found for the longest time (i.e. for the most composite times if a different one is chosen to compute the occurrence composites) and essentially follows the reference cyclone track, suggesting that for Qendresa and Xandra the upper-level cut-off was crucial for both the development and maintenance of the cyclone.

Another group includes storms Rolf, Ilona, Stephanie and Trixie (Figures 6.12c, 6.12d, 6.12e and 6.12f, respectively), for which the highest SSND is found during the mature stage of the cyclone, while a weaker or even no SSND is seen at the time of cyclone development (not shown). This suggests that in these cases, a stronger upper-level trough is tightly linked to cyclone maintenance, while being unimportant for cyclone development. In fact, for Rolf, Stephanie and Trixie, all ensemble members have a pronounced trough at the time the cyclone forms, such that a stronger trough is not associated with (i.e. does not result in) a higher probability of cyclone formation; conversely, ensemble variability is much higher at the composite time – during the mature stage – such that a stronger trough (or even, for Trixie, an existing trough) can play a more important role and is therefore associated with a higher probability of cyclone maintenance (i.e. a longer cyclone lifetime). Ilona is different from the other three cases, in that only a weak trough was present at the time the cyclone formed (see Subsection 5.1.3) and the storm rapidly crossed the western Mediterranean: the pattern in Figure 6.12d suggests that in this case, a deeper trough may contribute to maintain the cyclone for longer; in fact, many members with a weaker trough also have a shorter-lived cyclone (not shown).

A last group includes storms Ruven and Numa (Figures 6.12g and 6.12h, respectively), for which the highest SSND is found during the cyclone's early stage, while a weaker or even no SSND is seen during the mature stage (not shown). The pattern in Figures 6.12g and 6.12h suggests that storm members have an upper-level trough located further upstream (i.e. west) with respect to no-storm members, resulting in a better vertical alignment with the surface cyclone (this remains true when forecast cyclone tracks are considered, as most of them develop in the vicinity of the SSND region – not shown), which in turn decreases VWS and promotes cyclogenesis. For Ruven, no SSND region is found at a later composite time (not shown), as ensemble

variability is low and most members have no longer an upper-level trough. For Numa, which unlike Ruven was a long-lived cyclone, a weak SSND region is found during the cyclone's mature stage, while ensemble variability is small and most members have only a very weak upper-level trough: this suggests that the trough plays a little role in cyclone maintenance in this case.

The influence of the upper-level trough on cyclone thermal structure is examined by using $-V_T^U$-based composites, hereafter referred to as structure composites for brevity, which are computed as follows. Storm members are sorted according to their $-V_T^U$ value and subsequently divided into three terciles; the members belonging to the highest/lowest tercile will be referred to as warm/cold-core members hereafter. The upper-level trough is once again represented by 300 hPa GPH. For each case, a suitable forecast is selected with a sufficiently high ensemble spread of $-V_T^U$ and at least 30 storm members[4], while the composite time is selected among all forecast times during the cyclone's mature stage as the one with the clearest signal (the dependency of composites on this choice is discussed in detail below). The average 300 hPa GPH value of cold-core members is then subtracted from that of warm-core members, and the difference is normalized by dividing by the ensemble standard deviation as was done for occurrence composites. A cyclone-centered (Lagrangian) frame of reference is chosen for structure composites, which are shown for all cases in Figure 6.13.

A much larger case-to-case variability is observed for structure composites than for occurrence composites. The eight cases can be first sorted into three groups depending on the prevailing sign of the composite difference, i.e. whether warm-core members have a lower or higher GPH (corresponding to a stronger or weaker upper-level trough) than cold-core members. The first group includes storms Qendresa, Xandra, Ruven and Ilona (Figures 6.13a, 6.13b, 6.13c and 6.13d, respectively). In these cases, a SSND prevails in the vicinity of the cyclone center, hinting at a linkage between a stronger upper-level trough and a warmer core of the cyclone and therefore a marked influence of the synoptic-scale dynamics on the cyclone's thermal structure. However, the intensity of this pattern is highly variable within this group, with Qendresa having the strongest signal and Ilona having the weakest (albeit with a small region of SSND close to the cyclone center). The second group includes storms Stephanie and Trixie (Figures 6.13e and 6.13f, respectively), for which a dipole pattern is found. The third

[4]This value is chosen to have a tercile size of at least 10 members, in an effort to maximize statistical significance of composites; the results obtained are insensitive to little variations of this value. The forecast is also chosen so as to guarantee that all warm-core members have positive $-V_T^U$ values and all cold-core ones have large negative $-V_T^U$ values.

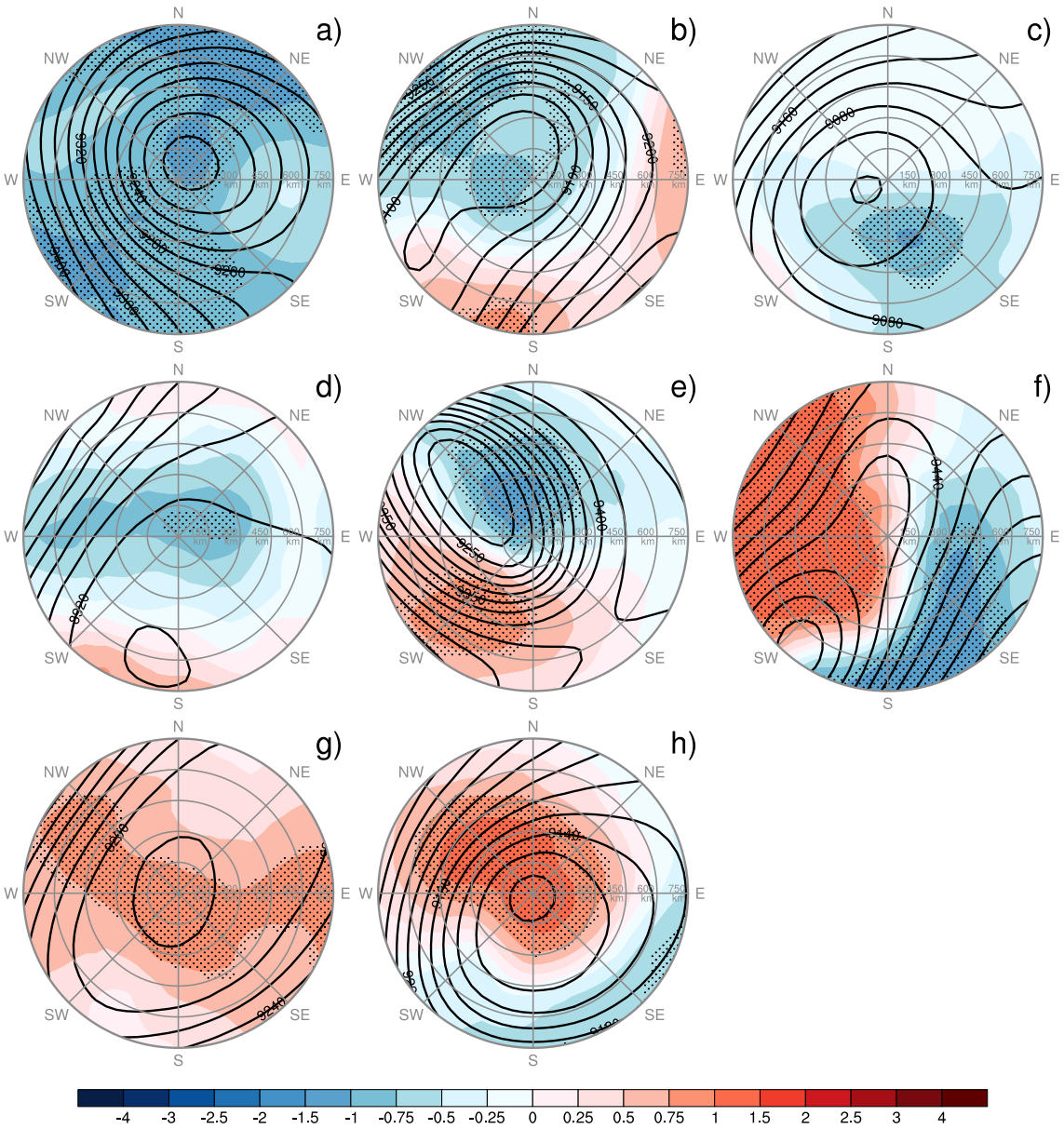

Figure 6.13: *High-—V_T^U (warmer-core, upper tercile) vs low-—V_T^U (colder-core, lower tercile) cyclone-relative (Lagrangian) composites for all cases:* (a) *Qendresa, initialization time 1200 UTC on November 3, 2014, forecast time 1200 UTC on November 8, 2014;* (b) *Xandra, init. time 0000 UTC on November 29, 2014, fc. time 1800 UTC on November 30, 2014;* (c) *Ruven, init. time 0000 UTC on November 14, 2013, fc. time 1800 UTC on November 18, 2013;* (d) *Ilona, init. time 1200 UTC on January 18, 2014, fc. time 0000 UTC on January 21, 2014;* (e) *Stephanie, init. time 0000 UTC on September 13, 2016, fc. time 1800 UTC on September 14, 2016;* (f) *Trixie, init. time 0000 UTC on October 28, 2016, fc. time 1800 UTC on October 29, 2016;* (g) *Rolf, init. time 0000 UTC on November 3, 2011, fc. time 0600 UTC on November 8, 2011;* (h) *Numa, init. time 0000 UTC on November 14, 2017, fc. time 0600 UTC on November 17, 2017. Shading, stippling and contours as in Figure 6.12.*

group includes storms Rolf and Numa (Figures 6.13g and 6.13h, respectively), for which a statistically significant positive difference (SSPD) is found in the vicinity of the cyclone center, revealing an association between a weaker upper-level trough and a warm-core cyclone; this indicates that other factors (e.g. convective processes, surface fluxes) play a larger role than the upper-level trough in promoting the development of a warm core in these cases.

A clearer picture emerges if the ensemble average GPH (shown as contours in Figure 6.13) is considered along with the composite difference. In most cases, almost all members exhibit a strong upper-level cut-off trough which is comparatively well aligned with the cyclone[5], the only exceptions being Ruven and Ilona (Figures 6.13c and 6.13d), for which only a weak cut-off is predicted (as well as observed). The SSND found for Qendresa, Xandra, Ruven and Ilona can then be interpreted in terms of a deeper cut-off being instrumental for the development of a warm core due to increased air-sea instability. The dipole pattern observed for Stephanie and Trixie suggests that a better vertical alignment is the necessary ingredient for warm core development in these cases, most likely due to reduced VWS, which is typically associated with TT events (Davis and Bosart 2003; Hulme and Martin 2009a): this is consistent with Stephanie exhibiting a higher VWS than other cases (Subsection 5.1.6) and Trixie spending its mature stage in a region of higher VWS a few hundred km downstream of the upper-level trough, after losing its vertical alignment with the trough (Subsection 5.1.7). Finally, even though Rolf and Numa exhibit a SSPD region in the vicinity of the cyclone center, a strong upper-level cut-off trough is still predicted by most members to be very well aligned with the cyclone (Figures 6.13g and 6.13h). The combined presence of the cut-off and the SSPD region suggests that the upper-level trough still plays a role in promoting warm core development, though other factors, such as surface fluxes and/or latent heat release through convection, have a larger effect in these cases. This is consistent with previous findings of both 1) a strong influence of surface fluxes on Medicane evolution (e.g. Tous et al. 2013) and 2) a high dependency on the case of the importance of air-sea interaction (Miglietta and Rotunno 2019).

Another interpretation of the SSPD that is seen in structure composites for Rolf and Numa can be given as follows. These storms are the longest-lived among the eight

[5]Such vertical alignment is maintained in all cases for most of the mature stage of the cyclone, although the strength of the upper-level trough decreases with time. Structure composites are relatively insensitive to a small variation of the composite time, though the difference pattern rotates around the cyclone center in some cases, with its maxima and minima shifting as the cyclone evolves; the nature of the patterns found is preserved throughout the mature stage.

Medicanes and exhibit a similar evolution in terms of thermal structure, as can be seen comparing Figures 5.4 and 5.31, with a slow but steady warm core development. Rolf and Numa, unlike other Medicanes, had a prolonged permanence over the sea and also maintained a nearly perfect vertical alignment with the upper-level cut-off until their late stage. This is likely to have allowed air-sea instability to occur for a sufficiently long time that by the time warm core magnitude peaked, the upper-level trough had been partially eroded by convection, which would explain why warm-core members have a weaker trough than cold-core members in structure composites. This hypothesis is supported by evidence of deep convection occurring for at least 48 hours for storm Rolf (Dafis et al. 2018).

6.3 Considerations on case-to-case variability

The analysis of the dynamics and predictability of the eight Medicane events carried out so far has revealed a very high case-to-case variability. This confirms that the "Medicane" tag actually corresponds to a broad category of Mediterranean cyclones, including both explosively and slowly intensifying, short-lived and long-lived, weak and intense cyclones. On the other hand, despite this large variability, all eight storms exhibit a common development pathway, with a RW packet forming over the Atlantic, crossing the ocean and breaking over western Europe in association with an upper-level trough penetrating the Mediterranean region and usually, but not always, developing into a cut-off. The eight cases also exhibit common features, such as the development of an upper-level warm core, a marked contraction and symmetrization of the cyclone.

Nevertheless, the evolution pathway of the eight storms is highly variable. A glance back at Table 5.1 can shed further light on the mechanisms that are associated with such variability, having in mind the results presented in the previous two sections. From Table 5.1, it is apparent that the four longest-lived Medicanes (namely, Rolf, Xandra, Trixie and Numa) are also the ones that reached the highest upper-level warm core magnitude (this holds true also if a slightly different radius is used to compute $-V_T^U$). This can be interpreted in terms of long-lived Medicanes having a longer time available for air-sea instability to reach a steady state and promote warm core development. Storm Qendresa constitutes a peculiar case – at least within the eight analyzed in this thesis – as it underwent explosive intensification and shrank to a extremely small size, such that the calculation of $-V_T^U$ is most sensitive to the chosen radius in this case and a higher value is attained if a smaller radius is used; however, Qendresa's peak value of

$-V_T^U$ does not exceed that of the four longest-lived Medicanes even if a much smaller radius is used, and the storm attained an upper-level warm core for a mere 12 hours.

At the opposite extreme of this spectrum are Ruven and Ilona, both of which evolved very rapidly, crossing the western Mediterranean and the Tyrrhenian Sea and considerably interacting with Mediterranean orography along their path. Both Ruven and Ilona had no upper-level cut-off trough throughout their existence, which is likely to have played an important role in their failure to attain a deeper, longer-lived upper-level warm core.

The results of this thesis are summarized and discussed in the context of existing literature in the next chapter, which also provides an outlook on further research paths.

Chapter 7

Summary and outlook

Medicanes have been gaining increasing attention in the research community in the last two decades. These storms constitute a major threat in the Mediterranean region as they are associated with intense winds, abundant to extreme rainfall and flooding. Medicanes remain to this day elusive characters of the Mediterranean climate in that they occur infrequently and in regions where observations are scarce; moreover, a unanimous, objective definition is still missing, which has hindered the implementation of an objective early warning procedure based on operational forecasts. Although the evolution pathway of Medicanes is known, our understanding of their development, intensification and maintenance is still partial, as the prevailing mechanisms vary considerably from case to case and a coherent, general picture is still missing. For these reasons, predicting Medicanes poses a considerable challenge for operational forecasts, also due to the complex interplay between the numerous factors influencing their evolution at multiple spatial and temporal scales.

The overarching goal of this thesis was to assess the predictability of Medicanes through the evaluation of ECMWF operational ensemble forecasts. For this purpose, a systematic investigation of seven recent (2011–2017) Medicanes and a 2016 tropical-like storm which occurred over the Bay of Biscay was carried out through an object-based approach. The eight events were first examined using ECMWF operational analysis data and characterized by using suitable storm-relative parameters; in addition, the antecedent large-scale dynamics of these events was also examined. Focus was then given to the overall predictability of the eight cases and the evolution of forecast uncertainty and variability with lead time. Finally, an assessment was carried out of the predictability of precursor large-dynamics and its impact on the development and thermal structure of the eight events.

The examination of the eight Medicane events and their antecedent large-scale dynamics is illustrated in Chapter 5. Referring to the corresponding research questions enumerated in Chapter 3, the findings of this part can be summarized as follows:

RQ 1 Medicanes fit into the TT paradigm, though two major distinctions need to be made, as explained below.

RQ 1a Medicanes develop in a highly similar large-scale environment to North Atlantic TT cases. Specifically, an upper-level trough always precedes the formation of the cyclone, while the trough often, but not always, develops into a cut-off which reaches nearly perfect vertical alignment with the cyclone in some cases. The presence of cold air aloft has the effect of destabilizing the atmosphere, promoting air-sea instability while decreasing vertical wind shear, as also observed for North Atlantic TT cases (Davis and Bosart 2003, 2004; Hulme and Martin 2009a). However, the Mediterranean Sea lacks vast expanses of uninterrupted open waters and its complex orography often interacts strongly with Medicanes, as is also seen for four of the eight cases considered in this thesis. This, together with the relatively low SST of the Mediterranean Sea compared to the subtropical Atlantic, causes Medicanes to be often short-lived and hardly ever reach hurricane intensity.

RQ 1b The analysis of the eight events confirms the high case-to-case variability of Medicanes (Fita and Flaounas 2018; Miglietta and Rotunno 2019) and reveals a high sensitivity of CPS parameters to the computing radius as well as a slight positive MSLP bias of ECMWF analysis data. However, common features are found between all cases in addition to the (often short-lived) development of a warm core, such as a marked contraction and symmetrization of the cyclone prior to its mature stage. This suggests that a better categorization of Medicanes in terms of symmetry, compactness and upper-level thermal wind is desirable.

The investigation of the overall predictability of the eight Medicane events is illustrated in Section 6.1. The main findings are summarized as follows:

RQ 2 Medicanes are successfully reproduced in ECMWF ensemble forecasts, as discussed below in further detail.

RQ 2a An analysis of the EFI and SOT indices for wind and wind gust forecasts reveals once again a high case-to-case variability, with only some cases exhibiting consistent forecasts and high index values, corresponding to extreme speeds. However, the tendency of high EFI and SOT values to increase further with decreasing LT and the considerably high values reached in some cases reveal that a fraction of Medicanes can be indeed considered to be extreme with respect to model climatology.

RQ 2b No systematic errors were found for ensemble forecasts. The general convergence of forecasts towards the analysis, with an associated reduction of spread with decreasing LT, and the forecast distribution tail reaching or exceeding the analysis value even at long LTs indicate that the ECMWF model is capable of reproducing Medicanes in their salient features. However, a significant underestimation of storm intensity (1–5 hPa) was found in analysis data for all cases where observational and/or high-resolution modeling data were available, most likely owing to the ECMWF model's relatively low resolution and parameterized convection. Despite this, the evolution, trajectory and structure of all events was found to be highly similar to that derived from analysis data.

RQ 2c The occurrence of a cyclone is generally well forecast, with higher probability than 50% at 7 days LT. In most cases, however, at long LTs only the tails of the forecast distribution reach the high values of symmetry, compactness and upper-level thermal wind found in the analysis, hinting at an intrinsically low probability of the cyclone exhibiting Medicane traits. Such probability tends to increase with decreasing LT in all cases, but does not exceed 50% earlier than 2 days in advance.

In Section 6.1, forecast uncertainty was given special attention, in particular as concerns its evolution with LT, obtaining the following findings:

RQ 3 Uncertainty is characterized through *ad-hoc*, tailored representation choices depending on the quantity.

RQ 3a For most variables, box-percentile plots were preferred to normal box-and-whisker plots in that they show the entire distribution of values. This is advantageous for representing ensemble forecasts, in that the assumption that all ensemble members be equally probable future states results in the distribution tails to be as important as its central values. Two-dimensional uncertainty was represented through an EOF-based visualization which proved effective in displaying the joint variability of two quantities for multiple forecasts – this is particularly suitable for cyclone position uncertainty, though it is also helpful to explore the linkages between two different aspects of the same forecasts.

RQ 3b The evolution of uncertainty with LT strongly depends on the quantity, being most gradual for CP and least gradual for cyclone thermal structure (i.e. upper-level thermal wind $-V_T^U$). A remarkable consistency was found for cyclone position uncertainty, which was interpreted in terms of some regions of the Mediterranean Sea being more conducive to Medicane development than others, mostly due to the overlap of large-scale and small-scale favorable environmental conditions, consistently with existing literature (Tous and Romero 2013; Cavicchia et al. 2014a). Conversely, forecast jumps are found in most cases for cyclone occurrence and structure forecasts, confirming the high sensitivity of Medicane forecasts to the initial conditions (Fita et al. 2007; Davolio et al. 2009; Cioni et al. 2016) and hinting at the existence of predictability barriers, which would be overcome only when the initial conditions adequately represent the variety of factors playing a role in Medicane development.

RQ 3c The largest uncertainty is found for upper-level thermal wind $-V_T^U$, indicating that whether the cyclone will develop an upper-level warm core or not is one of the least predictable aspects of Medicane forecasts, most likely due to the multitude of large-scale and small-scale processes (e.g. the upper-level trough and surface fluxes) playing a role in warm core development.

In Section 6.2, the focus shifted to the large-scale processes that are found to precede Medicane development, namely RW packets, RW breaking and upper-level troughs. This part of the study produced the following findings:

RQ 4 While a RW packet breaking over western Europe is observed for all cases, the occurrence and thermal structure of the cyclone appears to be more strongly linked to the occurrence, strength and position of the upper-level trough.

RQ 4a RW packets and RW breaking were found to be predictable respectively up to 10 and 8 days prior to cyclone formation; both these features exhibit a lower predictability shortly after their development or before their dissipation than during their mature stage, both in terms of occurrence probability and forecast consistency. Interestingly, ensemble forecasts do not indicate a significant linkage between the occurrence and features of the cyclone and those of both RW packets and RW breaking, with the exception of weak hints that the cyclone is less likely to develop if no RW breaking occurs in the previous 2–3 days. Since the occurrence of a RW packet and subsequent RW breaking are observed for all cases, it is concluded that these large-scale processes are a necessary, but not sufficient ingredient for Medicane development and that their primary role is to bring about a large-scale environment that is later conducive for cyclogenesis and air-sea instability.

RQ 4b The presence and intensity of the upper-level cut-off trough were found to be instrumental in determining cyclone occurrence, while their linkage to cyclone thermal structure is highly variable from case to case. Specifically, in six cases a stronger trough and/or a better vertical alignment with the surface cyclone is associated with a higher cyclone occurrence probability and a deeper warm core; conversely, in two cases warm core magnitude is negatively linked with trough depth, suggesting that other factors, such as surface fluxes and/or latent heat release through convection, may have a larger influence depending on the case, consistently with previous findings (e.g. Tous et al. 2013; Miglietta and Rotunno 2019).

While this thesis focused on the antecedent large-scale dynamics of Medicanes, it paves the way towards a more complete and in-depth investigation of the physical mechanisms underlying the findings summarized in this chapter. The large-scale

perspective is, in fact, but one fragment of the full picture, a vast mosaic of numerous processes interacting with each other at multiple temporal and spatial scales. The results obtained and presented in this thesis indicate that large-scale processes are responsible for setting the stage for the development of a Mediterranean cyclone which is then likely to follow the TT pathway and develop tropical traits. Given the sensitivity of Medicane forecasts to the initial conditions, however, small-scale processes such as surface fluxes (Fita et al. 2007; Tous et al. 2013; Miglietta et al. 2017) and local low-level convergence (Miglietta and Rotunno 2019) are most likely to be the culprits,i.e. the decisive factor determining the extent to which the cyclone attains tropical traits.

Nevertheless, Medicanes are by nature a multiscale phenomenon, such that surface fluxes and latent heat release are most effective when working in synergy with the upper-level trough (Carrió et al. 2017). The present work indeed highlighted the instrumental role played by the vertical alignment between the upper-level and surface lows. An effective means of building on the findings of this thesis would be to perform high-resolution, convection-permitting ensemble simulations of several Medicane events, introducing perturbations of the large-scale flow in order to quantify the influence of the upper-level trough and its interaction with local processes. An object-based approach similar to the one employed in the present work would help condense information in a meaningful fashion, thus tackling the challenge of analyzing vast amounts of data.

Finally, this thesis pointed out the large case-to-case variability between Medicane events, most importantly in terms of the influence of the upper-level trough on warm core development. This is consistent with the findings of Miglietta and Rotunno (2019), who remarked that the importance of air-sea interaction strongly depends on the case. A systematic analysis of all Medicanes that occurred in the last 50–60 years, possibly using high-resolution reanalysis data as soon as it becomes available, could shed further light on Medicane variability and attempt at sorting Medicane events into meaningful subcategories, in order to study the linkage of “Medicane flavors” to their predictability.

Symbols and abbreviations

Abbreviations

CP	central pressure
CPS	cyclone phase space
DTW	dynamic time warping
ECMWF	European Centre for Medium-Range Weather Forecasts
EDA	Ensemble Data Assimilation
EFI	Extreme Forecast Index
ENS	ensemble prediction system
EOF	Empirical Orthogonal Function
ETW	evaluation time window
GPH	geopotential height
HRES	high-resolution
LT	lead time
MSLP	mean sea level pressure
NCEP	National Centers for Environmental Prediction
NOAA	National Oceanic and Atmospheric Administration
PC	Principal Component
PDF	probability density function

PV potential vorticity

PVU potential vorticity unit

RQ research question

RW Rossby wave

SOT Shift Of Tails

SSND statistically significant negative difference

SSPD statistically significant positive difference

SST sea surface temperature

TC tropical cyclone

TLC tropical-like cyclone

TT tropical transition

UTC Universal Time Coordinate

VWS vertical wind shear

CPS parameters

B 925-700 hPa storm-relative thickness asymmetry

$-V_T^L$ lower-level (925-700 hPa) thermal wind

$-V_T^U$ upper-level (700-400 hPa) thermal wind

References

Akhtar, N., Brauch, J., Dobler, A., Béranger, K. and Ahrens, B. (2014) Medicanes in an ocean-atmosphere coupled regional climate model. *Natural Hazards and Earth System Sciences*, **14**, 2189–2201.

Baldwin, M. E. and Kain, J. S. (2006) Sensitivity of several performance measures to displacement error, bias, and event frequency. *Weather and Forecasting*, **21**, 636–648.

Bauer, P., Thorpe, A. and Brunet, G. (2015) The quiet revolution of numerical weather prediction. *Nature*, **525**, 47–55.

Bentley, A. M., Bosart, L. F. and Keyser, D. (2017) Upper-tropospheric precursors to the formation of subtropical cyclones that undergo tropical transition in the North Atlantic basin. *Monthly Weather Review*, **145**, 503–520.

Bentley, A. M., Keyser, D. and Bosart, L. F. (2016) A dynamically based climatology of subtropical cyclones that undergo tropical transition in the North Atlantic basin. *Monthly Weather Review*, **144**, 2049–2068.

Berndt, D. J. and Clifford, J. (1994) Using dynamic time warping to find patterns in time series. In *KDD workshop*, vol. 10, 359–370.

Berner, J., Achatz, U., Batté, L., Bengtsson, L., de la Cámara, A., Christensen, H. M., Colangeli, M., Coleman, D. R. B., Crommelin, D., Dolaptchiev, S. I., Franzke, C. L. E., Friederichs, P., Imkeller, P., Järvinen, H., Juricke, S., Kitsios, V., Lott, F., Lucarini, V., Mahajan, S., Palmer, T. N., Penland, C., Sakradzija, M., von Storch, J.-S., Weisheimer, A., Weniger, M., Williams, P. D. and Yano, J.-I. (2017) Stochastic parameterization: Toward a new view of weather and climate models. *Bulletin of the American Meteorological Society*, **98**, 565–588.

Billing, H., Haupt, I. and Tonn, W. (1983) Evolution of a hurricane-like cyclone in the Mediterranean Sea. *Beiträge zur Physik der Atmosphäre*, **56**, 508–510.

Bister, M. and Emanuel, K. A. (1998) Dissipative heating and hurricane intensity. *Meteorology and Atmospheric Physics*, **65**, 233–240.

Bohr, T., Jensen, M. H., Paladin, G. and Vulpiani, A. (2005) *Dynamical systems approach to turbulence*. Cambridge University Press.

Bosart, L. F. and Bartlo, J. A. (1991) Tropical storm formation in a baroclinic environment. *Monthly Weather Review*, **119**, 1979–2013.

Bracken, W. E. and Bosart, L. F. (2000) The role of synoptic-scale flow during tropical cyclogenesis over the North Atlantic Ocean. *Monthly Weather Review*, **128**, 353–376.

Bresch, J. F., Reed, R. J. and Albright, M. D. (1997) A polar-low development over the Bering Sea: Analysis, numerical simulation, and sensitivity experiments. *Monthly Weather Review*, **125**, 3109–3130.

Buizza, R. (1997) Potential forecast skill of ensemble prediction and spread and skill distributions of the ECMWF ensemble prediction system. *Monthly Weather Review*, **125**, 99–119.

— (2008) The value of probabilistic prediction. *Atmospheric Science Letters*, **9**, 36–42.

Buizza, R. and Hollingsworth, A. (2002) Storm prediction over Europe using the ECMWF ensemble prediction system. *Meteorological Applications*, **9**, 289–305.

Buizza, R. and Leutbecher, M. (2015) The forecast skill horizon. *Quarterly Journal of the Royal Meteorological Society*, **141**, 3366–3382.

Buizza, R., Leutbecher, M. and Isaksen, L. (2008) Potential use of an ensemble of analyses in the ECMWF Ensemble Prediction System. *Quarterly Journal of the Royal Meteorological Society*, **134**, 2051–2066.

Buizza, R. and Palmer, T. N. (1995) The singular-vector structure of the atmospheric global circulation. *Journal of the Atmospheric Sciences*, **52**, 1434–1456.

Businger, S. and Reed, R. J. (1989) Cyclogenesis in cold air masses. *Weather and Forecasting*, **4**, 133–156.

Buzzi, A. and Tibaldi, S. (1978) Cyclogenesis in the lee of the Alps: A case study. *Quarterly Journal of the Royal Meteorological Society*, **104**, 271–287.

Carrió, D. S., Homar, V., Jansá, A., Romero, R. and Picornell, M. A. (2017) Tropicalization process of the 7 November 2014 Mediterranean cyclone: Numerical sensitivity study. *Atmospheric Research*, **197**, 300–312.

Case, J. L., Manobianco, J., Lane, J. E., Immer, C. D. and Merceret, F. J. (2004) An objective technique for verifying sea breezes in high-resolution numerical weather prediction models. *Weather and Forecasting*, **19**, 690–705.

Cavicchia, L. and von Storch, H. (2012) The simulation of medicanes in a high-resolution regional climate model. *Climate dynamics*, **39**, 2273–2290.

Cavicchia, L., von Storch, H. and Gualdi, S. (2014a) A long-term climatology of medicanes. *Climate dynamics*, **43**, 1183–1195.

— (2014b) Mediterranean tropical-like cyclones in present and future climate. *Journal of Climate*, **27**, 7493–7501.

Chaboureau, J.-P., Nuissier, O. and Claud, C. (2012a) Verification of ensemble forecasts of Mediterranean high-impact weather events against satellite observations. *Natural Hazards and Earth System Sciences*, **12**, 2449–2462.

Chaboureau, J.-P., Pantillon, F. P., Lambert, D., Richard, E. and Claud, C. (2012b) Tropical transition of a Mediterranean storm by jet crossing. *Quarterly Journal of the Royal Meteorological Society*, **138**, 596–611.

Cioni, G., Cerrai, D. and Klocke, D. (2018) Investigating the predictability of a Mediterranean tropical-like cyclone using a storm-resolving model. *Quarterly Journal of the Royal Meteorological Society*, **144**, 1598–1610.

Cioni, G., Malguzzi, P. and Buzzi, A. (2016) Thermal structure and dynamical precursor of a Mediterranean tropical-like cyclone. *Quarterly Journal of the Royal Meteorological Society*, **142**, 1757–1766.

Claud, C., Alhammoud, B., Funatsu, B. M. and Chaboureau, J.-P. (2010) Mediterranean hurricanes: large-scale environment and convective and precipitating areas from satellite microwave observations. *Natural Hazards and Earth System Sciences*, **10**, 2199–2213.

Dafis, S., Rysman, J. F., Claud, C. and Flaounas, E. (2018) Remote sensing of deep convection within a tropical-like cyclone over the Mediterranean Sea. *Atmospheric Science Letters*, **19**, e823.

Davis, C. A. (2010) Simulations of subtropical cyclones in a baroclinic channel model. *Journal of the Atmospheric Sciences*, **67**, 2871–2892.

Davis, C. A. and Bosart, L. F. (2003) Baroclinically induced tropical cyclogenesis. *Monthly Weather Review*, **131**, 2730–2747.

— (2004) The TT problem: Forecasting the tropical transition of cyclones. *Bulletin of the American Meteorological Society*, **85**, 1657–1662.

Davis, C. A., Brown, B. and Bullock, R. (2006a) Object-based verification of precipitation forecasts. Part I: Methodology and application to mesoscale rain areas. *Monthly Weather Review*, **134**, 1772–1784.

— (2006b) Object-based verification of precipitation forecasts. Part II: Application to convective rain systems. *Monthly Weather Review*, **134**, 1785–1795.

Davis, C. A., Brown, B. G., Bullock, R. and Halley-Gotway, J. (2009) The method for object-based diagnostic evaluation (MODE) applied to numerical forecasts from the 2005 NSSL/SPC Spring Program. *Weather and Forecasting*, **24**, 1252–1267.

Davolio, S., Miglietta, M. M., Moscatello, A., Pacifico, F., Buzzi, A. and Rotunno, R. (2009) Numerical forecast and analysis of a tropical-like cyclone in the Ionian Sea. *Natural Hazards and Earth System Sciences*, **9**, 551–562.

De Zolt, S., Lionello, P., Nuhu, A. and Tomasin, A. (2006) The disastrous storm of 4 November 1966 on Italy. *Natural Hazards and Earth System Sciences*, **6**, 861–879.

DelSole, T. (2004) Predictability and information theory. Part I: Measures of predictability. *Journal of the Atmospheric Sciences*, **61**, 2425–2440.

DeMaria, M., Knaff, J. A. and Connell, B. H. (2001) A tropical cyclone genesis parameter for the tropical Atlantic. *Weather and Forecasting*, **16**, 219–233.

Di Muzio, E., Riemer, M., Fink, A. H. and Maier-Gerber, M. (2019) Assessing the predictability of Medicanes in ECMWF ensemble forecasts using an object-based approach. *Quarterly Journal of the Royal Meteorological Society*, **145**, 1202–1217.

Diaconescu, E. P. and Laprise, R. (2012) Singular vectors in atmospheric sciences: A review. *Earth-Science Reviews*, **113**, 161–175.

Ebert, E. E. and Gallus Jr., W. A. (2009) Toward better understanding of the contiguous rain area (CRA) method for spatial forecast verification. *Weather and Forecasting*, **24**, 1401–1415.

Ebert, E. E. and McBride, J. L. (2000) Verification of precipitation in weather systems: Determination of systematic errors. *Journal of Hydrology*, **239**, 179–202.

Emanuel, K. A. (1986) An air-sea interaction theory for tropical cyclones. Part I: Steady-state maintenance. *Journal of the Atmospheric Sciences*, **43**, 585–605.

— (2005) Genesis and maintenance of "Mediterranean hurricanes". *Advances in Geosciences*, **2**, 217–220.

Emanuel, K. A. and Nolan, D. S. (2004) Tropical cyclone activity and the global climate system. In *26th Conference on Hurricanes and Tropical Meteorology*, 10A.2.

Emanuel, K. A. and Rotunno, R. (1989) Polar lows as arctic hurricanes. *Tellus A: Dynamic Meteorology and Oceanography*, **41**, 1–17.

Ernst, J. A. and Matson, M. (1983) A Mediterranean tropical storm? *Weather*, **38**, 332–337.

Esty, W. W. and Banfield, J. D. (2003) The box-percentile plot. *Journal of Statistical Software*, **8**, 1–14.

Evans, C., Wood, K. M., Aberson, S. D., Archambault, H. M., Milrad, S. M., Bosart, L. F., Corbosiero, K. L., Davis, C. A., Dias Pinto, J. R., Doyle, J., Fogarty, C., Galarneau Jr., T. J., Grams, C. M., Griffin, K. S., Gyakum, J., Hart, R. E., Kitabatake, N., Lentink, H. S., McTaggart-Cowan, R., Perrie, W., Quinting, J. F. D., Reynolds, C. A., Riemer, M., Ritchie, E. A., Sun, Y. and Zhang, F. (2017) The extratropical transition of tropical cyclones. Part I: Cyclone evolution and direct impacts. *Monthly Weather Review*, **145**, 4317–4344.

Evans, J. L. and Guishard, M. P. (2009) Atlantic subtropical storms. Part I: Diagnostic criteria and composite analysis. *Monthly Weather Review*, **137**, 2065–2080.

Fita, L. and Flaounas, E. (2018) Medicanes as subtropical cyclones: the December 2005 case from the perspective of surface pressure tendency diagnostics and atmospheric water budget. *Quarterly Journal of the Royal Meteorological Society*, **144**, 1028–1044.

Fita, L., Romero, R., Luque, A., Emanuel, K. A. and Ramis, C. (2007) Analysis of the environments of seven Mediterranean tropical-like storms using an axisymmetric, nonhydrostatic, cloud resolving model. *Natural Hazards and Earth System Science*, **7**, 41–56.

Flaounas, E., Raveh-Rubin, S., Wernli, H., Drobinski, P. and Bastin, S. (2015) The dynamical structure of intense Mediterranean cyclones. *Climate Dynamics*, **44**, 2411–2427.

Fowle, M. A. and Roebber, P. J. (2003) Short-range (0-48 h) numerical prediction of convective occurrence, mode, and location. *Weather and Forecasting*, **18**, 782–794.

Gaertner, M. A., Jacob, D., Gil, V., Domínguez, M., Padorno, E., Sánchez, E. and Castro, M. (2007) Tropical cyclones over the Mediterranean Sea in climate change simulations. *Geophysical Research Letters*, **34**, L14711.

Galarneau Jr., T. J., McTaggart-Cowan, R., Bosart, L. F. and Davis, C. A. (2015) Development of North Atlantic tropical disturbances near upper-level potential vorticity streamers. *Journal of the Atmospheric Sciences*, **72**, 572–597.

Giorgi, F. and Lionello, P. (2008) Climate change projections for the Mediterranean region. *Global and planetary change*, **63**, 90–104.

Glatt, I. and Wirth, V. (2014) Identifying Rossby wave trains and quantifying their properties. *Quarterly Journal of the Royal Meteorological Society*, **140**, 384–396.

Gneiting, T. and Katzfuss, M. (2014) Probabilistic forecasting. *Annual Review of Statistics and Its Application*, **1**, 125–151.

Gneiting, T. and Raftery, A. E. (2005) Weather forecasting with ensemble methods. *Science*, **310**, 248–249.

Gneiting, T., Raftery, A. E., Westveld III, A. H. and Goldman, T. (2005) Calibrated probabilistic forecasting using ensemble model output statistics and minimum CRPS estimation. *Monthly Weather Review*, **133**, 1098–1118.

González-Alemán, J. J., Evans, J. L. and Kowaleski, A. (2018) Use of ensemble forecasts to investigate synoptic influences on the structural evolution and predictability of Hurricane Alex (2016) in the midlatitudes. *Monthly Weather Review*, **146**, 3143–3162.

Grimit, E. P. and Mass, C. F. (2002) Initial results of a mesoscale short-range ensemble forecasting system over the Pacific Northwest. *Weather and Forecasting*, **17**, 192–205.

— (2007) Measuring the ensemble spread–error relationship with a probabilistic approach: Stochastic ensemble results. *Monthly Weather Review*, **135**, 203–221.

Hamill, T. M., Mullen, S. L., Snyder, C., Toth, Z. and Baumhefner, D. P. (2000) Ensemble forecasting in the short to medium range: Report from a workshop. *Bulletin of the American Meteorological Society*, **81**, 2653–2664.

Hamill, T. M., Whitaker, J. S., Fiorino, M. and Benjamin, S. G. (2011) Global ensemble predictions of 2009's tropical cyclones initialized with an ensemble Kalman filter. *Monthly Weather Review*, **139**, 668–688.

Hart, R. E. (2003) A cyclone phase space derived from thermal wind and thermal asymmetry. *Monthly Weather Review*, **131**, 585–616.

Hewson, T. D. (2009) Diminutive frontal waves –A link between fronts and cyclones. *Journal of the Atmospheric Sciences*, **66**, 116–132.

Hewson, T. D. and Titley, H. A. (2010) Objective identification, typing and tracking of the complete life-cycles of cyclonic features at high spatial resolution. *Meteorological Applications*, **17**, 355–381.

Homar, V., Romero, R., Stensrud, D. J., Ramis, C. and Alonso, S. (2003) Numerical diagnosis of a small, quasi-tropical cyclone over the western Mediterranean: Dynamical vs. boundary factors. *Quarterly Journal of the Royal Meteorological Society*, **129**, 1469–1490.

Hopson, T. M. (2014) Assessing the ensemble spread–error relationship. *Monthly Weather Review*, **142**, 1125–1142.

Hulme, A. L. and Martin, J. E. (2009a) Synoptic- and frontal-scale influences on tropical transition events in the Atlantic basin. Part I: A six-case survey. *Monthly Weather Review*, **137**, 3605–3625.

— (2009b) Synoptic- and frontal-scale influences on tropical transition events in the Atlantic basin. Part II: Tropical transition of Hurricane Karen. *Monthly Weather Review*, **137**, 3626–3650.

Jansá, A., Genovés, A. and Garcia-Moya, J. A. (2000) Western Mediterranean cyclones and heavy rain. Part 1: Numerical experiment concerning the Piedmont flood case. *Meteorological Applications*, **7**, 323–333.

Jones, S. C., Harr, P. A., Abraham, J., Bosart, L. F., Bowyer, P. J., Evans, J. L., Hanley, D. E., Hanstrum, B. N., Hart, R. E., Lalaurette, F., Sinclair, M. R., Smith, R. K. and Thorncroft, C. (2003) The extratropical transition of tropical cyclones: Forecast challenges, current understanding, and future directions. *Weather and Forecasting*, **18**, 1052–1092.

Kalnay, E. (2003) *Atmospheric modeling, data assimilation and predictability*. Cambridge University Press.

Keogh, E. and Ratanamahatana, C. A. (2005) Exact indexing of dynamic time warping. *Knowledge and information systems*, **7**, 358–386.

Lagouvardos, K., Kotroni, V., Nickovic, S., Jovic, D., Kallos, G. and Tremback, C. J. (1999) Observations and model simulations of a winter sub-synoptic vortex over the central Mediterranean. *Meteorological Applications*, **6**, 371–383.

Lalaurette, F. (2003) Early detection of abnormal weather conditions using a probabilistic extreme forecast index. *Quarterly Journal of the Royal Meteorological Society*, **129**, 3037–3057.

Leutbecher, M. and Palmer, T. N. (2008) Ensemble forecasting. *Journal of Computational Physics*, **227**, 3515–3539.

Lillo, S. P. and Parsons, D. B. (2017) Investigating the dynamics of error growth in ECMWF medium-range forecast busts. *Quarterly Journal of the Royal Meteorological Society*, **143**, 1211–1226.

Limbach, S., Schömer, E. and Wernli, H. (2012) Detection, tracking and event localization of jet stream features in 4-D atmospheric data. *Geoscientific Model Development*, **5**, 457–470.

Lionello, P., Cavaleri, L., Nissen, K. M., Pino, C., Raicich, F. and Ulbrich, U. (2012) Severe marine storms in the Northern Adriatic: characteristics and trends. *Physics and Chemistry of the Earth, Parts A/B/C*, **40**, 93–105.

Lorenz, E. N. (1956) Empirical orthogonal functions and statistical weather prediction. Science Report 1, Statistical Forecasting Project, Department of Meteorology, MIT (NTIS AD 110268), 49 pp.

— (1963a) Deterministic nonperiodic flow. *Journal of the Atmospheric Sciences*, **20**, 130–141.

— (1963b) The predictability of hydrodynamic flow. *Transactions of the New York Academy of Sciences*, **25**, 409–432.

— (1965) A study of the predictability of a 28-variable atmospheric model. *Tellus*, **17**, 321–333.

— (1969a) Atmospheric predictability as revealed by naturally occurring analogues. *Journal of the Atmospheric Sciences*, **26**, 636–646.

— (1969b) The predictability of a flow which possesses many scales of motion. *Tellus*, **21**, 289–307.

— (1982) Atmospheric predictability experiments with a large numerical model. *Tellus*, **34**, 505–513.

— (1996) Predictability: A problem partly solved. In *Proc. Seminar on Predictability*, vol. 1, 40–58.

Lynch, P. (2008) The origins of computer weather prediction and climate modeling. *Journal of Computational Physics*, **227**, 3431–3444.

Magnusson, L., Bidlot, J.-R., Lang, S. T. K., Thorpe, A., Wedi, N. and Yamaguchi, M. (2014) Evaluation of medium-range forecasts for Hurricane Sandy. *Monthly Weather Review*, **142**, 1962–1981.

Magnusson, L., Thorpe, A., Buizza, R., Rabier, F. and Nicolau, J. (2015) Predicting this year's European heat wave. *ECMWF Newsletter*, **145**, 4–5.

Maier-Gerber, M., Pantillon, F. P., Di Muzio, E., Riemer, M., Fink, A. H. and Knippertz, P. (2017) Birth of the Biscane. *Weather*, **72**, 236–241.

Maier-Gerber, M., Riemer, M., Fink, A. H., Knippertz, P., Di Muzio, E. and McTaggart-Cowan, R. (2019) Tropical transition of Hurricane Chris (2012) over the North Atlantic Ocean: A multi-scale investigation of predictability. *Monthly Weather Review*, **147**, 951–970.

Majumdar, S. J. and Torn, R. D. (2014) Probabilistic verification of global and mesoscale ensemble forecasts of tropical cyclogenesis. *Weather and Forecasting*, **29**, 1181–1198.

Marzban, C. and Sandgathe, S. (2008) Cluster analysis for object-oriented verification of fields: A variation. *Monthly Weather Review*, **136**, 1013–1025.

Mayengon, R. (1984) Warm core cyclones in the Mediterranean. *Mariners Weather Log*, **28**, 6–9.

Mazza, E., Ulbrich, U. and Klein, R. (2017) The tropical transition of the October 1996 medicane in the western Mediterranean Sea: A warm seclusion event. *Monthly Weather Review*, **145**, 2575–2595.

McIntyre, M. E. and Palmer, T. N. (1985) A note on the general concept of wave breaking for Rossby and gravity waves. *Pure and Applied Geophysics*, **123**, 964–975.

McTaggart-Cowan, R., Davies, E. L., Fairman Jr., J. G., Galarneau Jr., T. J. and Schultz, D. M. (2015) Revisiting the 26.5 °C sea surface temperature threshold for tropical cyclone development. *Bulletin of the American Meteorological Society*, **96**, 1929–1943.

McTaggart-Cowan, R., Deane, G. D., Bosart, L. F., Davis, C. A. and Galarneau Jr., T. J. (2008) Climatology of tropical cyclogenesis in the North Atlantic (1948–2004). *Monthly Weather Review*, **136**, 1284–1304.

McTaggart-Cowan, R., Galarneau Jr., T. J., Bosart, L. F. and Milbrandt, J. A. (2010a) Development and tropical transition of an Alpine lee cyclone. Part I: case analysis and evaluation of numerical guidance. *Monthly Weather Review*, **138**, 2281–2307.

— (2010b) Development and tropical transition of an Alpine lee cyclone. Part II: Orographic influence on the development pathway. *Monthly Weather Review*, **138**, 2308–2326.

McTaggart-Cowan, R., Galarneau Jr., T. J., Bosart, L. F., Moore, R. W. and Martius, O. (2013) A global climatology of baroclinically influenced tropical cyclogenesis. *Monthly Weather Review*, **141**, 1963–1989.

Melhauser, C. and Zhang, F. (2012) Practical and intrinsic predictability of severe and convective weather at the mesoscales. *Journal of the Atmospheric Sciences*, **69**, 3350–3371.

Miglietta, M. M. (2019) Mediterranean tropical-like cyclones (Medicanes). *Atmosphere*, **10**, 206.

Miglietta, M. M., Cerrai, D., Laviola, S., Cattani, E. and Levizzani, V. (2017) Potential vorticity patterns in Mediterranean "hurricanes". *Geophysical Research Letters*, **44**, 2537–2545.

Miglietta, M. M., Laviola, S., Malvaldi, A., Conte, D., Levizzani, V. and Price, C. (2013) Analysis of tropical-like cyclones over the Mediterranean Sea through a combined modeling and satellite approach. *Geophysical Research Letters*, **40**, 2400–2405.

Miglietta, M. M., Mastrangelo, D. and Conte, D. (2015) Influence of physics parameterization schemes on the simulation of a tropical-like cyclone in the Mediterranean Sea. *Atmospheric Research*, **153**, 360–375.

Miglietta, M. M., Moscatello, A., Conte, D., Mannarini, G., Lacorata, G. and Rotunno, R. (2011) Numerical analysis of a Mediterranean 'hurricane' over south-eastern Italy: sensitivity experiments to sea surface temperature. *Atmospheric research*, **101**, 412–426.

Miglietta, M. M. and Rotunno, R. (2019) Development Mechanisms for Mediterranean Tropical-Like Cyclones (Medicanes). *Quarterly Journal of the Royal Meteorological Society*.

Moscatello, A., Miglietta, M. M. and Rotunno, R. (2008a) Numerical analysis of a Mediterranean "hurricane" over southeastern Italy. *Monthly Weather Review*, **136**, 4373–4397.

— (2008b) Observational analysis of a Mediterranean 'hurricane' over south-eastern Italy. *Weather*, **63**, 306–311.

Munsell, E. B., Zhang, F. and Stern, D. P. (2013) Predictability and dynamics of a nonintensifying tropical storm: Erika (2009). *Journal of the Atmospheric Sciences*, **70**, 2505–2524.

Murphy, J. M. (1988) The impact of ensemble forecasts on predictability. *Quarterly Journal of the Royal Meteorological Society*, **114**, 463–493.

Nachamkin, J. E. (2004) Mesoscale verification using meteorological composites. *Monthly Weather Review*, **132**, 941–955.

Nastos, P. T., Papadimou, K. K. and Matsangouras, I. T. (2018) Mediterranean tropical-like cyclones: Impacts and composite daily means and anomalies of synoptic patterns. *Atmospheric Research*, **208**, 156–166.

Neu, U., Akperov, M. G., Bellenbaum, N., Benestad, R., Blender, R., Caballero, R., ... and Wernli, H. (2013) IMILAST: A community effort to intercompare extratropical cyclone detection and tracking algorithms. *Bulletin of the American Meteorological Society*, **94**, 529–547.

Nissen, K. M., Leckebusch, G. C., Pinto, J. G., Renggli, D., Ulbrich, S. and Ulbrich, U. (2010) Cyclones causing wind storms in the Mediterranean: characteristics, trends and links to large-scale patterns. *Natural Hazards and Earth System Sciences*, **10**, 1379–1391.

Pachauri, R. K., Allen, M. R., Barros, V. R., Broome, J., Cramer, W., Christ, R., Church, J. A., Clarke, L., Dahe, Q., Dasgupta, P., Dubash, N. K., Edenhofer, O., Elgizouli, I., Field, C. B., Forster, P., Friedlingstein, P., Fuglestvedt, J., Gomez-Echeverri, L., Hallegatte, S., Hegerl, G., Howden, M., Jiang, K., Jimenez Cisneroz, B., Kattsov, V., Lee, H., Mach, K. J., Marotzke, J., Mastrandrea, M. D., Meyer, L., Minx, J., Mulugetta, Y., O'Brien, K., Oppenheimer, M., Pereira, J. J., Pichs-Madruga, R., Plattner, G. K., Pörtner, H. O., Power, S. B., Preston, B., Ravindranath, N. H., Reisinger, A., Riahi, K., Rusticucci, M., Scholes, R., Seyboth, K., Sokona, Y., Stavins, R., Stocker, T. F., Tschakert, P., van Vuuren, D. and van Ypserle, J. P. (2014) *Climate Change 2014: Synthesis Report. Contribution of Working Groups I, II and III to the Fifth Assessment Report of the Intergovernmental Panel on Climate Change*. IPCC.

Palmer, T. N. (2000) Predicting uncertainty in forecasts of weather and climate. *Reports on progress in Physics*, **63**, 71–116.

— (2002) The economic value of ensemble forecasts as a tool for risk assessment: From days to decades. *Quarterly Journal of the Royal Meteorological Society*, **128**, 747–774.

Palmer, T. N., Döring, A. and Seregin, G. (2014) The real butterfly effect. *Nonlinearity*, **27**, R123.

Palmer, T. N., Gelaro, R., Barkmeijer, J. and Buizza, R. (1998) Singular vectors, metrics, and adaptive observations. *Journal of the Atmospheric Sciences*, **55**, 633–653.

Palmer, T. N. and Räisänen, J. (2002) Quantifying the risk of extreme seasonal precipitation events in a changing climate. *Nature*, **415**, 512–514.

Palmén, E. H. and Newton, C. W. (1969) *Atmospheric circulation systems: their structure and physical interpretation*, vol. 13. Academic Press.

Pantillon, F. P., Chaboureau, J.-P., Mascart, P. J. and Lac, C. (2013) Predictability of a Mediterranean tropical-like storm downstream of the extratropical transition of Hurricane Helene (2006). *Monthly Weather Review*, **141**, 1943–1962.

Pantillon, F. P., Chaboureau, J.-P. and Richard, E. (2016) Vortex–vortex interaction between Hurricane Nadine (2012) and an Atlantic cut-off dropping the predictability over the Mediterranean. *Quarterly Journal of the Royal Meteorological Society*, **142**, 419–432.

Pappenberger, F., Bogner, K., Wetterhall, F., He, Y., Cloke, H. L. and Thielen, J. (2011) Forecast convergence score: a forecaster's approach to analysing hydrometeorological forecast systems. *Advances in Geosciences*, **29**, 27–32.

Peterssen, S. (1956) *Weather Analysis and Forecasting*, vol. 1. McGraw-Hill.

Pfahl, S. and Wernli, H. (2012) Quantifying the relevance of cyclones for precipitation extremes. *Journal of Climate*, **25**, 6770–6780.

Picornell, M. A., Campins, J. and Jansá, A. (2014) Detection and thermal description of medicanes from numerical simulation. *Natural Hazards and Earth System Sciences*, **14**, 1059–1070.

Prates, F. and Buizza, R. (2011) PRET, the Probability of RETurn: a new probabilistic product based on generalized extreme-value theory. *Quarterly Journal of the Royal Meteorological Society*, **137**, 521–537.

Pytharoulis, I. (2018) Analysis of a Mediterranean tropical-like cyclone and its sensitivity to the sea surface temperatures. *Atmospheric Research*, **208**, 167–179.

Pytharoulis, I., Craig, G. and Ballard, S. (2000) The hurricane-like Mediterranean cyclone of January 1995. *Meteorological Applications*, **7**, 261–279.

Pytharoulis, I., Matsangouras, I. T., Tegoulias, I., Kotsopoulos, S., Karacostas, T. S. and Nastos, P. T. (2017) Numerical Study of the Medicane of November 2014. In *Perspectives on Atmospheric Sciences*, 115–121.

Rabier, F., Järvinen, H., Klinker, E., Mahfouf, J. F. and Simmons, A. (2000) The ECMWF operational implementation of four-dimensional variational assimilation. I: Experimental results with simplified physics. *Quarterly Journal of the Royal Meteorological Society*, **126**, 1143–1170.

Rasmussen, E. A. (1979) The polar low as an extratropical CISK disturbance. *Quarterly Journal of the Royal Meteorological Society*, **105**, 531–549.

Rasmussen, E. A., Pedersen, T. S., Pedersen, L. T. and Turner, J. (1992) Polar lows and arctic instability lows in the Bear Island region. *Tellus A*, **44**, 133–154.

Rasmussen, E. A. and Zick, C. (1987) A subsynoptic vortex over the Mediterranean with some resemblance to polar lows. *Tellus A*, **39**, 408–425.

Raveh-Rubin, S. and Wernli, H. (2015) Large-scale wind and precipitation extremes in the Mediterranean: a climatological analysis for 1979–2012. *Quarterly Journal of the Royal Meteorological Society*, **141**, 2404–2417.

Reale, O. and Atlas, R. (2001) Tropical cyclone-like vortices in the extratropics: Observational evidence and synoptic analysis. *Weather and forecasting*, **16**, 7–34.

Ricchi, A., Miglietta, M. M., Bonaldo, D., Cioni, G., Rizza, U. and Carniel, S. (2019) Multi-physics ensemble versus atmosphere-ocean coupled model simulations for a tropical-like cyclone in the Mediterranean Sea. *Atmosphere*, **10**, 202.

Riemer, M. and Jones, S. C. (2014) Interaction of a tropical cyclone with a high-amplitude, midlatitude wave pattern: Waviness analysis, trough deformation and track bifurcation. *Quarterly Journal of the Royal Meteorological Society*, **140**, 1362–1376.

Rife, D. L. and Davis, C. A. (2005) Verification of temporal variations in mesoscale numerical wind forecasts. *Monthly Weather Review*, **133**, 3368–3381.

Rios-Berrios, R., Torn, R. D. and Davis, C. A. (2016) An ensemble approach to investigate tropical cyclone intensification in sheared environments. Part I: Katia (2011). *Journal of the Atmospheric Sciences*, **73**, 71–93.

Rivière, G. (2009) Effect of latitudinal variations in low-level baroclinicity on eddy life cycles and upper-tropospheric wave-breaking processes. *Journal of the Atmospheric Sciences*, **66**, 1569–1592.

da Rocha, R. P., Reboita, M. S., Gozzo, L. F., Dutra, L. M. M. and de Jesus, E. M. (2018) Subtropical cyclones over the oceanic basins: a review. *Annals of the New York Academy of Sciences*, **1436**, 138–156.

Romero, R. and Emanuel, K. A. (2013) Medicane risk in a changing climate. *Journal of Geophysical Research: Atmospheres*, **118**, 5992–6001.

— (2017) Climate change and Hurricane-like extratropical cyclones: Projections for North Atlantic polar lows and medicanes based on CMIP5 models. *Journal of Climate*, **30**, 279–299.

Rotunno, R. and Emanuel, K. A. (1987) An air–sea interaction theory for tropical cyclones. Part II: Evolutionary study using a nonhydrostatic axisymmetric numerical model. *Journal of the Atmospheric Sciences*, **44**, 542–561.

Rotunno, R. and Snyder, C. (2008) A generalization of Lorenz's model for the predictability of flows with many scales of motion. *Journal of the Atmospheric Sciences*, **65**, 1063–1076.

Sakoe, H. and Chiba, S. (1978) Dynamic programming algorithm optimization for spoken word recognition. *IEEE Transactions on Acoustics, Speech, and Signal Processing*, **26**, 43–49.

Selz, T. (2019) Estimating the intrinsic limit of predictability using a stochastic convection scheme. *Journal of the Atmospheric Sciences*, **76**, 757–765.

Simmons, A. J. and Hollingsworth, A. (2002) Some aspects of the improvement in skill of numerical weather prediction. *Quarterly Journal of the Royal Meteorological Society*, **128**, 647–677.

Skok, G., Bacmeister, J. and Tribbia, J. (2013) Analysis of tropical cyclone precipitation using an object-based algorithm. *Journal of Climate*, **26**, 2563–2579.

Souders, M. B., Colle, B. A. and Chang, E. K. (2014a) A description and evaluation of an automated approach for feature-based tracking of Rossby wave packets. *Monthly Weather Review*, **142**, 3505–3527.

— (2014b) The climatology and characteristics of Rossby wave packets using a feature-based tracking technique. *Monthly Weather Review*, **142**, 3528–3548.

Sousounis, P. J., Wallman, J., Mann, G. E. and Miner, T. J. (2001) "Hurricane Huron": An Example of an Extreme Lake-Aggregate Effect in Autumn. *Monthly weather review*, **129**, 401–419.

Strong, C. and Magnusdottir, G. (2008) Tropospheric Rossby wave breaking and the NAO/NAM. *Journal of the Atmospheric Sciences*, **65**, 2861–2876.

Sun, Y. Q. and Zhang, F. (2016) Intrinsic versus practical limits of atmospheric predictability and the significance of the butterfly effect. *Journal of the Atmospheric Sciences*, **73**, 1419–1438.

Tao, D. and Zhang, F. (2015) Effects of vertical wind shear on the predictability of tropical cyclones: Practical versus intrinsic limit. *Journal of Advances in Modeling Earth Systems*, **7**, 1534–1553.

Thorncroft, C. D., Hoskins, B. J. and McIntyre, M. E. (1993) Two paradigms of baroclinic-wave life-cycle behaviour. *Quarterly Journal of the Royal Meteorological Society*, **119**, 17–55.

Tibaldi, S. and Molteni, F. (1990) On the operational predictability of blocking. *Tellus A*, **42**, 343–365.

Torn, R. D. and Cook, D. (2013) The role of vortex and environment errors in genesis forecasts of Hurricanes Danielle and Karl (2010). *Monthly Weather Review*, **141**, 232–251.

Torn, R. D., Whitaker, J. S., Pegion, P., Hamill, T. M. and Hakim, G. J. (2015) Diagnosis of the source of GFS medium-range track errors in Hurricane Sandy (2012). *Monthly Weather Review*, **143**, 132–152.

Toth, Z. and Kalnay, E. (1993) Ensemble forecasting at NMC: The generation of perturbations. *Bulletin of the American Meteorological Society*, **74**, 2317–2330.

— (1997) Ensemble forecasting at NCEP and the breeding method. *Monthly Weather Review*, **125**, 3297–3319.

Tous, M. and Romero, R. (2013) Meteorological environments associated with medicane development. *International Journal of Climatology*, **33**, 1–14.

Tous, M., Romero, R. and Ramis, C. (2013) Surface heat fluxes influence on medicane trajectories and intensification. *Atmospheric research*, **123**, 400–411.

Tous, M., Zappa, G., Romero, R., Shaffrey, L. and Vidale, P. L. (2016) Projected changes in medicanes in the HadGEM3 N512 high-resolution global climate model. *Climate Dynamics*, **47**, 1913–1924.

Ulbrich, U., Leckebusch, G. C. and Pinto, J. G. (2009) Extra-tropical cyclones in the present and future climate: a review. *Theoretical and Applied Climatology*, **96**, 117–131.

Van Schaeybroeck, B. and Vannitsem, S. (2016) A probabilistic approach to forecast the uncertainty with ensemble spread. *Monthly Weather Review*, **144**, 451–468.

Walsh, K., Giorgi, F. and Coppola, E. (2014) Mediterranean warm-core cyclones in a warmer world. *Climate dynamics*, **42**, 1053–1066.

Wang, Z., Li, W., Peng, M. S., Jiang, X., McTaggart-Cowan, R. and Davis, C. A. (2018) Predictive skill and predictability of North Atlantic tropical cyclogenesis in different synoptic flow regimes. *Journal of the Atmospheric Sciences*, **75**, 361–378.

Warner, T. T. (2010) *Numerical weather and climate prediction*. Cambridge University Press.

Wernli, H., Paulat, M., Hagen, M. and Frei, C. (2008) SAL–A novel quality measure for the verification of quantitative precipitation forecasts. *Monthly Weather Review*, **136**, 4470–4487.

Whitaker, J. S., Hamill, T. M., Wei, X., Song, Y. and Toth, Z. (2008) Ensemble data assimilation with the NCEP global forecast system. *Monthly Weather Review*, **136**, 463–482.

Whitaker, J. S. and Loughe, A. F. (1998) The relationship between ensemble spread and ensemble mean skill. *Monthly Weather Review*, **126**, 3292–3302.

Wiegand, L. and Knippertz, P. (2014) Equatorward breaking Rossby waves over the North Atlantic and Mediterranean region in the ECMWF operational Ensemble Prediction System. *Quarterly Journal of the Royal Meteorological Society*, **140**, 58–71.

Wilks, D. S. (2011) *Statistical Methods in the Atmospheric Sciences*. Academic Press.

— (2016) "The stippling shows statistically significant grid points": How research results are routinely overstated and overinterpreted, and what to do about it. *Bulletin of the American Meteorological Society*, **97**, 2263–2273.

Wirth, V., Riemer, M., Chang, E. K. and Martius, O. (2018) Rossby wave packets on the midlatitude waveguide—A review. *Monthly Weather Review*, **146**, 1965–2001.

Wolf, G., Brayshaw, D. J., Klingaman, N. P. and Czaja, A. (2018) Quasi-stationary waves and their impact on European weather and extreme events. *Quarterly Journal of the Royal Meteorological Society*, **144**, 2431–2448.

Wolf, G. and Wirth, V. (2015) Implications of the semigeostrophic nature of Rossby waves for Rossby wave packet detection. *Monthly Weather Review*, **143**, 26–38.

— (2017) Diagnosing the horizontal propagation of Rossby wave packets along the midlatitude waveguide. *Monthly Weather Review*, **145**, 3247–3264.

Yamaguchi, M. and Majumdar, S. J. (2010) Using TIGGE data to diagnose initial perturbations and their growth for tropical cyclone ensemble forecasts. *Monthly Weather Review*, **138**, 3634–3655.

Ying, Y. and Zhang, F. (2017) Practical and intrinsic predictability of multiscale weather and convectively coupled equatorial waves during the active phase of an MJO. *Journal of the Atmospheric Sciences*, **74**, 3771–3785.

Zhang, F., Bei, N., Rotunno, R., Snyder, C. and Epifanio, C. C. (2007) Mesoscale predictability of moist baroclinic waves: Convection-permitting experiments and multistage error growth dynamics. *Journal of the Atmospheric Sciences*, **64**, 3579–3594.

Zhang, F., Qiang Sun, Y., Magnusson, L., Buizza, R., Lin, S. J., Chen, J. H. and Emanuel, K. A. (2019) What is the Predictability Limit of Midlatitude Weather? *Journal of the Atmospheric Sciences*, **76**, 1077–1091.

Zhang, F. and Sippel, J. A. (2009) Effects of moist convection on hurricane predictability. *Journal of the Atmospheric Sciences*, **66**, 1944–1961.

Zhang, F. and Tao, D. (2013) Effects of vertical wind shear on the predictability of tropical cyclones. *Journal of the Atmospheric Sciences*, **70**, 975–983.

Zhang, G., Wang, Z., Dunkerton, T. J., Peng, M. S. and Magnusdottir, G. (2016) Extratropical impacts on Atlantic tropical cyclone activity. *Journal of the Atmospheric Sciences*, **73**, 1401–1418.

Zhu, Y. (2005) Ensemble forecast: A new approach to uncertainty and predictability. *Advances in Atmospheric Sciences*, **22**, 781–788.

Zimin, A. V., Szunyogh, I., Hunt, B. R. and Ott, E. (2006) Extracting envelopes of nonzonally propagating Rossby wave packets. *Monthly Weather Review*, **134**, 1329–1333.

Zsótér, E. (2006) Recent developments in extreme weather forecasting. ECMWF Newsletter, **107**, 8–17.

Zsótér, E., Buizza, R. and Richardson, D. (2009) "Jumpiness" of the ECMWF and Met Office EPS control and ensemble-mean forecasts. *Monthly Weather Review*, **137**, 3823–3836.

Acknowledgements

First of all, I would like to sincerely express my gratitude to my advisors for their continuous support and constructive feedback: Prof. Andreas H. Fink, whose enthusiasm and keen passion intoxicated me from day one (and who knows he is always welcome in Abruzzo to go visit the Calderone glacier before it disappears); and Dr. Michael Riemer, whose careful, in-depth comments and precious advice spanning a vast array of work aspects helped me grow personally as well as professionally. My sincere thanks also go to Prof. Peter Knippertz, who as our group leader made me immediately feel welcome at the institute and whose insightful considerations on all things meteorological helped me develop my scientific intuition; I also thank him for organizing the best summer parties, which have become a tradition and help create valuable bonds within the working group.

I am of course grateful to all of my colleagues. I had a very enjoyable time working with them and always felt intellectually stimulated; discussing my work with them helped me immensely in refining my working method and improving the quality of my results. I owe it to Anke, Titike and Joseph, with whom I shared my office in Karlsruhe, if my working hours always flew by; they are some of the most kind-hearted people I know and the four of us made the most wonderfully heterogeneous office (I need to thank Joseph personally for helping me keep my English vocabulary afloat in Germany!). Without Michael I would not have had some of the most in-depth, painstaking discussions the IMK has ever seen; only perfectionists like us can appreciate that! I thank Florian not only for his insightful comments on my work, but also for being the perfect bike riding partner and for making me want to play keyboard again; the institute actually had plenty of bike-loving people and I had a great time on the wheels also with Katharina, Hilke and Heinz Jürgen. I am grateful to Andreas for having me over and showing me how to make honey, but also for being able to spark interesting conversations about plants, languages, philosophy and much more. I thank Marlon for being a fun colleague, a caring person and my first hiking fella in Germany,

together with Florian; with Eva we also share unforgettable memories of RF's comeback in 2017! Gregor is possibly the most helpful colleague ever, but he is also responsible for my first visit ever to a *soccer* stadium. I am grateful to Andrew for bringing a bit of British atmosphere to the institute. I also had a great time and valuable discussions with Pila, Peter, Philipp, Manuel, Lisa (whom I should thank for making us all suffer, I guess), Corinna Hoose and her working group and many more colleagues between CS and CN. Finally, I should thank our secretaries Frau Schönbein and Frau Stenschke for helping me a great deal with convoluted forms and 40-letter German words; I owe it to them if I survived my first impact with German bureaucracy and I learned some of my first German words with them. Plus, the long discussions I had with Doris on cycling, the Giro d'Italia and the Tour de France make some of my nicest memories at the KIT.

But the long list of colleagues does not end here. Having spent half of my PhD at the University of Mainz, I got to experience two totally different worlds with their rules and traditions. I am grateful to Christian, Marlene, Georgios and Paolo, whom I knew already from Waves to Weather meetings, for welcoming me to Mainz and helping me adapt to the new environment. Unfortunately I did not have the pleasure of sharing an office with them – or perhaps fortunately, as I ended up in the coolest (temperature-wise) office of the entire floor. My first months were quite solitary, but then Franzi came back and she has been a very nice office mate. With her, Mark, Vera, Joachim and other colleagues I had a good time playing beach volleyball during lunch breaks in the hottest summer Germany has seen recently. I also thank Prof. Volkmar Wirth, Dr. Joachim Eichhorn and Prof. Holger Tost for welcoming me to the institute in Mainz and helping me with bureaucratic and IT matters. Finally, I am in debt with my German teacher Anne: thanks to her I got to appreciate the subtleties of the German language and I would have never been able to survive a job interview in German if I had not attended two of her classes.

I am of course very grateful to all of the colleagues within Waves to Weather. I enjoyed working with them and participating to the numerous meetings in various cities in Germany. After experiencing the smooth and painstaking organization of these meetings, I feel my professionalism has greatly improved. I want to thank here all of the Waves to Weather Early Career Scientists, with whom I had lots of stimulating discussions and whose company I enjoyed during our ECS meetings; in particular the one on the Zugspitze was a blast! A special thank goes to Audine: not only does she always organize everything perfectly, but she also gives it a light-hearted and playful touch.

I am glad I had plenty of opportunities to go to conferences and workshops around Europe, where I could meet and exchange ideas with a great number of colleagues. While it is impossible to mention everyone here, I would like to thank especially Marcello Miglietta, Manos Flaounas, Silvio Davolio, Diego Carrió and Annalina Lombardi for their valuable feedback and support.

While all the people I mentioned above have helped me throughout my PhD years, I would not be where I am if it had not been for my family: my parents, who were always there for me, constantly supported me and gifted me with a special attitude towards life which helps me weather the most intense storms (including Medicanes); my sister, who is an immense source of inspiration for me and the strongest person I know, and who believes in me more than I will ever do; my grandfather, who initiated my passion for meteorology by bequeathing his to me and who will be thrilled when I tell him that *saccature* (troughs) play a central role in my thesis, as he has been talking about them for ages; and all of my aunts, uncles and cousins who have always believed in me.

I am also grateful to all of my friends who supported me during these years: the ones I have met in Germany, many of whom are also climbing their way towards their PhD (or they got it already), and the old ones, who have known me the longest and keep supporting me despite being far away. With Alessio, Elisabetta, Angeliki, Ruba and Eleonora – the Mediterranean Resistance of – I have shared many great moments in Mainz. Marco and Nina are what makes me miss Karlsruhe the most. Federico and Carlo always believed I was going to become a great metoreoleolologist. And the Bologna FAM gang: Michela, Riccardo, Leonardo, Francesca and Olimpia (who started at IMK the exact day I left!) are dispersed in five different countries but still remind me with their passion why we all started studying meteorology in the first place.

Last but not least, I want to express my immense, profound gratitude to my girlfriend Angela, with whom I have shared possibly every detail of this PhD. She knows more than anyone else what I have gone through in the last years and she has been marvellously caring, supportive and patient, especially during those gloomy winter months when everything seems hopeless. This PhD is also hers.